Sensitized Energy Transfer for Organic Solar Cells, Optical Solar Concentrators, and Solar Pumped Lasers

by

Philip David Reusswig

B.S. Electrical Engineering
Iowa State University (2006)
M.S. Electrical Engineering
Iowa State University (2008)

Submitted to the

Department of Electrical Engineering and Computer Science

in partial fulfillment of the requirements for the degree of

Doctor of Philosophy

at the

Massachusetts Institute of Technology

September 2014

Author..... Signature redacted .....
Department of Electrical Engineering and Computer Science
August 25, 2014

Certified by..... Signature redacted .....
Professor Marc A. Baldo
Thesis Supervisor

Certified by..... Signature redacted .....
Professor Leslie A. Kolodziejski
Chair, Department Committee on Graduate Students

Sensitized Energy Transfer for Organic Solar Cells, Optical Solar Concentrators, and Solar Pumped Lasers

by

Philip David Reusswig

Submitted to the Department of Electrical Engineering and Computer Science
on August 28, 2014, in partial fulfillment of the
requirements for the degree of
Doctor of Philosophy

Abstract

The separation of chromophore absorption and excitonic processes, such as singlet exciton fission and photoluminescence, offers several advantages to the design of organic solar cells and luminescent solar concentrators (LSCs) for the end goal of achieving a lower cost solar energy generation. This thesis explores three new device architectures to overcome limited solar absorption in singlet-exciton-fission based solar cells and neodymium based LSCs.

The process of singlet exciton fission is de-coupled from photon absorption, exciton diffusion, and charge transport in singlet-exciton-fission based solar cells by inserting a singlet fission material at the donor-acceptor interface of an organic solar cell. Singlet excitons generated in the singlet exciton donor are transferred to the singlet fission material through near field energy transfer. In this device structure, the singlet donor can be chosen for high photon absorption, exciton diffusion, and charge transport, and the singlet fission sensitizer can be selected for high singlet fission efficiency. We demonstrated a doubling of the external quantum efficiency from 12.8% to 27.6% in a singlet donor (TPTPA) through the introduction of thin film singlet fission sensitizer (rubrene) for high efficiency organic solar cells.

To reduce the cost of electricity generated by sunlight via LSC systems, replacing the expensive high efficiency visible photovoltaic (PV) elements with cheap, high efficiency, earth abundant near-infrared PV elements made with silicon. This requires replacing within the LSC the visible emitting chromophores with near infrared emitters. Here, we present the use of a lanthanide ion, neodymium--colloidal nanocrystal energy cascade system as a promising LSC emitter scheme for the silicon spectral region. Peak optical quantum efficiencies of 43% in a Nd^{3+}:glass based LSC are demonstrated with simulated high geometric gain performance. With cascade energy transfer, the optical quantum efficiency in the visible of a Nd^{3+}:glass is significantly improved with peak efficiency of 28%. The enhanced solar absorption of Nd^{3+}:glass through cascade energy transfer can be extended into the infrared with more optimal sensitizers.

The idea of directly converting broad-band solar radiation into coherent and narrow-band laser radiation could enable many attractive technologies for solar energy. Here, we present an architecture for solar pumped lasers that uses a luminescent solar concentrator to decouple the conventional trade-off between solar absorption efficiency and the mode volume of the optical gain material. We report a 750-μm-thick Nd^{3+}-doped YAG planar waveguide sensitized by a

luminescent CdSe/CdZnS (core/shell) colloidal nanocrystal, yielding a peak cascade energy transfer of 14%, a broad spectral response in the visible portion of the solar spectrum, and an equivalent quasi-CW solar lasing threshold of 20 W-cm^{-2}, or approximately 200 suns. The efficient coupling of incoherent, spectrally broad sunlight in small gain volumes should allow the generation of coherent laser light from intensities of less than 100 suns.

Acknowledgements

The time I have been spent pursuing my PhD degree will be looked back on with fondness thanks to so many bright and generous individuals. Foremost of all, I would like to thank my research supervisor Professor Marc Baldo for his guidance over the years. Through good and bad results, Marc was ever the optimist and never wavered in his encouragement. His door was always open for me to act as a sounding board for project ideas or just to chat. Discussing, listening, and observing Marc over the years, I've developed a critical and strong applied science and engineering approach to problem solving, and hope to have as deep a joy of engineering and science that Marc displays every day at MIT.

I would also like to acknowledge Professor Leslie Kolodziejski, who not only served on my PhD committee, but also as a member of my RQE committee. She has always been very inquisitive in our conversations and always supportive and pleasant. Professor Vladimir Bulovic served on my thesis committee and was an ever present personality during my PhD degree in building 13. Observing him teach, speak, and think over the years offered another role model to me in my academic inquiries and his steady sunny disposition always left me smiling also.

It has been a pleasure to be a part of the Soft Semiconductor Group for all the collaboration, exciting projects, and friendship. When I arrived at MIT, I could not have asked for two better office mates in Carlijn Mulder and Carmel Rotschild. I thank Carlijn for her many discussions with me concerning luminescent solar concentrators. Your ability to execute on hard problems and work ethic served as a model for me. And for introducing me to the wonderful activity that is rock climbing and to many post-climbing beers and burgers at Charlie's Kitchen. I thank Carmel Rotschild for him bringing me on to collaborate on the solar laser project. I

thoroughly enjoyed our many scientific discussions over coffee and greatly admire your enthusiasm for research and science. I have been lucky to have yet another pair of stimulating office mates in Nicolas Thompson and Priya Jadhav. I thank Nicolas Thompson for him struggling with me to make Ti^{3+} emit light. Priya Jadhav, thank you for putting up with my unwavering sarcasm and learning to respond in kind. Jiye Lee, your persistence, tenacity, and curiosity served as a model for me as a growing researcher. I thank Paul Azunre for many stimulating conversations and also for kicking a soccer ball around and watching a World Cup game or two. I thank Dan Congreve for his help and contributions to the singlet fission sensitizer work, and to continuing the tradition of MRC ISU students at MIT. I thank Jennifer Scherer for holding my hand with colloidal nanocrystals and for our shared affection of Calvin and Hobbes. I thank the many post docs of building 13 that I shared a coffee with especially Simon Gustavsson, Jonas Bylander, Ofer Shapira, Sebastian Reineke, and Shlomy Goffri. I thank Matthias Bahlke and Jason Sussman for great discussions over delicious Chipotle.

I would especially like to acknowledge my family for their continual love and support. Without my parents, this degree would not have occurred. Their encouragement and support is a true gift. I thank my siblings, Matt and Emily, for their wonderful sarcastic senses of humor, work ethic, and their moral support over the years. I thank my Grandma Sabbath for all the looks of love that have helped me towards my goals. I thank my Grandma Reusswig for her amazing sense of humor and always giving me a hard time in the most supportive way. Finally, I would like to thank both my Grandpa Sabbath and Reusswig who sadly were not able to see the completion of this degree. They both had incredible integrity, work ethics, and senses of humor that I have greatly admired. Thank you all for helping shape the clay.

Contents

List of Figures

Chapter 1

Introduction

1.1 Motivation

Growing up in America, I have taken for granted the fact of access to energy on demand. Turning on a light or powering up a computer for work is not greeted with more than a blink of an eye. Large fractions of the global population (> 7 billion) do not take energy for granted as we do in America. Over 20% of the world's population is without access to electricity, almost all of whom live in developing countries [1]. This fact is exemplified in Fig. 1.1, a photo of some students in Conakry, Guinea. They are studying under street lamps due to the lack of reliable energy at home. Additionally, about 2.8 billion use solid fuels – wood, charcoal, coal, and dung – for cooking and heating [1]. The generated fumes and smoke from open cooking fires kills approximately 1.5 million people mostly women and children, from respiratory diseases.

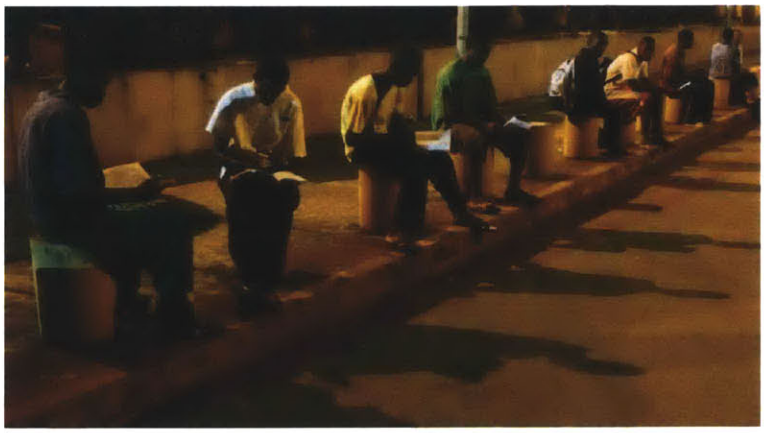

Fig. 1.1 Photograph of students in Conakry, Guinea, studying under street lamps, because they do not have reliable lights at home [2].

The global population is projected to increase to over 9 billion people by 2050, largely coming from developing countries [1]. For these developing countries to lift themselves out of poverty will require lights for schools so students can study when it is dark out. Refrigerators in hospitals and health clinics to keep medicine and vaccines cold. Pumps to irrigate farmland and provide clean water. The motivation to provide more people access to reliable and affordable energy is economical in nature, but also morally driven. Solar energy is one route to this goal.

1.2 Solar Energy

Solar energy incident on the surface of the Earth annually can easily satisfy human's energy needs and many times more as seen in Fig. 1.2. Unlike traditional energy sources – coal, natural gas, uranium, and petroleum – solar energy is renewable, abundant, with short energy payback times. Coupled with the growing concern of human's impact on the global environment due to carbon emissions from sources such as the energy sector, moving to low carbon energy sources such as solar energy may mitigate human's impact on the environment.

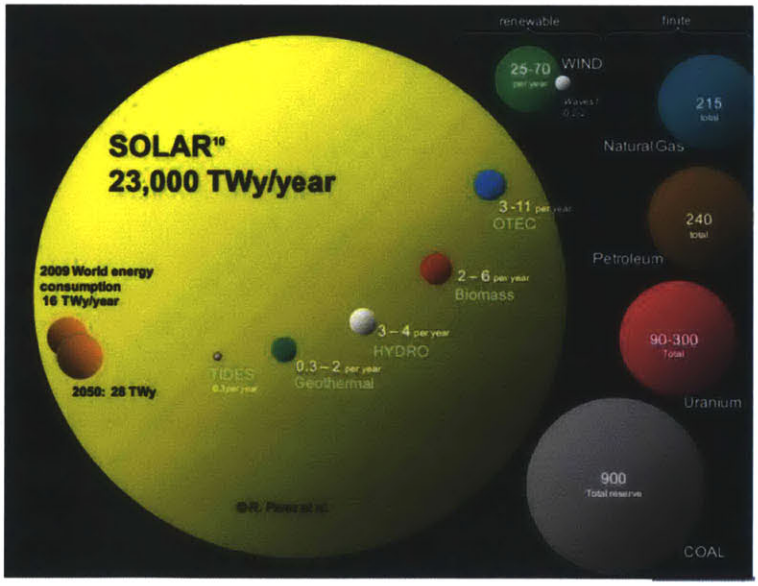

Fig. 1.2 Finite and renewable planetary energy reserves. Total recoverable reserves are shown for the finite resources. Yearly potential is shown for the renewables Figure from [3].

Despite the advantages of solar energy, less than 0.1% of global energy production is derived from photovoltaics (PV) and concentrated solar power (CSP). One reason for the low market share of solar energy is due to the lack of economic incentives relative to traditional energy resources. The cost of solar energy produced from PV and CSP systems must reach grid parity before a significant market acceptance will occur. Fig. 1.3 [4] illustrates this problem for various electricity markets, most of which have no economic incentive to transition to clean solar energy. The left y-axis is the average power per household. The right y-axis is the cost per watt of solar energy. The x-axis is annual solar energy yield. The sizes of the circles are the size of the electricity market. The dark blue contour are markets where there is an economic incentive to displace the more traditional energy sources. As the cost of solar energy decreases, many markets will move to PV and CSP solar generation, as shown in light blue. To reach grid parity in emerging economies of China and India significant innovations in PV and CSP solar generation must yet occur.

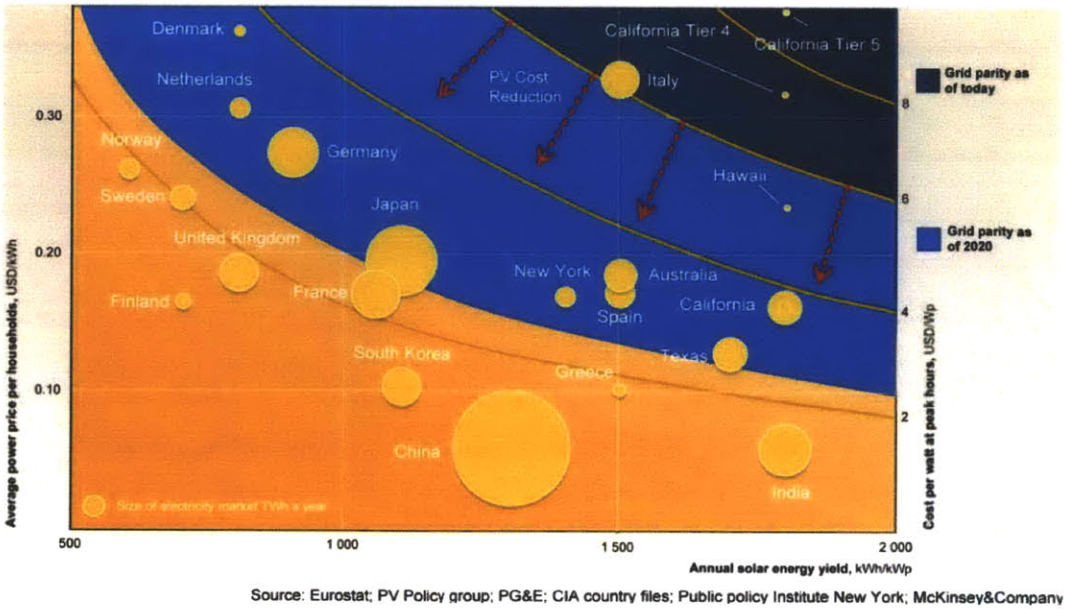

Fig. 1.3 To reach significant solar energy market penetration in emerging economies like China and India, the cost of solar energy generation must be reduced significantly. Figure from [4].

1.2.1 Solar Concentrators

One of the main costs of solar energy is the photovoltaic cost. A well-known method to reduce the cost of the PV is to use a solar concentrator. The general concept is to collect sunlight with an inexpensive concentrator and focus the solar energy onto a small PV, ultimately reducing the amount of expensive photovoltaic used. The geometric concentration factor, G, is defined as the ratio of the area of the collector to the area of the PV:

$$G = \frac{A_{Collector}}{A_{PV}}$$

The geometric gain must be corrected for optical losses in the light collection process; hence the important figure of merit of the concentrator system is the flux gain, F:

$$F = G\eta_{EQE}$$

where η_{EQE} is the external efficiency of the concentrator. The following simple cost model [5] for solar energy produced by a concentrator system can give insight into the ideal concentrator system:

$$\frac{\$}{W_P} = \frac{collector\ cost}{efficiency \times solar\ flux} + \frac{1}{F}\frac{PV\ cost}{efficiency \times solar\ flux} + Maintenance$$

As can be seen, the cost per Watt-peak is composed of three main components: (1) the collector cost and efficiency, (2) the PV cost and efficiency, and (3) any system maintenance costs such as collector or PV cleaning, tracking or pump motor repairs, and collector-PV alignment. To minimize Eq. 1.3, the ideal solar collector system makes use of a cheap solar collector, a collector that operates at high flux gains, and low maintenance costs. The ideal PV has high efficiency and is low cost to further reduce the overall system cost.

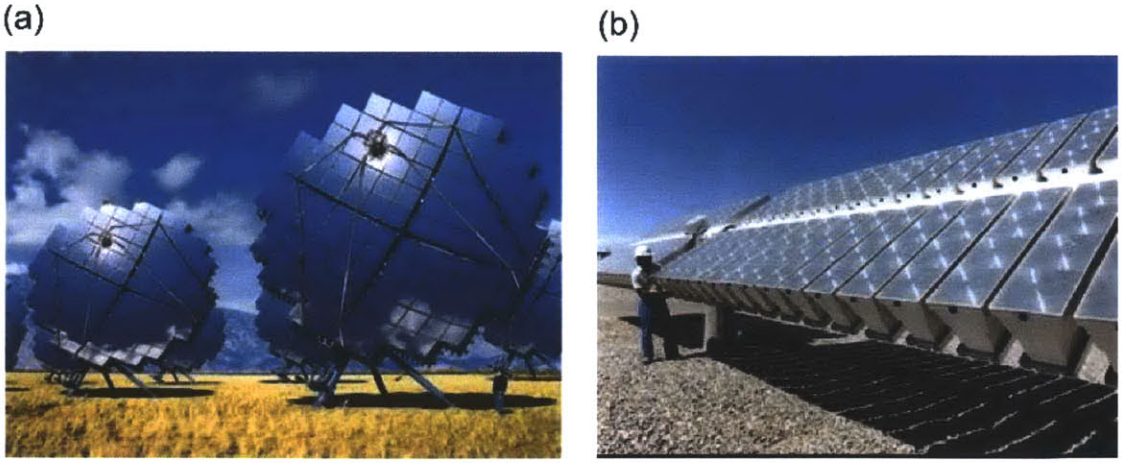

Fig. 1.4 Two examples of traditional solar concentrator systems: (a) Parabolic mirror-based concentrator and (b) Fresnel lens-based concentrator. These systems can achieve high solar concentrations, but require solar tracking, active cooling, and are only compatible with direct sunlight. Pictures from [6, 7].

Traditional solar concentrators are based on imaging systems making use of glass, plastic, or metallic lenses. Fig. 1.4 presents two well-known examples of this class of solar collectors: (a) parabolic mirror-based collector and (b) Fresnel lens-based collector. The maximum achievable solar concentration [8] depends on the light's incident angle, θ_i, and the concentrator refractive index, n, as shown in Eq. 1.4:

$$G_{Max}(n) \leq \frac{n^2}{\sin^2 \theta_i}$$

As seen in the previous equation, for high solar concentrations the incident light angle must be kept small (< 1°). To achieve this, traditional solar concentrators track the sun as it traverses the sky. As has been experimentally [9] demonstrated, these tracking geometric concentrators can operate at solar concentrations of greater than 1,000 suns, significantly reducing the PV system costs.

Even with the advantage of high solar concentration, geometrical concentrators have been limited by a number of factors. The main factor is related to the cost of maintenance. Due to the requirement of solar tracking, these concentrators need moving parts and motors which will need upkeep and replacement. A second limitation is due to the operation of the photovoltaic. Light produces both electrical and thermal energy within the PV. At the high optical concentration, active cooling is required to remove heat to maintain the efficiency and lifetime of the PV. This active cooling requires motors to operate pumps, which will also need maintenance. Finally, these concentrators require clear skies to maintain the low incident angle. Many areas in the world regularly have cloudy days, limiting these concentrators to geographic areas where a majority of sunlight is direct versus diffusive.

1.2.2 High Efficiency Solar Cells

Increasing the efficiency of solar cells can also reduce the cost of solar energy generation by reducing area-related costs of the system. The cost of PV energy is composed of the module, inverter, and the balance of systems (BOS). The BOS consists of all the components of a PV system other than the module and inverter such as land, installation, wiring, and support racks. The fraction of the module, inverter, and BOS for various solar energy generation applications can be seen in Fig. 1.5 [10] for standard 14.5% efficient silicon modules. For utility scale generation, the BOS makes up 68% of the total cost. Higher efficiency modules address the BOS costs by reducing the amount of land required, the number of modules installed, number of junction boxes, wiring, and related maintenance such as cleaning modules and mowing grass.

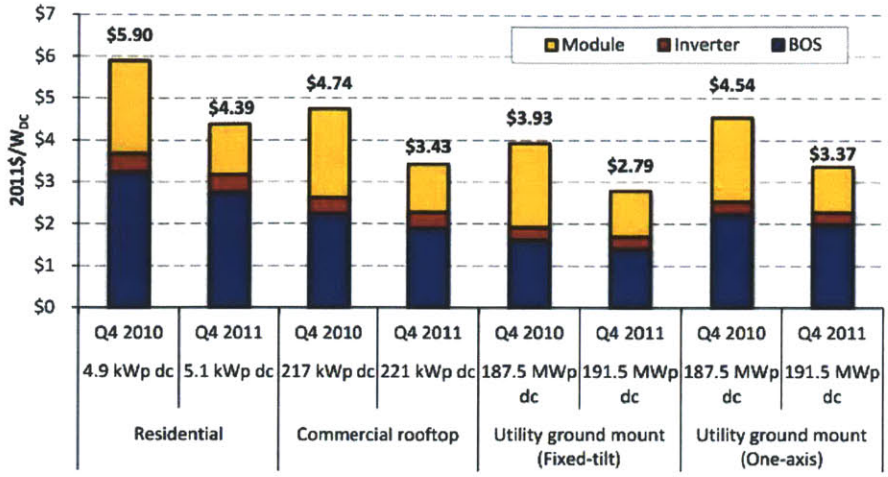

Fig. 1.5 Bottom-up modeled installed PV system prices by sector, Q4 2010 and Q4 2011. Image from [10].

The ultimate efficiency of single junction solar cells is limited by the spectral properties of sunlight and the operation of solar cells. This limit is defined as the Shockley-Queisser limit [11]. The two fundamental losses in single junction solar cells are thermilization and sub-bandgap losses, pictured in Fig. 1.6.a. Sunlight is energetically spectrally broad whereas solar cells operated energetically monochromatically defined by the semiconductor bandgap. A photon with energy in excess of the bandgap produce both an electron with energy of the bandgap and the remainder becomes thermal energy lost to the environment. A photon with energy less than the bandgap cannot be absorbed by the solar cell, eventually being lost to the environment as lost heat. The fraction of solar energy harvested by a silicon solar cell as a function of wavelength can be seen in Fig. 1.6.b. To produce high efficiency solar cells, concepts to address the high energy spectrum and low energy spectrum must be researched.

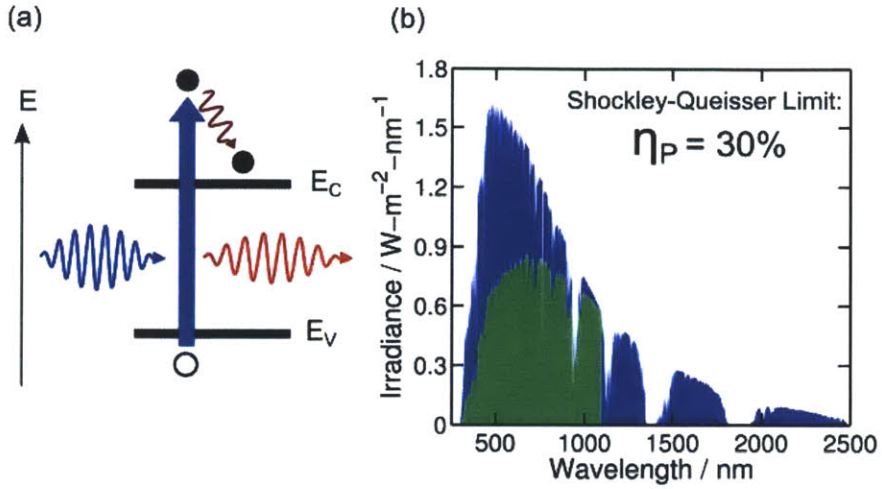

Fig. 1.6 (a) Band diagram of a single junction solar cell. Photons with energy in excess of the bandgap (blue) produce both electrical energy and thermal energy. Photons with energy less than the bandgap (red) are not absorbed. (b) Solar irradiance as a function of wavelength (blue). The fraction of solar energy harvested by a silicon solar cell (green). Only photons near the bandgap produce electrical energy efficiently.

Chapter 2

Enhanced External Quantum Efficiency in Organic Solar Cells via a Singlet Exciton Fission Sensitizer

Expanding the library of organic singlet fission materials

2.1 Introduction

Singlet exciton fission is a well-established phenomenon in a small sub-class of organic semiconductors by which a singlet exciton splits into two triplet excitons [12]. The process of singlet exciton fission has recently been proposed as a means to achieve very high external quantum efficiencies (EQE) in organic optoelectronic devices such as photodetectors and photovoltaic cells [13-15]. Due to the limited number of materials that exhibit singlet exciton fission [12], it is challenging to achieve high photon absorption, long exciton diffusion lengths, efficient charge separation, charge transport, and singlet fission in a single organic semiconductor. The process of singlet fission is de-coupled from photon absorption, exciton diffusion, and charge transport by inserting a singlet fission material at the donor-acceptor (D-A) interface of an organic photovoltaic cell [16]. Singlet excitons generated in the singlet exciton donor Förster resonance energy transfer (FRET) to the singlet fission material where they undergo singlet fission. This interlayer acts as a singlet fission sensitizer to the singlet donor. In

this device structure, the singlet donor can be chosen for high photon absorption, exciton diffusion, and charge transport, and the singlet fission sensitizer can be selected for high singlet fission efficiency to achieve very high EQE organic photovoltaic cells.

2.1.1 Singlet Exciton Fission

Singlet fission is a process that splits a singlet (spin 0) exciton into two triplet (spin 1) excitons, Fig. 2.1(a). This process can lead to multiple electrons per absorbed photon, promising for photovoltaics with efficiencies beyond the Shockley-Queisser (SQ) limit [11]. In a conventional single-junction solar cell, an electron-hole pair photoexcited with energy above the bandgap loses its extra energy via thermalization. Singlet exciton fission instead splits a high-energy excited state into two low-energy states, generating one extra exciton per absorbed photon, which would have been otherwise wasted as heat.

Although the transition between singlet and triplet states is disallowed by the conservation of spin symmetry, a pair of triplets can have some singlet character; therefore, singlet fission, the conversion of a singlet into a pair of triplets, can be a spin- allowed process. If the energy of the singlet exciton is approximately twice the energy of the triplet, singlet fission can be very fast, hence outcompeting other decay channels, including prompt fluorescence.

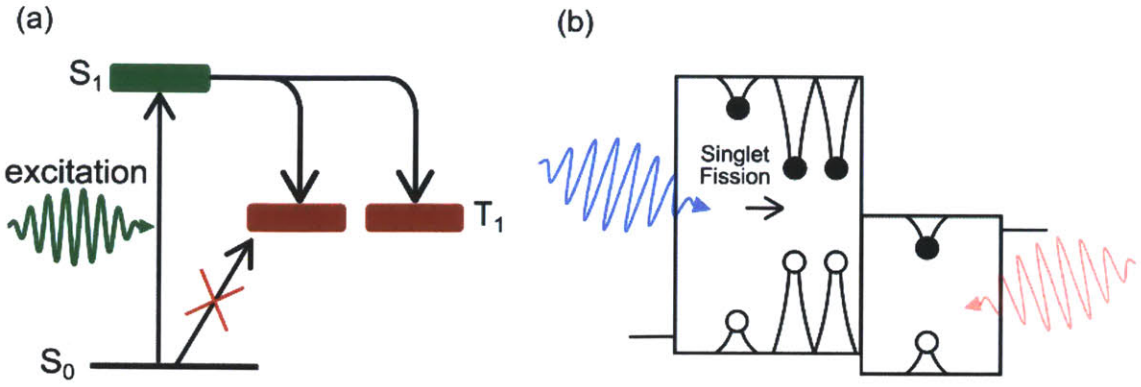

Fig. 2.1 (a) Energy diagram and excited state transitions in singlet exciton fission materials. Photoexcitation of singlet can split into a pair of triplet states. (b) A device structure for singlet fission based solar cells. The high energy singlet fission donor is combined with a low photon energy absorber acceptor to absorb all solar light to the triplet energy.

The triplet excitons produced by fission have roughly half the energy of the initial singlet excitation. Consequently, fission limits the open circuit voltage of the cell to no more than half its previous value. Triplet excitons are, however, also dark states; the absorption in the spectral region between the singlet and triplet excitons is spin-forbidden. This spectral region must be filled by combining the high energy singlet fission absorber with another material that captures low-energy photons. Otherwise, the singlet-fission photovoltaic system will double the photocurrent, but also cut the voltage by half, leading to no net benefit in the power conversion efficiency. See Fig. 2.l(b) for an example of device structures featuring singlet fission donors and low bandgap acceptors. As shown in Fig. 2.2, singlet fission solar cells with absorption in the singlet-triplet gap can bring the SQ limit to 41% from 33% of conventional single-junction solar cells.

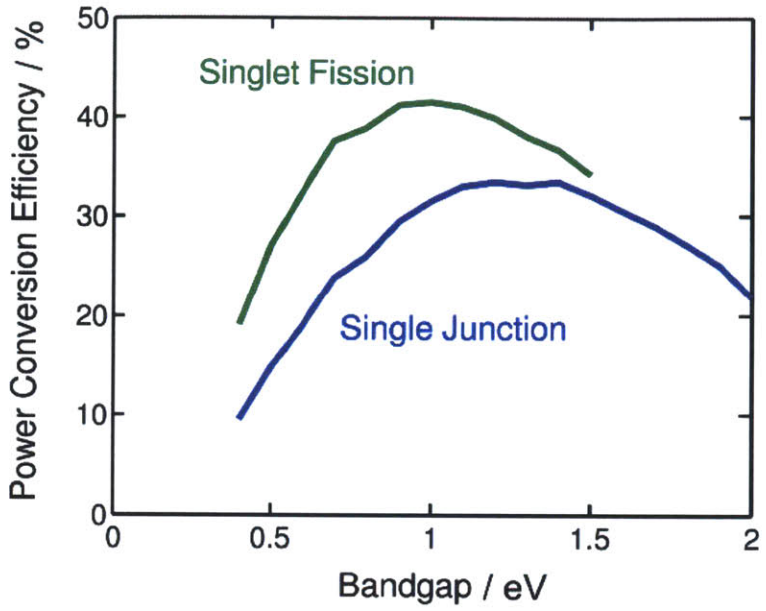

Fig. 2.2 Theoretical maximum power efficiency as a function of bandgap energy for single junction solar cell (blue) and for a singlet exciton fission solar cell (green).

2.1.2 Förster Resonance Energy Transfer

Förster resonance energy transfer (FRET) is a fast and efficient process by which energy can be transferred from a donor chromophore, D, to an acceptor chromophore, A, over a relatively long distance (~ 5-10 nm). Förster energy transfer is a non-radiative process mediated by a virtual photon through dipole-dipole interactions between the donor and acceptor molecules, Fig. 2.3(a). The efficiency of the process depends on the overlap between the acceptor absorption cross-section spectrum, $\sigma_A(\lambda)$, and donor emission spectrum, $F_D(\lambda)$, schematically shown in Fig. 2.3(b).

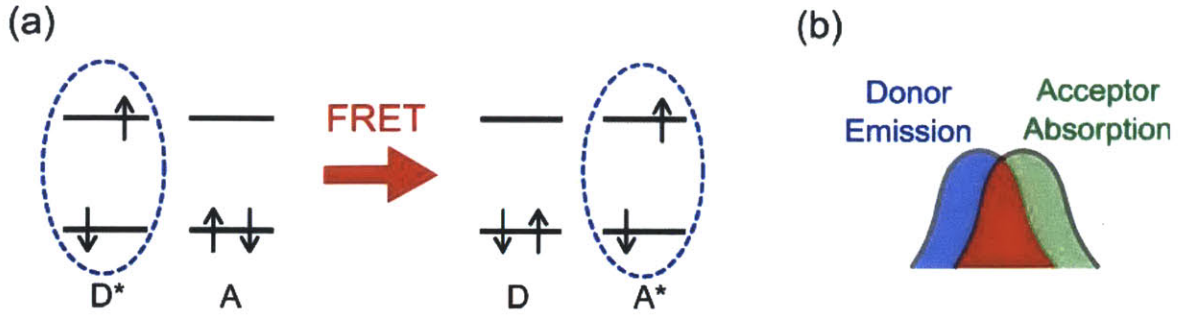

Fig. 2.3 (a) The process of Förster energy transfer. Energy is transferred from an excited donor (D) chromophore to an acceptor (A) chromophore without the emission of a photon. (b) The rate and hence efficiency of Förster energy transfer depends on the spectral overlap between the emission and absorption of the donor and acceptor respectively.

The transfer rate in the dipole-dipole approximation can be derived from Fermi's golden rule and can be expressing in the experimental parameters as:

$$k_f = \frac{9\eta_{fl}\kappa^2}{128\tau_{fl}\pi^5 n^4 d^6}\int \lambda^4 F_D(\lambda)\sigma_A(\lambda)\mathrm{d}\lambda \qquad (2.1)$$

Here, n is the refractive index, d is the molecular separation, κ is the dipole orientation, η_{fl} is the photoluminescence quantum yield, λ is the wavelength, and τ_{fl} is the photoluminescence lifetime. A more convenient way to express the rate of energy transfer is:

$$k_f = \frac{1}{\tau_{fl}}\left(\frac{R_0}{d}\right)^6 \qquad (2.2)$$

where R_0 is defined as the Förster radius. It is clear from Eq. 2.2 that for efficient energy transfer, $d < R_0$ or the separation between donor and acceptor chromophores should be within a Förster radius. R_0 is typically in the range of 5-10 nm.

2.1.3 Organic Solar Cell Operation

Fig. 2.4 illustrates the photocurrent generation process of organic solar cells. Photon absorption creates a bound electron-hole pair, or exciton. In organic molecules, the exciton has a high binding energy up to 1 eV and therefore cannot be dissociated by the internal electric field. The excitons diffuse toward the donor-acceptor heterojunction. The energy offset at the interface dissociates the strongly bound excitons in organic molecules with near unity efficiency. Excitons are separated into charge transfer states, which are bound electron-hole pairs across the junction. The charge transfer states can be dissociated into free carriers, which ultimately generate photocurrent. A singlet exciton fission donor material must be efficient at all of these steps plus singlet exciton fission.

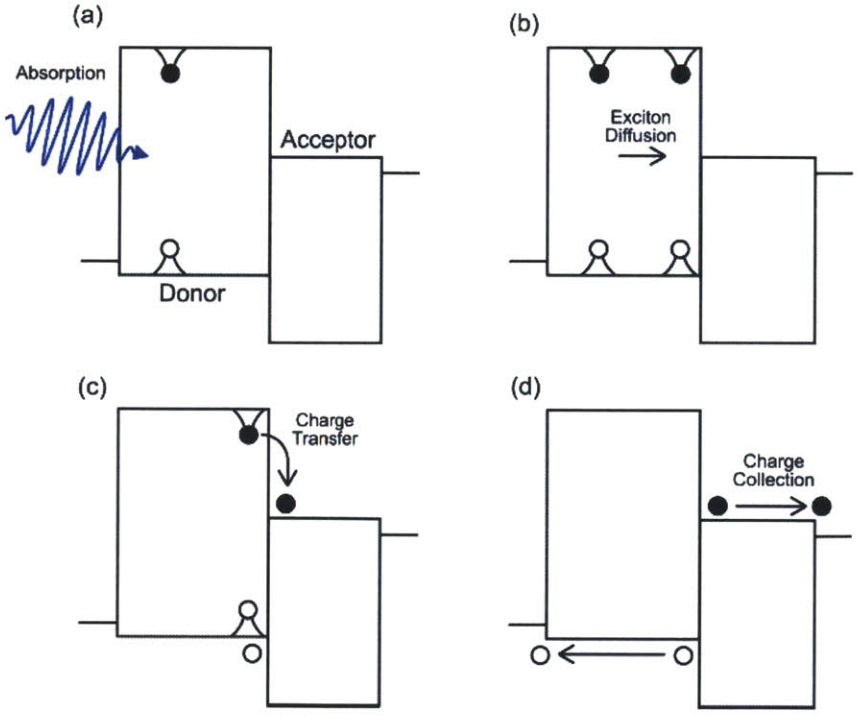

Fig. 2.4 The operating principle of organic bilayer solar cells. (a) Upon light absorption, an exciton is created. (b) Excitons diffuse to the interface. (c) Excitons are dissociated into charges at the donor-acceptor interface. (d) Charges are extracted to the electrodes.

2.2 Singlet Exciton Fission Sensitization

In the present work, the singlet donor tris[4-(5-phenylthiophen-2-yl)phenyl]amine [17] (TPTPA) is sensitized with the singlet fission material 5, 6, 11, 12-tetraphenylnaphthacene [18] (rubrene). As shown in Fig. 2.5, the sensitization process begins with the absorption of light by TPTPA, resulting in singlet exciton formation. The singlet exciton then diffuses to the TPTPA-rubrene interface which is then transferred to the singlet state of rubrene by FRET due to the energy alignment of the singlet state of TPTPA (S_{TPTPA} = 2.8 eV) estimated from fluorescence, and rubrene ($S_{rubrene}$ = 2.3 eV) [18]. The singlet in rubrene then undergoes singlet exciton fission. The process is conditional on the energy of the first excited state being approximately twice the energy of the first triplet ($T_{rubrene}$ = 1.2 eV) [18]. If the two triplet excitons are dissociated, one photon absorbed can result in two charge carriers, potentially doubling the EQE in the absorption region of TPTPA. In order to facilitate charge extraction after exciton dissociation, the highest occupied molecular orbital (HOMO) of the singlet fission layer should be equal to or deeper than the singlet donor. In this work, TPTPA and rubrene both have HOMO levels of approximately 5.4eV [19, 20].

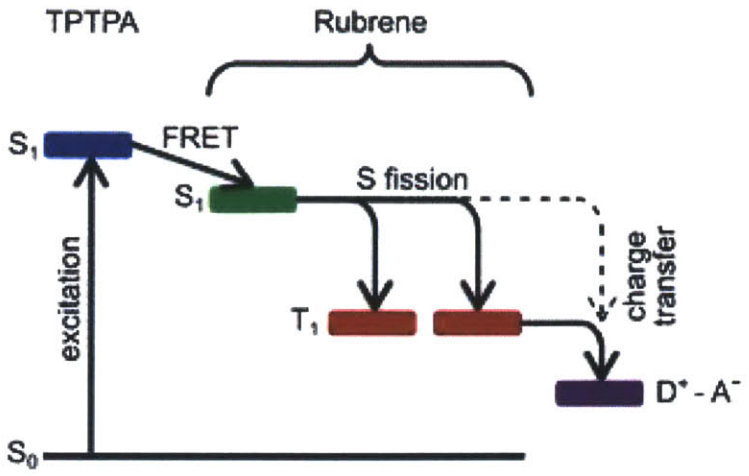

Fig. 2.5 A schematic representation of singlet fission sensitization scheme in an organic photovoltaic cell (OPV). Radiation is absorbed by the singlet donor, TPTPA, resulting in singlet generation. The singlet diffuses to the interface and energy transfers to the singlet fission sensitizer layer, rubrene. The singlet on the sensitizer then undergoes singlet exciton fission resulting in two triplets. The triplets then dissociate at the donor-acceptor (D-A) interface resulting in two charge carriers from one photon absorbed in the singlet exciton donor. If the rate of singlet fission is comparable to the rate of singlet charge transfer, direct singlet dissociation (dashed arrow) at the D-A interface may occur.

2.2.1 Optical Characterization

Before OPV device fabrication, photoluminescence (PL) of a co-deposited film on glass of TPTPA(30%): rubrene(70%), by volume, was measured to characterize energy transfer from TPTPA to rubrene. The absorption coefficients and PL of TPTPA and rubrene are shown in Fig. 2.6(a). TPTPA absorbs broadly in the region from 350 nm $< \lambda <$ 450 nm while rubrene absorbs light in the region from 450 nm $< \lambda <$ 550 nm. Ideally, the singlet donor's absorption peak would be slightly higher in energy than the absorption peak of the singlet fission sensitizer for efficient exciton transfer while maintaining broad solar absorption. To study singlet fission sensitization, TPTPA and rubrene were chosen for non-overlapping absorptions to allow for selective material

excitation. When TPTPA is photoexcited (λ = 349 nm) in the co-deposited thin film, TPTPA's fluorescence is fully quenched as singlets on TPTPA are transferred to rubrene as shown in Fig. 2.6(a).

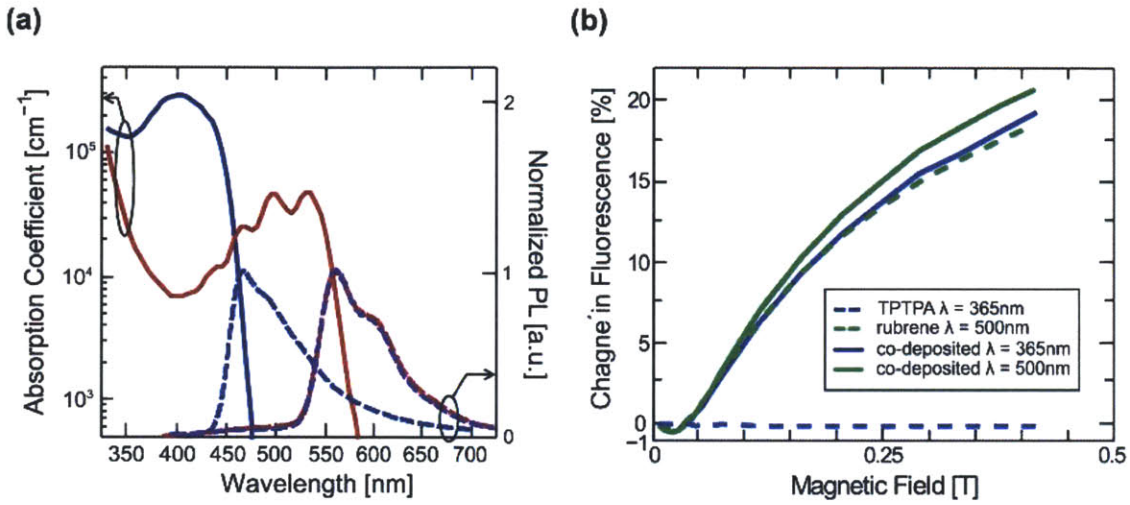

Fig. 1.6 (a) Absorption coefficient (solid line) and normalized PL (dashed line) photoexcited at λ = 349 nm of TPTPA (blue) and rubrene (red) thin films. In a co-deposited film of TPTPA (30%):rubrene (70%), TPTPA's fluorescence is fully quenched as singlets are transferred to rubrene (violet). **(b)** The change in fluorescence under varying applied magnetic fields of photoexcited (λ = 500 nm) neat rubrene (green dashed line) showing a typical curve of singlet fission to two triplets. Photoexcitation of TPTPA (λ = 365 nm) and rubrene (λ = 500 nm) in the ensemble film, the fluorescence increases by 19% (blue solid line) and by 21% (green solid line) respectively, confirming singlet exciton fission. Neat TPTPA, photoexcited at λ = 365 nm, shows no magnetic field dependent changes in fluorescence (blue dashed line), demonstrating singlet exciton fission sensitization via exciton energy transfer from TPTPA to rubrene.

The process of singlet exciton fission is unaffected by the method of populating singlets (direct photoexcitation versus FRET) in rubrene as shown in Fig. 2.6(b) by magnetic field dependent change in fluorescence in luminescent thin films. The magnetic field was applied parallel to the film plane. In the co-deposited film, photoexcitation of TPTPA (λ = 365 nm) and subsequent energy transfer to rubrene produces an increase in fluorescence of 19%, and direct photoexcitation of rubrene (λ = 500 nm) produces an increase in fluorescence of 21%. The shapes of these curves with zero crossings at low fields are typical of singlet exciton fission into two triplets [18, 21]. The increase in fluorescence is due to the rate of singlet fission decreasing under high magnetic fields (H > 0.2 T) allowing for singlet exciton processes such as fluorescence to compete more efficiently with fission [22]. The measured changes in fluorescence of the co-deposited film are consistent with those of neat rubrene (λ = 500 nm) [Fig. 2.6(b)]. Neat TPTPA photoexcited (λ = 365 nm) under a varying magnetic field, as seen in Fig. 2.6(b), shows no magnetic field dependent fluorescence. The introduction of magnetic field dependent changes of fluorescence in photoexcited TPTPA demonstrates singlet fission sensitization via exciton energy transfer.

2.2.2 Electrical Characterization

To investigate the effect of singlet exciton fission sensitization in OPVs, we built bilayer heterojunction devices composed of the singlet donor, TPTPA, the singlet fission sensitizer, rubrene, and a perylene diimide, ActivInk N1400 (PDI-CN2) purchased from Polyera, as the electron acceptor. The charge transfer state energy of the OPV must be lower than the triplet energy in the fission material to ensure triplet dissociation at the D-A interface [23]. The electron acceptor was chosen for this reason due to its lowest unoccupied molecular orbital (LUMO) level

of 4.3 eV [24]. Devices were fabricated on indium tin oxide (ITO) coated glass substrates. The substrates were cleaned with detergent and solvents and exposed to an O_2-plasma prior to deposition. All organic layers were grown using thermal evaporation under high vacuum (~ 10^{-6} Torr). The cathode was defined by a 1-mm-diameter shadow mask. The device structure was as follows: ITO (160 nm)/MoO_3 (8 nm)/TPTPA (25 nm)/Rubrene (7 nm)/PDI-CN2 (20 nm)/Bathocuproine (BCP) (7 nm)/Ag (100 nm). The energy level diagram for these devices can be seen in Fig. 2.7(a) [19, 20, 24-26]. Control devices without the singlet fission sensitizer interlayer were also grown for comparison.

Current-density-voltage (*J-V*) curves are shown in Fig. 2.7(b) for devices with and without fission sensitization layer, performed under AM1.5G illumination (100 mW-cm^{-2}). Devices with no fission sensitizer exhibit short-circuit current density J_{SC} = 0.52 mA-cm^{-2}, open-circuit voltage V_{OC} = 0.49 V, fill factor *FF* = 0.53, and power conversion efficiency *PCE* = 0.14%. Devices with the rubrene sensitizer layer exhibit J_{SC} = 0.88 mA-cm^{-2}, V_{OC} = 0.55 V, *FF* = 0.59, and *PCE* = 0.29%. Similar V_{OC} in the control and sensitized devices indicate the HOMOs of TPTPA and rubrene are close in energy. Also, the *FF* enhancement indicates no obstruction to charge extraction at the TPTPA/rubrene interface. With the fission sensitizer layer, the J_{SC} and *PCE* show enhancements of 69% and 107% respectively compared to the control devices.

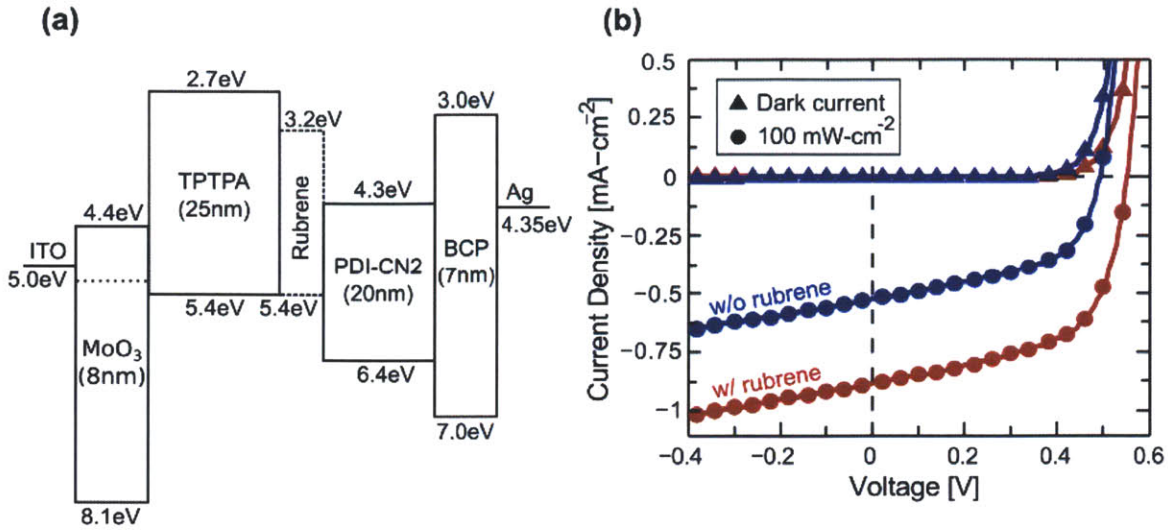

Fig. 2.7 (a) Schematic energy-level diagram and thicknesses of the OPV devices built. The energy-levels are from Ref. 19, 20, 24-26. **(b)** The measured dark (triangles) and light (100 mW-cm^{-2}) (dots) current-density-voltage (*J-V*) of the OPV device with rubrene (red) and without rubrene (blue).

To understand the mechanism of enhancement in J_{SC}, EQE versus wavelength was measured using a xenon lamp with monochromator, a chopper set to f = 200Hz, and a lock-in amplifier. Light intensity was measured using a calibrated silicon photodiode. For EQE measurements at approximate solar operating conditions, the devices were illuminated with a tungsten light source at 50 mW-cm^{-2}. EQE curves are shown in Fig. 2.8 for devices with and without fission sensitization layer. As expected, direct photoexcitation of rubrene adds to the PDI-CN2 photocurrent in the wavelength range of 450 nm < λ < 550 nm, increasing the EQE in this region from 5.0% to 8.9% when rubrene is introduced. The EQE in the wavelength range of 350 nm < λ < 450 nm, associated with TPTPA, exhibits a peak enhancement from 12.8% to 27.6% upon introduction of rubrene.

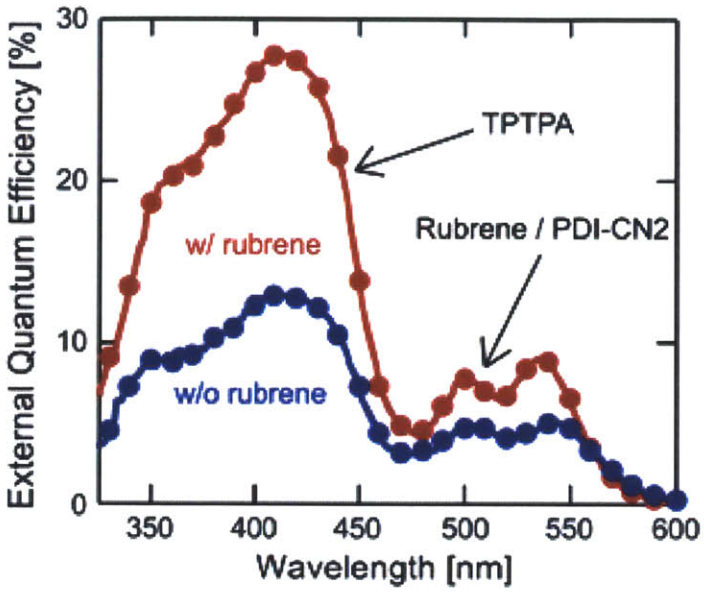

Fig. 2.8 The measured external quantum efficiency (EQE) versus wavelength curves of the OPV device with rubrene (red dots) and without rubrene (blue dots) showing enhancement in the TPTPA region due to singlet fission sensitization via rubrene.

Although, the rubrene interlayer in this work is designed as a singlet fission sensitizer to the singlet donor, TPTPA, it can also act to enhance exciton separation as shown in Ref. 27. To confirm singlet exciton fission contributes to the enhancement in EQE of the TPTPA region, magnetic field dependent photocurrent measurements were performed, shown in Fig. 2.9. The magnetic field was applied parallel to the device plane. Photoexcitation of TPTPA (λ = 365 nm) produces a decrease in photocurrent of 14% because TPTPA singlets undergo energy transfer to rubrene where they are split into triplets. The decrease in photocurrent under high magnetic fields is analogous to the increase in fluorescence shown previously for mixed TPTPA/rubrene films. The magnetic field effect on photocurrent is due to a decrease in the rate of singlet exciton fission under high magnetic fields (H > 0.2 T). This allows singlet exciton processes such as direct singlet charge transfer, which produces one charge carrier per singlet, to compete more

efficiently with singlet exciton fission and triplet charge transfer, which produces two charge carriers per singlet, reducing the observed photocurrent [13]. Direct photoexcitation of rubrene (λ = 500 nm) produces a decrease in photocurrent of 8.7%. The magnitude of the change is smaller due to competing optical absorption by PDI-CN2 at the same wavelength. The control device without rubrene shows no magnetic field dependent photocurrent in the TPTPA region (λ = 365 nm) or the PDI-CN2 region (λ = 500 nm). The magnetic field dependent photocurrent in the TPTPA region confirms the presence of singlet exciton fission via the rubrene sensitizer layer.

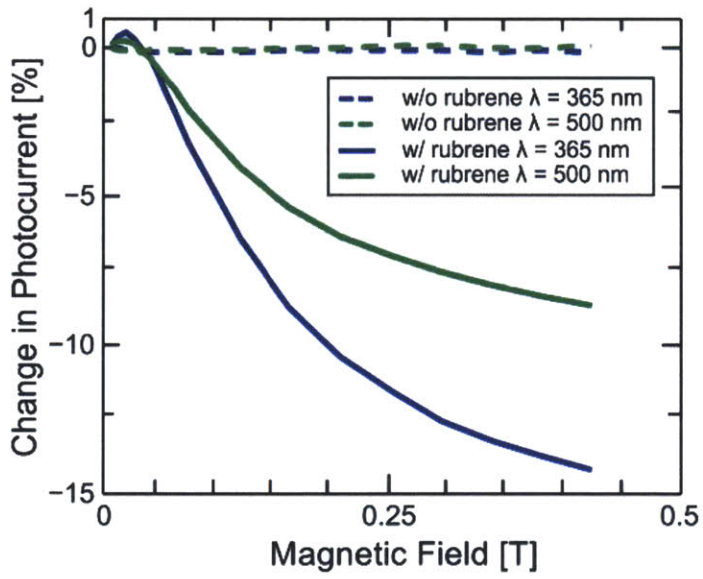

Fig. 2.9 The change in photocurrent under varying applied magnetic fields at short circuit conditions for OPV with rubrene (solid line) and without rubrene (dashed line) interlayer. For the device with rubrene, the photocurrent decreases by 14% under illumination at λ = 365 nm (solid blue line) of the TPTPA layer. The photocurrent decreases by 8.7% under illumination at λ = 500 nm (solid green line) of the rubrene and PDI-CN2 layers. The magnitude of change is smaller due to the PDI-CN2 component of photocurrent being magnetic field independent. In contrast, the device without rubrene shows no magnetic field dependent photocurrent at λ = 365 nm (dashed blue line) or λ = 500 nm (dashed green line), confirming singlet exciton fission sensitization of TPTPA via rubrene in an OPV.

To demonstrate the generality of this proposed scheme, Congreve et. al. [28] applied singlet sensitization to the well-studied polymer solar cell donor P3HT and the efficient singlet fission material pentacene. The device structure used can be seen in Fig. 2.10(a). They measured the EQE (Fig. 2.10(b)) for a device that features a 15-nm-thick pentacene layer. The EQE at normal incidence is (82 +/- 1)% at the peak pentacene absorption wavelength λ = 670 nm. Optical modeling predicts that the internal quantum efficiency (IQE), which is defined as the number of electrons collected per photon absorbed, for photoexcitation of pentacene and P3HT is (160 +/- 10)% and (150 +/- 10)%, respectively. The IQE of pentacene in this structure is approximately double that reported previously for pentacene, and the high IQE of P3HT is consistent with the expected sensitization of P3HT by pentacene, as singlet excitons generated in P3HT are transferred to pentacene and then split into triplets [16]. As far as we know, this is the first time more than one electron generated per photon absorbed has been demonstrated in a material that does not exhibit a multiple carrier multiplication process.

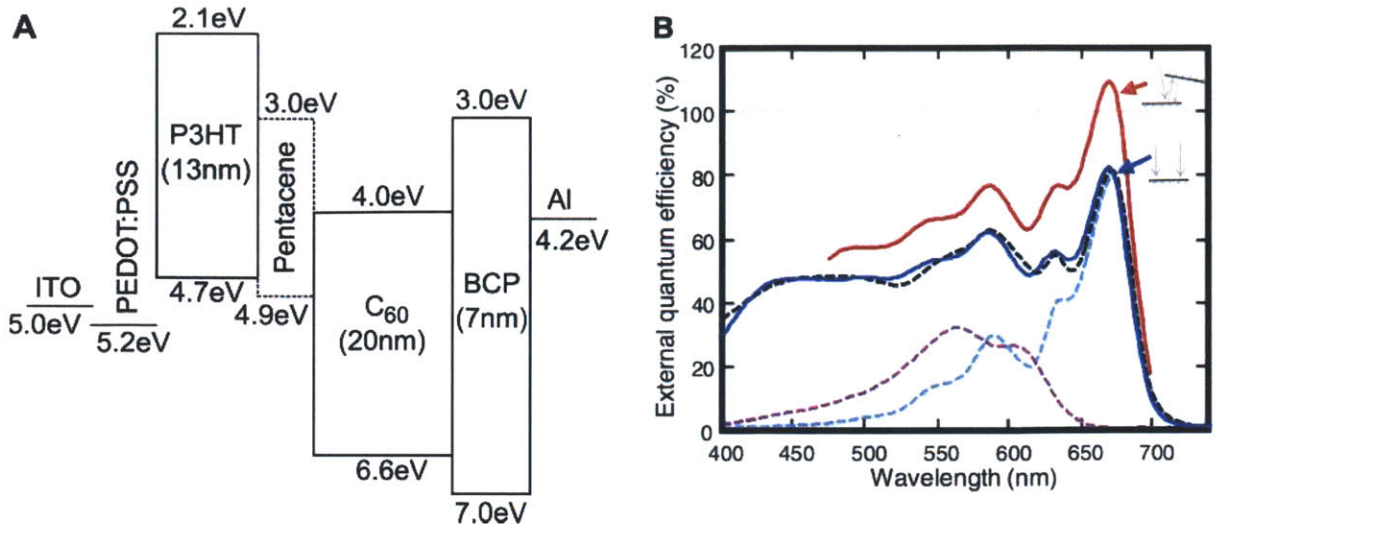

Fig. 2.10 (a) Device architecture and EQE of a pentacene solar cell. (A) Architecture of the solar cell with the thickness of each layer in nanometers and energy levels of the lowest unoccupied and highest occupied molecular orbitals in electron volts. The anode is composed of indium tin oxide (ITO) and poly(3,4-ethylenedioxythiophene) poly(styrenesulfonate) (PEDOT:PSS). The cathode employs bathocuproine (BCP) and a silver cap. **(b)** External quantum efficiency of devices without optical trapping (blue line), and device measured with light incident at 10° from normal with an external mirror reflecting the residual pump light (red line). Optical fits from IQE modeling are shown with dashed lines: modeled pentacene EQE (blue dashes), modeled P3HT EQE (purple dashes), and modeled device EQE (black dashes) for comparison to the measured device efficiency without optical trapping.

We also studied the magnetic field dependence of P3HT within the device structure shown in Fig. 2.10(a) to confirm that excitons generated in P3HT can be transferred to pentacene and subsequently split into two triplets, resulting in P3HT IQEs above 100%. The wavelength dependence of the magnetic field effect is shown in Fig. 2.11 and observed to be correlated with the optical absorption of pentacene and P3HT. Devices fabricated with only P3HT and C60 active layers, illuminated at $\lambda = 530$ nm, had no magnetic field dependence, demonstrating that there is no singlet fission in the absence of pentacene. This is consistent with prior studies that

found no singlet fission in regio-regular P3HT, but suggested that singlet fission can occur in regio-random P3HT only under illumination of high energy photons (34). Excitation of the acceptor in any device structure resulted in no magnetic field modulation of photocurrent.

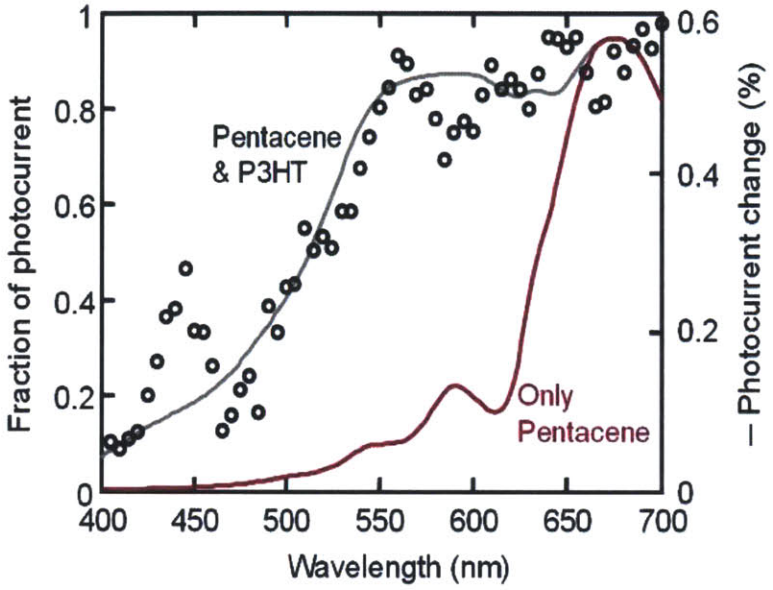

Fig. 2.11 The absolute value of the change in photocurrent as a function of wavelength (○) for a solar cell with a 5-nm-thick pentacene film, so chosen to enhance the magnetic field effect. The shape is very similar to the fraction of photocurrent due to P3HT and pentacene (—) and distinct from the photocurrent contribution only from pentacene (—). The similarity is a secondary proof that P3HT is sensitized by pentacene.

2.3 Conclusion

In summary, we have shown an enhancement in EQE in an OPV device due to singlet fission sensitization. The enhancement in peak EQE in the spectral region associated with the singlet exciton donor, TPTPA, increased from 12.8% to 27.6% upon introduction of the rubrene singlet exciton fission sensitization layer. The presence of singlet exciton fission via energy transfer from TPTPA to rubrene was demonstrated in a fluorescent thin film and in a OPV device by magnetic field dependent changes in fluorescence, 19%, and photocurrent, -14%, respectively. The generality of the scheme has been demonstrated with multiple singlet donors and singlet fission sensitizers. An IQE of >100% has been demonstrated with this scheme, with a material that does not exhibit multiple carrier multiplication for the first time. In the device structure introduced here, the singlet donor can be chosen for high photon absorption, long exciton diffusion, and efficient charge transport and the singlet fission sensitizer can be selected for high singlet fission efficiency for organic photovoltaic cells with EQEs potentially approaching 200%.

Chapter 3

Monte Carlo Ray Tracing Model of Luminescent Solar Concentrators

Predicting the performance of a LSC

3.1 The Luminescent Solar Concentrator

The luminescent solar concentrator (LSC) [29] can address the high costs faced by geometric concentrators and potentially exceed them in performance.

3.1.1 The anatomy of an LSC

A LSC is a conceptually simple optical device, illustrated in Fig. 3.1.a, which aims to reduce the cost of solar electricity by using an inexpensive collector to concentrate solar radiation without mechanical tracking [29-32]. An LSC consists of an optically clear waveguide with a refractive index greater than 1 such as glass or polymer. This waveguide is doped or coated with a luminescent chromophore that can efficiently absorb and re-emit light. Examples of luminescent chromophores used in LSCs are organic molecules (fluorescent, phosphorescent) [32, 5], inorganic semiconductors (quantum dot) [33, 34], or ions (transition metal, lanthanide) [35, 36]. A solar cell is attached to the edge of the waveguide to absorb the luminescence and convert it to electrical energy. Examples of visible light absorbing and emitting LSCs are shown in Fig. 3.1.b. Since the facial area of the concentrator is larger than the area of the concentrator edge (solar cell area), light can be concentrated. The geometric concentration factor, G, of an

LSC is the ratio of the concentrator area to the solar cell area. For the square LSC in Fig. 3.1.a, $G = \frac{L}{D}$, where L is the length of a side and D is the thickness of the waveguide.

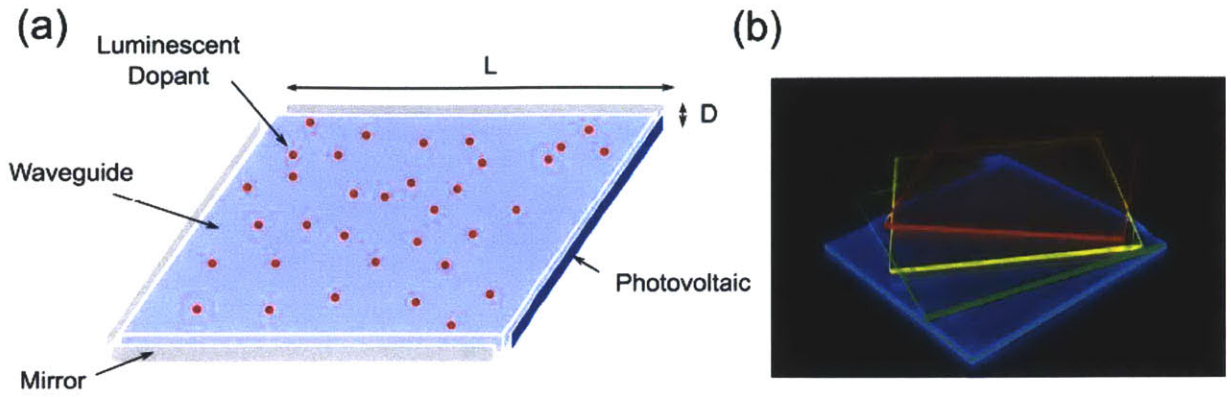

Fig. 3.1 (a) Schematic of a luminescent solar concentrator, composed of an optical waveguide, a chromophore that absorbs and emits light, and a solar cell. (b) Photograph of organic solar concentrators illuminated by UV light in the dark. (Soft Semiconductor lab)

3.1.2 The optical efficiency of an LSC

Fig. 3.2 illustrates the relevant optical processes that define the efficiency of a luminescent solar concentrator [30, 31]. Incident solar radiation is absorbed at energy, ε_1, by the luminescent chromophore with an efficiency of η_A. The absorbed photon is re-emitted at a lower energy, ε_2, as photoluminescence with an efficiency of η_{PL}. The remaining energy is dissipated as heat. Photoluminescence that has a Poynting vector of $\theta_k > \theta_C$, where θ_C is the critical angle for total internal reflection, is confined within the waveguide. The trapping efficiency of an isotropic emitter is given by

$$\eta_T = \sqrt{1 - \left(\frac{1}{n_S}\right)^2} \tag{3.1}$$

where n_s is the waveguide refractive index. For a refractive index of 1.5, the trapping efficiency is 75%. Ideally, this photoluminescence will waveguide to the edges with an overall efficiency of

$$\eta_{LS}{}^{C} = \eta_A \eta_{PL} \eta_T \tag{3.2}$$

The waveguided photoluminescence generates photocurrent via the attached solar cell. The LSC allows light to be concentrated with a cheap, flat plate, thereby reducing the required area of expensive solar cells and consequently, the cost of solar energy production.

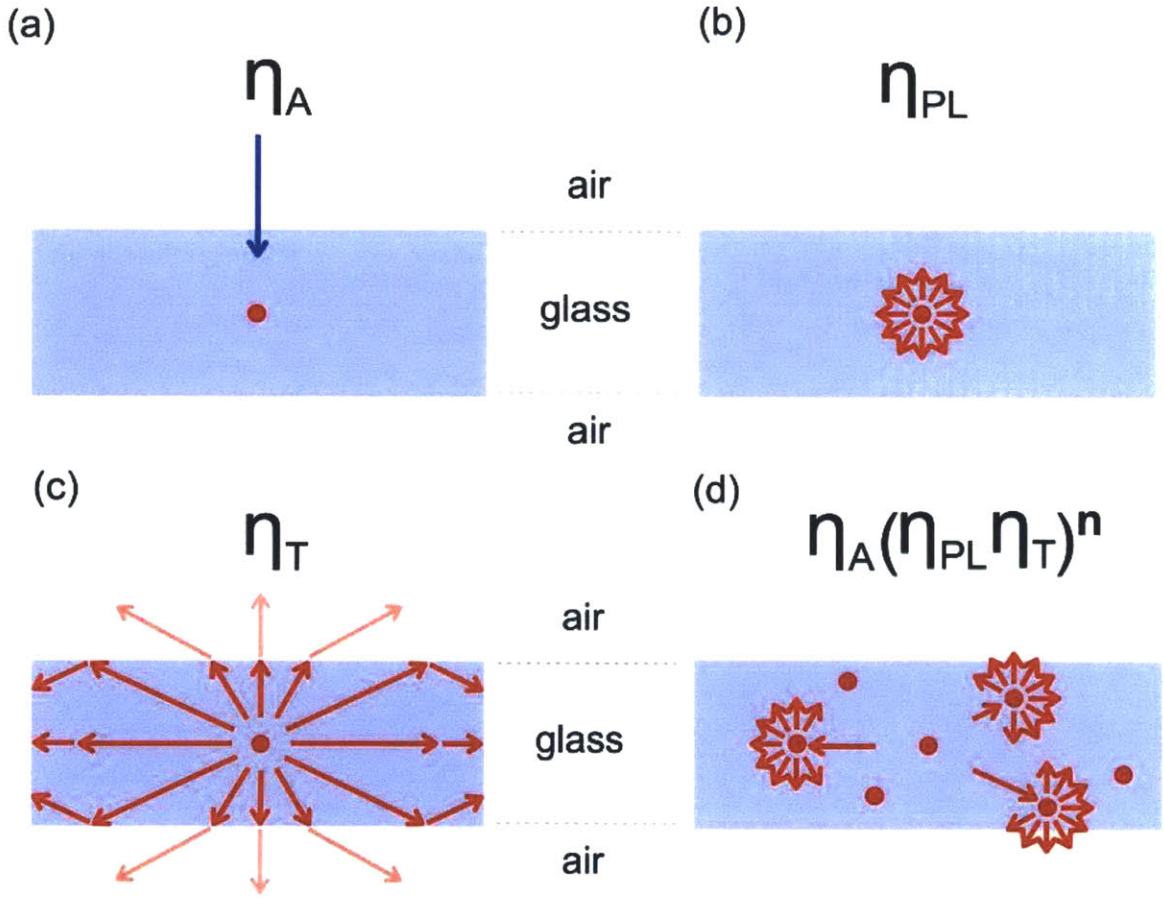

Fig. 3.2 The operating principle of luminescent solar concentrators. (a) Light absorption by the luminescent chromophore. (b) The absorbed photon is re-emitted as photoluminescence. (c) A large fraction of the photoluminescence is trapped within the waveguide due to total internal reflection. (d) Transport losses such as self-absorption lead to additional photon events causing the LSC efficiency to decrease exponentially.

3.1.3 The benefits of a luminescent solar concentrator

The advantages of a luminescent solar concentrator over conventional geometric concentrators are numerous, but largely address the problem of maintenance costs in imaging concentrators.

- Luminescent solar concentrators are compatible with large scale manufacturing techniques such as glass and polymer casting, and thin film coating processes such as thermal evaporation and solution casting. These optical devices also do not depend on scarce resources making them attractive for large scale production at low costs.
- Luminescent solar concentrators are non-imaging concentrators, hence do not require solar tracking, and are compatible with both direct and diffuse sunlight. This significantly reduces the complexity relative to imaging concentrators that require single to multi-axis solar tracking.
- The chromophore's luminescence and solar cell's bandgap can be tuned to be energetically identical. This energy matching means that cooling is not required due to excess solar energy being dissipated as heat in the optical concentrator and only electrical energy is produced in the solar cells.
- Solar cells wired in series are highly sensitive to defects such as shadowing, uneven illumination, and cell variability due to the current matching requirement. Luminescent solar concentrators are insensitive to these defects due to the isotropic chromophore luminescence that ensures uniform illumination of the solar cells.
- Solar cells require electrodes that are traditionally opaque. When integrated into consumer products such as windows for automobiles and homes, the metal grids can be dis-pleasing to the eye due to the opacity. Luminescent solar concentrator's optical

density and spectral properties can be tuned to both absorb and transmit light to the user for attractive building integrated energy harvesting.

Despite these advantages, luminescent solar concentrators have yet to penetrate the commercial energy market. The main factor limiting LSCs since their inception is photoluminescence self-absorption. Photoluminescence self-absorption is the result of finite overlap between the chromophore's absorption and luminescence, schematically shown in Fig. 3.3. As the photoluminescence propagates within the waveguide, it can be re-absorbed by other chromophores due to the finite Stokes shift. Self-absorption results in an additional photon emission event shown schematically in Fig 3.2.d. The LSC efficiency consequently decreases exponentially with the number of re-absorption events, n:

$$\eta_{LS}{}^{C} = \eta_A(\eta_{PL}\eta_T)^n \tag{3.3}$$

This process is termed a transport loss, because it scales with the geometric gain or optical pathlength of the waveguided photoluminescence.

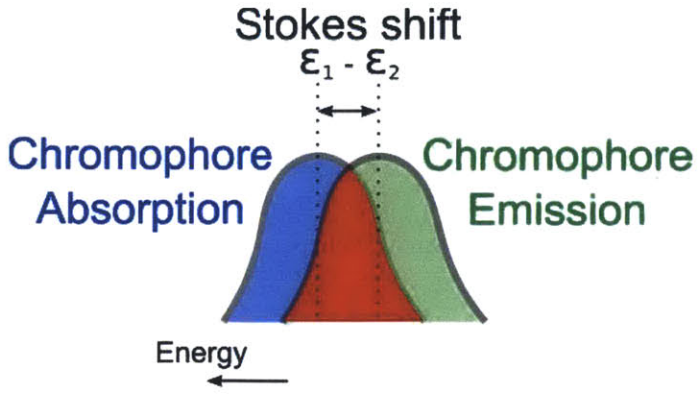

Fig. 3.3 Schematic of the Stokes shift in a chromophore's absorption (blue) and photoluminescence (green). The overlap between absorption and emission (red) leads to the transport loss called self-absorption that limits the achievable concentration of LSCs.

Significant progress has been made on the problem of self-absorption. The main two strategies to reduce self-absorption have done so by increasing the chromophore's Stokes shift. The first method is to use emitters that have inherently large Stokes shift such as organic phosphorescent emitters [5] and lanthanide ions (e.g. neodymium or europium). The second method is to make use of energy transfer techniques such as FRET to engineer the effective Stokes shift. Currie et al. [5] used a high concentration of a donor chromophore to act as a solar absorber doped with a small amount of an acceptor chromophore to act as the emitter at a lower energy. By minimizing the concentration of the emitter, the effective Stokes shift was increased significantly compared to the donor chromophore. Mulder et al. [37] applied this concept to bulk cast LSCs with molecular aggregates. This separation of roles (absorber/emitter) via energy transfer has been recently applied to an attractive LSC chromophore, luminescent colloidal nanocrystals, which have high self-absorption, but tunable and efficient photoluminescence. By doping a nanocrystal with the luminescent ion Mn^{2+}, Erickson et al. [35] have shown low self-absorption where the nanocrystal takes the role of donor and the ion as the acceptor. Meinardi et al. [33] and Coropceanu et al. [34] recently demonstrated low self-absorption colloidal core/shell nanocrystals for LSCs where a thick shell acts as the solar absorber which transfers the energy to the core emitter. Engineered low self-absorption emitters are also relevant to downshifting technologies such as displays, spectrally broad photodetectors, and cascade energy transfer.

3.2 Monte Carlo Ray Tracing Model for LSC

Monte Carlo simulations are a broad class of computational algorithms that rely on repeated random sampling to obtain numerical results. Due to the randomness and probabilistic nature, the name of this class of algorithm is taken from the famous Monte Carlo gambling casino. The simulations are often used in physical and mathematical problems and are most useful when an exact solution is difficult or impossible to obtain. Sawilowski defines the Monte Carlo simulation as a fictitious representation of reality which uses repeated sampling to determine the properties of some phenomenon.

3.2.1 Monte Carlo ray tracing

Although, exact solutions of Maxwell's equations for waveguides used in luminescent solar concentrators are well known, the analysis becomes difficult when including dipole absorption and re-emission. Due to this complexity, LSCs are well suited to be simulated by a Monte Carlo ray tracing model. The physical processes that define a LSC are photon propagation, absorption, photoluminescence, non-radiative recombination, reflection, and refraction. A flow diagram of the Monte Carlo ray tracing model can be seen in Fig. 3.4. In this model we treat photon absorption, photoluminescence, and reflection/refraction as binary processes determined probabilistically based on the relevant physical equations and experimental parameters describing energy flow. By repeated sampling, this binary path converges to the actual energy transfer behavior in a luminescent solar concentrator.

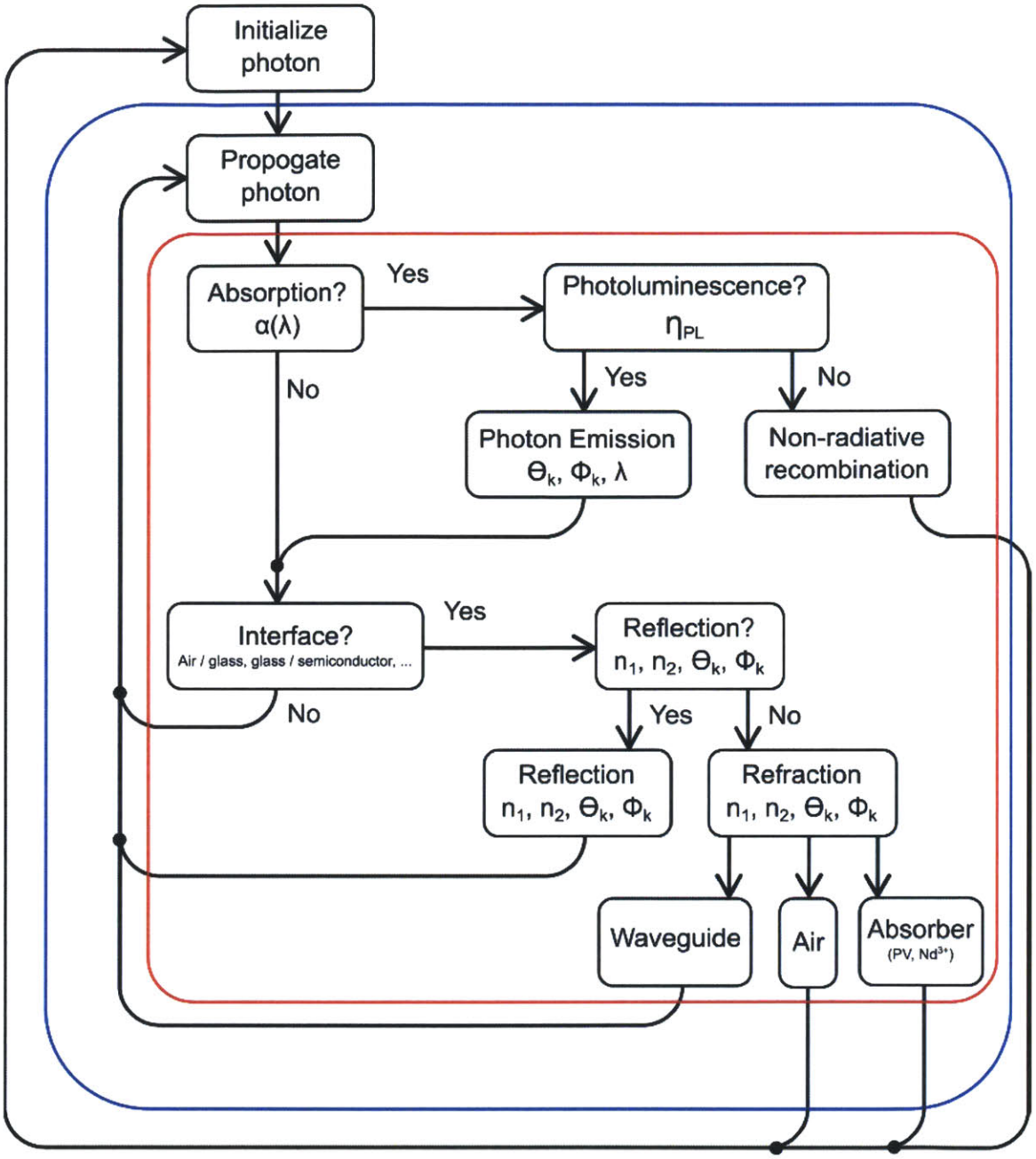

Fig. 3.4 Flow diagram of Monte Carlo ray tracing program. Absorption, photoluminescence, reflection/refraction are treated as probabilistic phenomena. By repeated sampling, the physical behavior of LSCs can be predicted without significant computation.

3.2.2 Absorption Probability

For both an incident solar photon and waveguided photoluminescence, the absorption probability can be calculated using the Beer-Lambert law (Eq. 3.4):

$$\frac{I}{I_0} = \exp(-\alpha(\lambda)t) \tag{3.4}$$

where I is the intensity of light transmitted through a sample of thickness, t, with an initial intensity of I_0, and $\alpha(\lambda)$ is the wavelength dependent absorption coefficient (Fig. 3.5.a). The probability of absorption of a photon is therefore can be written as Eq. 3.5.

$$\eta_A = 1 - \exp(-\alpha(\lambda)t) \tag{3.5}$$

The only experimental parameter required to predict the absorption probability is the wavelength dependent absorption coefficient. This can be obtained by measuring the wavelength dependent reflection and transmission in a known optical path length:

$$\alpha(\lambda) = -\frac{ln\left(\frac{T}{1-R}\right)}{t} \tag{3.6}$$

An example of the absorption probability for two different values of α as a function of photon propagation distance is shown in Fig. 3.5.b.

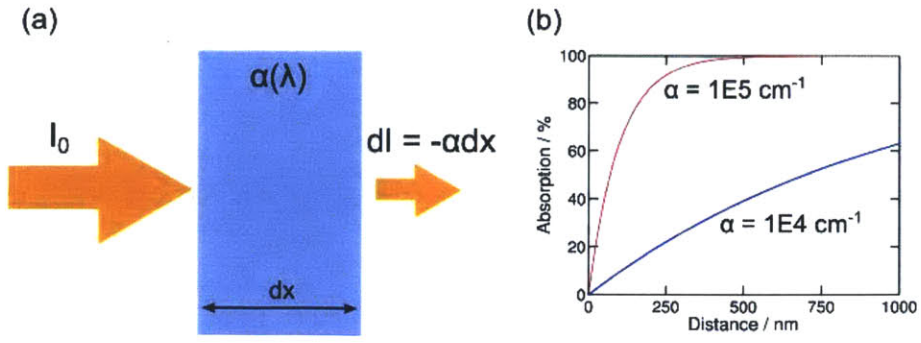

Fig. 3.5 (a) Schematic of Beer-Lambert law. The relevant experimental parameter that determines absorption probability is the wavelength dependent absorption coefficient. (b) Absorption probability as a function of photon distance determined by Beer-Lambert law for two different absorption coefficients.

3.2.3 Isotropic and Anisotropic Photoluminescence

In this model, the solution to the wave equation of a photon is approximated as a point source with position, x, y, z, wavelength, λ, and Poynting vector, θ_k, φ_k. The probability of emitting a photon after an absorption event is determined based on the photoluminescence quantum yield (PLQY). The PLQY of the luminescent chromophore can be experimentally measured with reasonable accuracy by measuring the photons emitted with an integrating sphere and dividing by the absorption at the excitation wavelength. A sample with low optical density should be used to minimize self-absorption for an accurate value of PLQY and spectrum.

Once a photon is emitted the Poynting vector (θ_k, φ_k) as defined in Fig. 3.6 and wavelength λ must be determined. The probability of emitting at some wavelength is determined by the photoluminescence spectrum. The photoluminescence spectrum can be measured with an excitation source, such as a laser, and a calibrated monochromater. A sample with low optical density should be used and photoluminescence collected at normal incidence to minimize self-absorption for an accurate photoluminescence spectrum. The probability of emitting at some θ_k, φ_k depends on whether the chromophore is an isotropic or anisotropic emitter, Fig. 3.7.a. An isotropic emitter has Poynting distribution, $\langle S \rangle \propto constant$, whereas the ideal dipole emitter has, $\langle S \rangle \propto sin(\theta)^2$, for a dipole with $\theta_D = 0°$. For non-zero (θ_D, φ_D) (Fig. 3.6), (θ_k, φ_k) would be rotated by (θ_D, φ_D) for the correct angular probabilities.

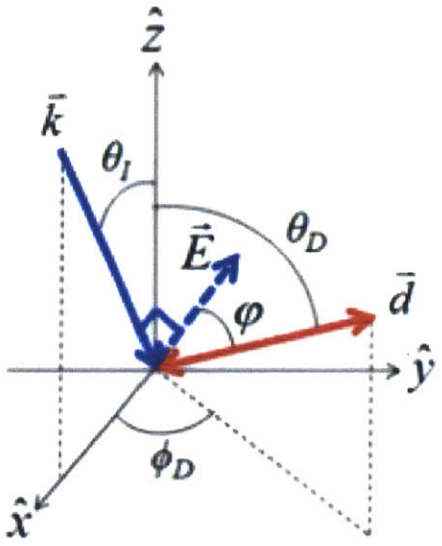

Fig. 3.6 Spherical coordinate system for photon k-vector and dipole absorber/emitter in the Monte Carlo ray tracing model.

In determining the angular probabilities for arbitrary aligned dipoles, we were also able to show the theoretical trapping efficiency for anisotropic emitters for LSCs [38]. By integrating an arbitrary orientation of a Hertzian dipole power density over the solid angle θ_C to π- θ_C, where θ_C is the critical angle:

$$\theta_C = co^{S-1}\left(\sqrt{1-\frac{1}{n_S{}^2}}\right) \tag{3.7}$$

By normalizing the integral by the total power emitted by the dipole, this yields the theoretical trapping efficiency for an anisotropic emitter with arbitrary orientation θ_D.

$$\eta_T(\theta_D) = \sqrt{1-\frac{1}{n_S{}^2}}\left(1+\frac{1}{n_S{}^2}\left[1-\frac{3}{2}si^{n_2}\theta_D\right]\right) \tag{3.8}$$

The trapping efficiency as a function of emitter angle is plotted in Fig. 3.7.b for three different refractive indices. Mulder et al. [38] have proposed and demonstrated aligned emitters as an additional engineering tool to address self-absorption. As photoluminescence and trapping efficiencies approach unity, the effect of self-absorption diminishes. A comparison of trapping

efficiency as a function of waveguide refractive index of isotropic and anisotropic emitters is shown in Fig. 3.7.c.

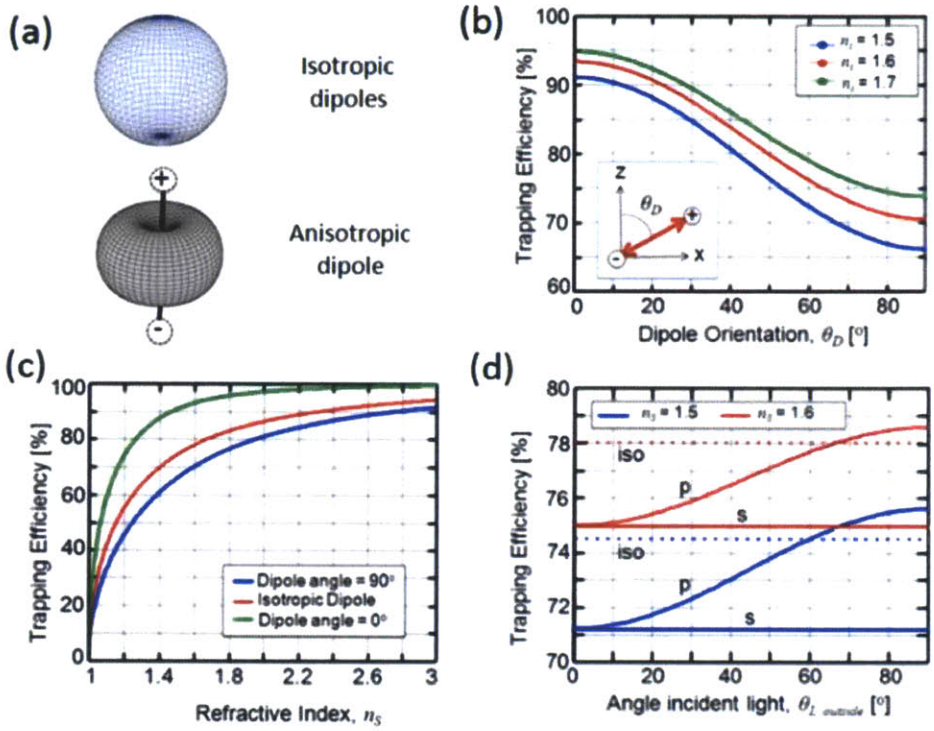

Fig. 3.7 (a) Power distributions for an isotropic and anisotropic emitter (dipole). Less power is present within the loss cone of an anisotropic emitter. (b) Theoretical trapping efficiency as a function of dipole angle for three different waveguide refractive indices. (c) Theoretical trapping efficiency as a function of waveguide refractive index for dipole orientation of θ_D = 0°, 90° and isotropic. (d) Theoretical trapping efficiency for dichroic chromophores dispersed uniformly as a function of incident light angle (solid line). Theoretical trapping efficiency of an isotropic emitter (dashed line) for reference.

3.2.4 Reflection Probability

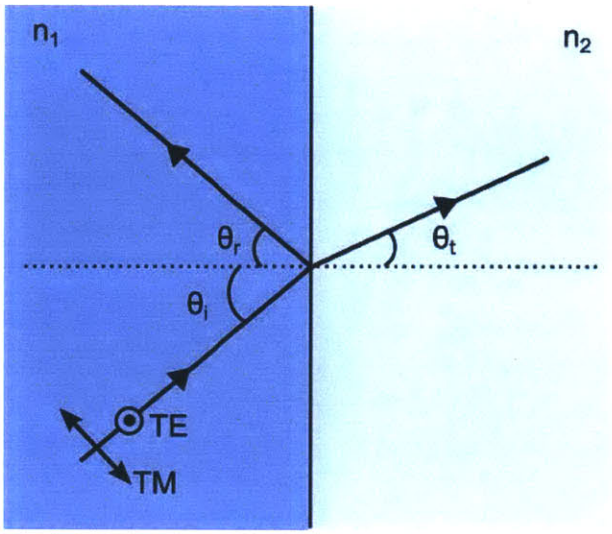

Fig. 3.8 Schematic of reflection and refraction at an interface. The relevant experimental parameters that define reflection probability is the wavelength dependent refractive index.

When a photon is incident at an interface between two materials with different refractive indices, a portion of the photon's energy is transmitted, or refracted, and the rest is reflected based on the boundary conditions as shown in Fig. 3.8. In the Monte Carlo ray tracing model, we treat this physical process as a probability defined by the Fresnel equations:

$$R_S = \frac{n_1 \cos^S(\theta_1) - n_2 \cos^S(\theta_2)}{n_1 \cos^S(\theta_1) + n_2 \cos^S(\theta_2)} \tag{3.9}$$

$$R_P = \frac{n_1 \sec^C(\theta_1) - n_2 \cos^S(\theta_2)}{n_1 \sec^C(\theta_1) + n_2 \cos^S(\theta_2)} \tag{3.10}$$

where R_S and R_P are the reflection coefficients for s- and p-polarized light respectively, n_1 and n_2 are the wavelength dependent refractive indices, and θ_1 and θ_2 are the incident and transmitted angles relative to the boundary's plane. The overall reflection probability is the weighted average of the s- and p-polarization reflection coefficients:

$$R = P_S R_S + P_P R_P \tag{3.11}$$

where P_S and P_P are the percentage of the photon's polarization in the s- and p-polarized plane, and R is the overall reflection coefficient. The relevant experimental parameters that determine the reflection probability are the wavelength dependent refractive indices. These can be determined experimentally by measuring the wavelength dependent reflection and transmission. Shown in Fig. 3.9 are examples of the reflection probabilities at an interface.

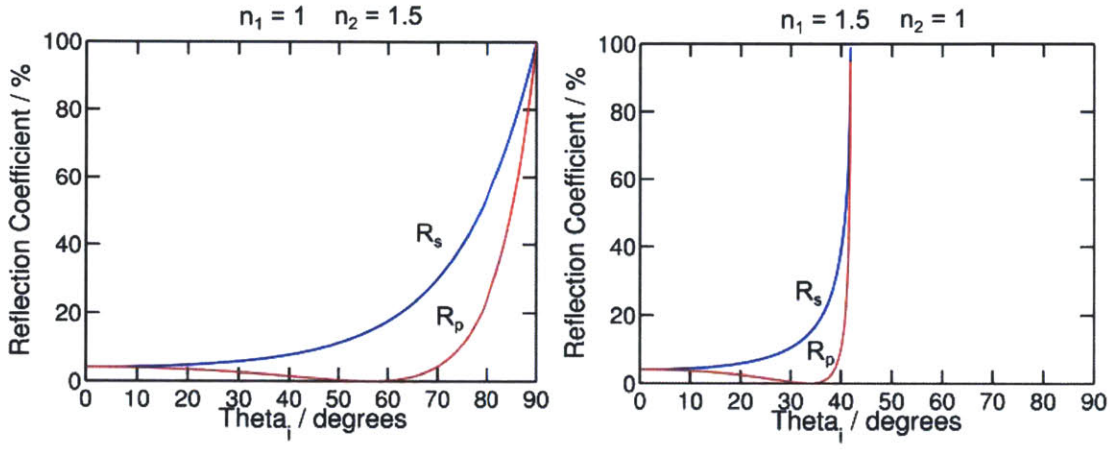

Fig. 3.9 Reflection probability versus incident angle for s- (blue) and p-polarized (red) light (a) for light in a material with refractive index of 1 incident on a material with index of refraction 1.5 and (b) for light in a material with refractive index of 1.5 incident on a material with index of refraction 1. Photons going from high to low index with incident angles greater than the critical angle have reflection probabilities of 1, due to trapping by total internal reflection.

3.3 Theoretical and Experimental Comparison

The Monte Carlo ray tracing model source code, example material input files, and LSC definition file can be found in Appendix A. The Monte Carlo ray tracing model was originally written in a MATLAB script, but was determined to be too slow. The MATLAB script was ported to C++, which significantly reduced run time of the simulation. The LSC optical properties are defined by layer files, such as air, glass waveguide, and luminescent chromophore, with wavelength dependent absorption coefficient, photoluminescence, refractive index, and photoluminescence quantum yield. The LSC definition file defines the geometry, the layer thicknesses, the order of the layers, the isotropic or anisotropic nature of the absorber/emitter, the input photon wavelength, the incident angle, and the number of photons to sample. More details can be found within the comments of the source code in Appendix A.

The first system studied with the Monte Carlo ray tracing model was a solution processed based LSC that makes use of the well-known BASF Lumogen chromophores [32]. The chromophores Lumogen Violet, Yellow, and Red are doped into poly(methyl methacrylate) (PMMA) at weight concentrations of 20:20:1% and 1:1:1% respectively. Lumogen Violet and Yellow are the solar absorbers and FRET to Lumogen Red, which is primarily the emitter. The difference in concentration of the final emitter of the two systems allows us to observe the behavior of high and low self-absorption in LSCs. Fig. 3.10.a and b are spectral plots of the input absorption coefficients and photoluminescence of the two systems. The measured PLQY of Lumogen Red is 90%. The refractive index of PMMA and SF10 (high index glass) was assumed to be 1.5 and 1.7 respectively and constant versus wavelength. The thicknesses were 18 μm and 2.8 μm for 1:1:1% and 20:20:1% to ensure absorption at excitation wavelength of 405 nm was matched and glass waveguide thickness of 1 mm.

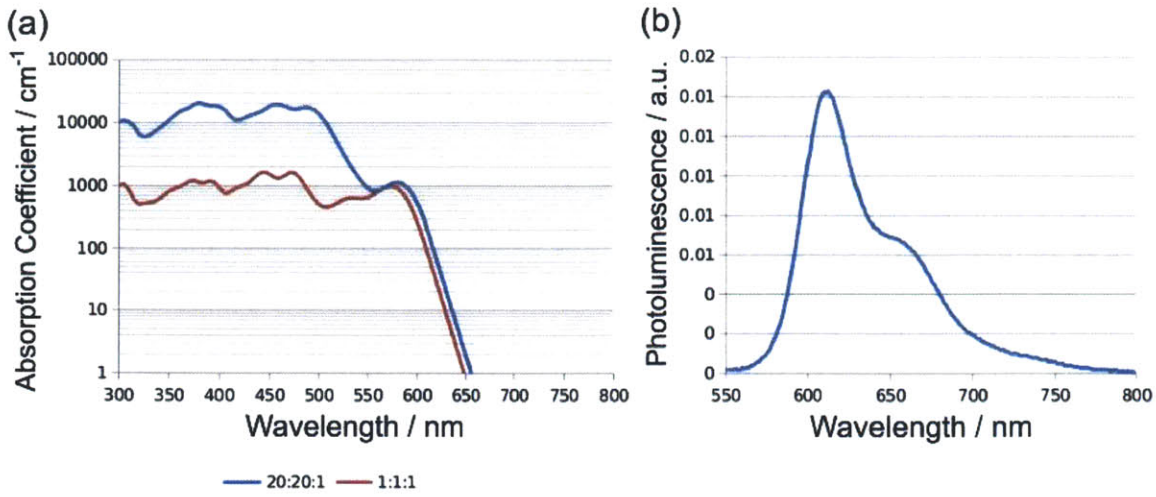

Fig. 3.10 Experimental (a) absorption coefficient of 20:20:1% (blue) and 1:1:1% (red) wt. Lumogen Violet:Yellow:Red in PMMA (b) and photoluminescence of Lumogen Red used in the Monte Carlo ray tracing model.

As can be seen in Fig. 3.11.a and b, the simulated spectrum that is incident at the edges of the LSC for G = 10, 20, and 30 is highly modified from the spectrum in Fig. 3.10.b. For the LSC with lower relative self-absorption (20:20:1), it is seen as the geometric gain (or average optical pathlength) increases the main peak of Lumogen Red (610 nm) becomes attenuated whereas the lower energy peak (650 nm) increases with G. This high energy peak decrease and low energy peak increase is due to photon recycling. The higher self-absorption (1:1:1) resembles a single Gaussian peak at all G, but also shows a slight red-shift with increasing G. The model generated single peak for 1:1:1% is in good agreement with experimental PL measurements. This spectral red-shift with decreased Stokes shift (20:20:1 versus 1:1:1) and increasing G (10 versus 20 versus 30) demonstrates the problem of self-absorption. This behavior indicates that, due to self-absorption, we should see a rapid decrease in efficiency with increasing G as the initial spectrum redshifts, but the rate of decrease should slow with increased spectral red-shifting or increasing

Stokes shift. This roll-off in efficiency with increased G is modeled and shown in Fig. 3.12 where 1:1:1 rapidly drops to 50% at low geometric gains (G < 5) and then falls off at a similar rate to the low self-absorption sample, 20:20:1, albeit at a lower efficiency.

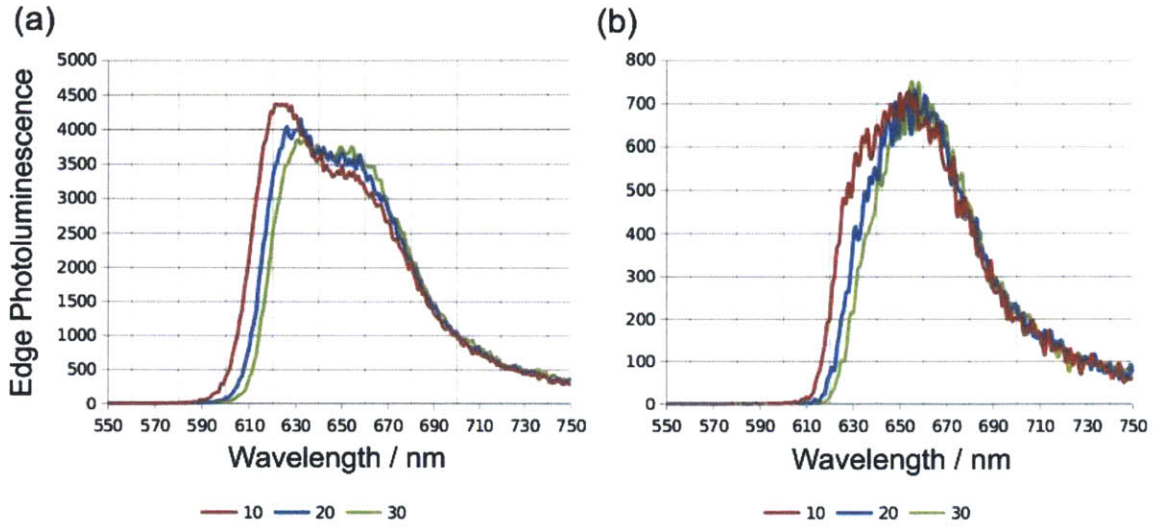

Fig. 3.11 Monte Carlo ray tracing generated spectrum of photoluminescence incident at the edges of LSCs at various G (a) for 20:20:1% (b) and 1:1:1% wt. Lumogen Violet:Yellow:Red in PMMA on glass.

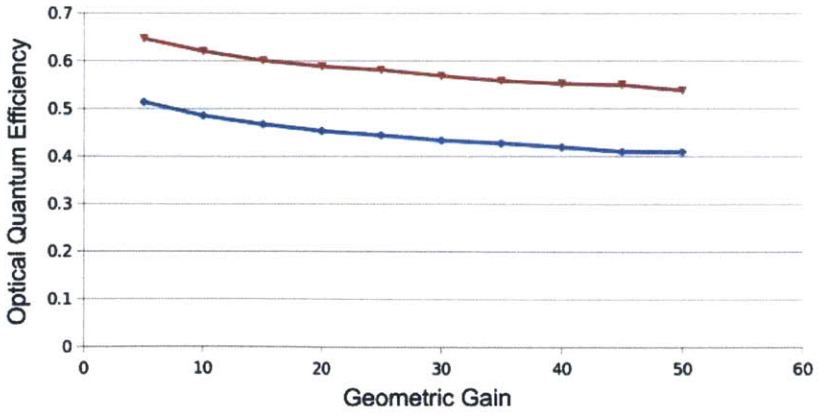

Fig. 3.12 Modelled LSC efficiency as a function of geometric gain for 20:20:1% (red) and 1:1:1% (blue) wt. Lumogen Violet:Yellow:Red in PMMA on glass.

The next system the Monte Carlo ray tracing model was applied to was oriented luminescent chromophores on glass for increased trapping efficiency in LSCs. The dichroic molecule used was a fluorescent molecule, Coumarin 6 (C6). Two different types of LSCs were investigated: an isotropic distribution of C6 in PMMA and vertically, $\theta_D = 0°$, aligned C6 in a liquid crystal host, UCL018. For more information on the experimental characterization, please see Mulder et al [38]. The relevant material inputs to the model were experimentally determined wavelength dependent absorption coefficients and photoluminescence, which are shown in Fig. 3.13.a and b. The refractive index of PMMA and UCL018 were assumed to be 1.5 and 1.6 respectively with SF10 (waveguide) having refractive index of 1.7. The PLQY of C6 at a 1% wt. loading was measured to be 78% with a coupling efficiency of 85% to the solar cell. The thicknesses in the model were adjusted to result in absorption of 42% in both PMMA and UCL018. The glass waveguide thickness was 1 mm.

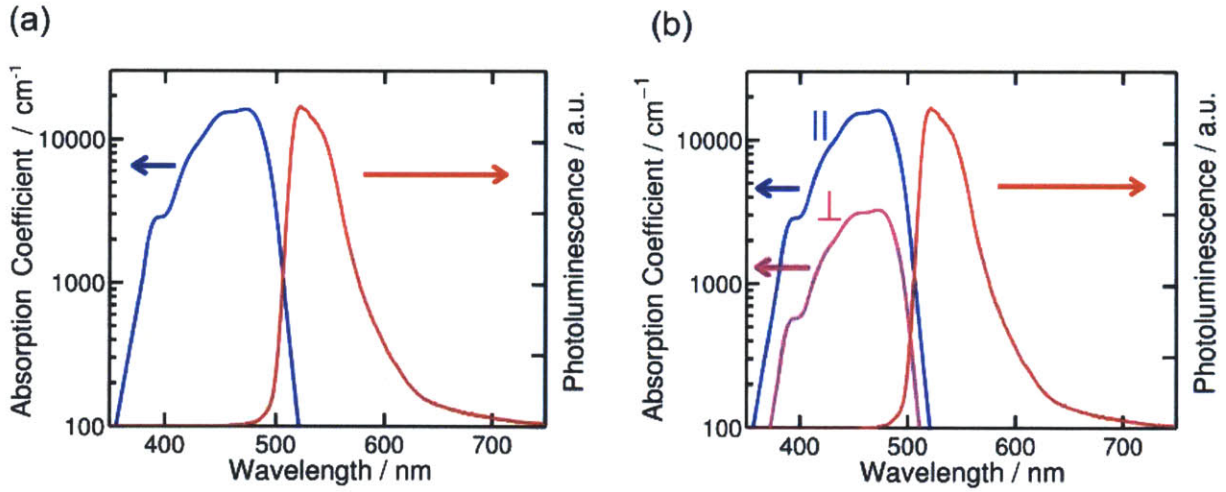

Fig. 3.13 Experimental absorption coefficient (blue/magenta) and photoluminescence (red) versus wavelength of (a) 1% wt. Coumarin 6 in PMMA (isotropic) (b) and 1% wt. Coumarin 6 in UCL018 (anisotropic) used in Monte Carlo ray tracing model.

The measured and modelled external quantum efficiency (EQE), electrons out per incident photon, as a function of geometric gain for an isotropic distribution and vertically aligned C6 molecules can be seen in Fig. 3.14. The geometric gain dependence was simulated in two different manners. The first method was the actual definition of geometric gain, where the area of the LSC is changed with uniform surface illumination (open circles). The second method was imitating the experimental method of geometric gain dependence [5] by the spot excitation technique (open squares). The modelled behavior matches very well with the experimental isotropic distribution of C6 molecules (green). The modelled G dependence of EQE of the vertically aligned C6 molecules do trend higher than the isotropic C6 due to higher trapping efficiency, as does the experimental data, but are not as good of a match as the isotropic case. This is more than likely due to the assumption of a pure dipole emitter whereas the actual power distribution of photoluminescence is more complicated function of space. With more accurate experimental data inputs, the model should converge to the experimental data.

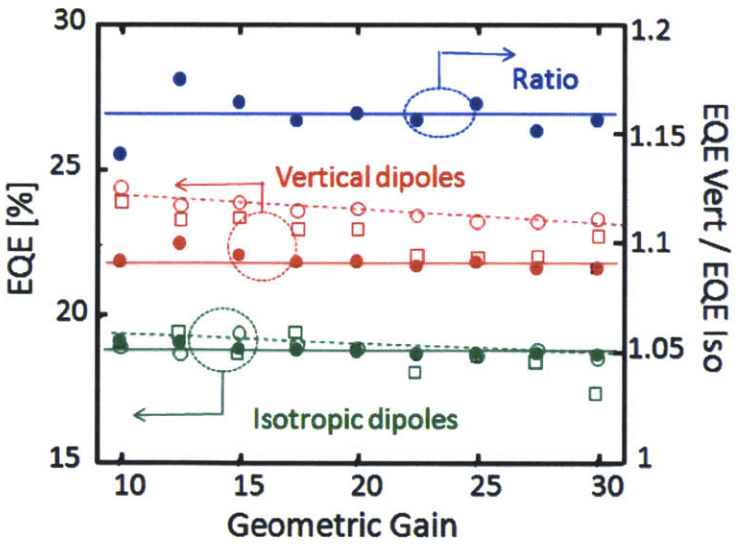

Fig. 3.14 (left axis) Measured (closed) and modelled (open) external quantum efficiency as a function of geometric gain for vertically aligned (red) and isotropic distribution (green) of C6 molecules [38].

3.4 Conclusion

In summary, we have developed a Monte Carlo ray tracing model for luminescent solar concentrators. In this model we include all the major processes occurring within an LSC such as photon absorption, photoluminescence, and reflection/refraction. Included in this model are chromophores with anisotropic absorption and emission at arbitrarily defined orientations as well as the traditional isotropic absorber and emitters. These processes are treated as binary processes determined probabilistically based on the relevant physical equations and experimental parameters describing energy flow. By repeated sampling, this probabilistic behavior converges to the actual energy movement and behavior in a luminescent solar concentrator. This tool has been used to reproduce experimental LSC results, demonstrating the productiveness of a Monte Carlo ray tracing model for next generation luminescent solar concentrators.

Chapter 4

Cascade Energy Transfer for Neodymium Based Infrared Luminescent Solar Concentrators

Separating solar absorption from optical emission

4.1 Infrared LSC Motivation

The luminescent solar concentrator (LSC) can address the high costs faced by geometric concentrators and potentially exceed them in performance [29]. State of the art LSC emitters operate in the visible or near infrared [5, 29-32], necessitating high energy solar cells such as GaAs or GaInP. These solar cells, when commercially available, are costly and use precious materials [39]. A more attractive option are the class of low cost, high efficiency, and earth abundant silicon solar cells, however current silicon-matched LSC systems are suboptimal. Here, we present the use of a lanthanide ion--colloidal nanocrystal energy cascade system as a promising LSC emitter scheme for the silicon spectral region. First, the strengths and weaknesses of two possible emitters, lanthanide ion and colloidal nanocrystal when individually employed for infrared LSCs are discussed followed by a discussion how they can be combined to overcome their respective weaknesses.

4.1.1 Optical Properties of Neodymium

Neodymium, a member of rare earth elements, is an important infrared emitting material used in some of the most efficient lasers and optical amplifiers today [40]. Fortunately, neodymium's classification of a rare earth metal is a misnomer, as its abundance is roughly half that of important industrial metals such as copper and nickel [41] (Fig. 4.1). Consequently, many rare earth elements find extensive employment in important technologies such as lasers [40], phosphors for lighting [42], and magnets for hard drives and automobiles [43].

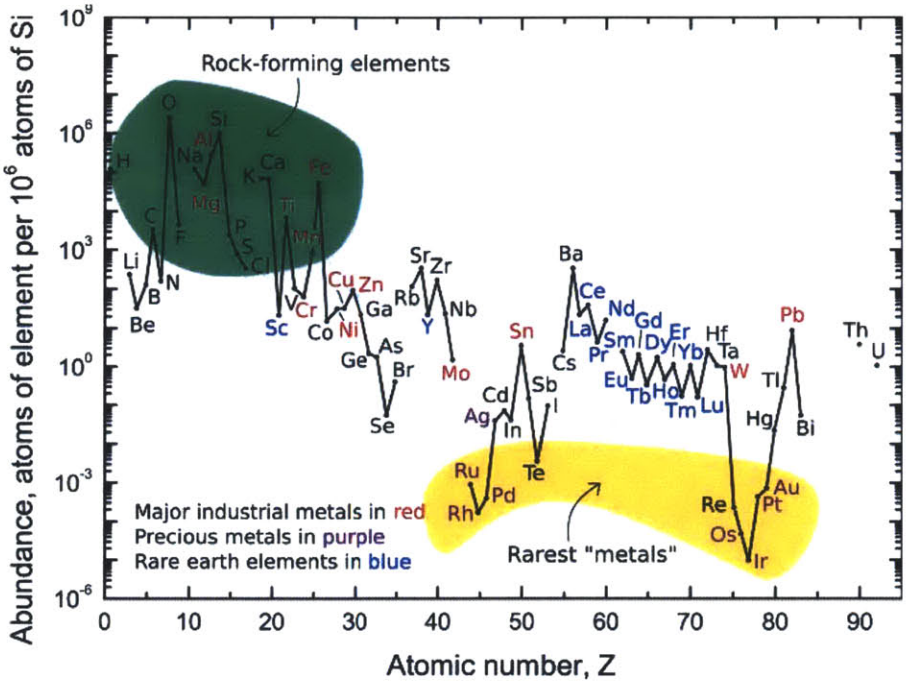

Fig. 4.1 Abundance (atom fraction) of the chemical elements in Earth's upper continental crust as a function of atomic number [41]. Rare earth elements are in blue.

In addition to its earth abundance, neodymium is an attractive emitter for luminescent solar concentrators for similar reasons that make it an important laser material. The high photoluminescence quantum yield and low self-absorption are essential for an efficient laser and also an LSC. Neodymium's low self-absorption is a result of the large Stokes shift between its absorption and main emission peak at 1.06 μm, shown in Fig. 4.2.a for Nd^{3+}:glass. This photoluminescence peak is well suited for high efficiency silicon solar cells with EQE cutoff of 1.1 μm. In a glass host at low concentrations (< 1%), neodymium has photoluminescence quantum yields of greater than 90% [44]. Of the four possible primary transitions (Fig. 4.2.b.), 90% of the emitted light is derived from transitions which are suitable to be harvested by silicon (0.88 um and 1.06 um), resulting in an effective photoluminescence quantum yield for a silicon solar cell would be approximately 80% [44].

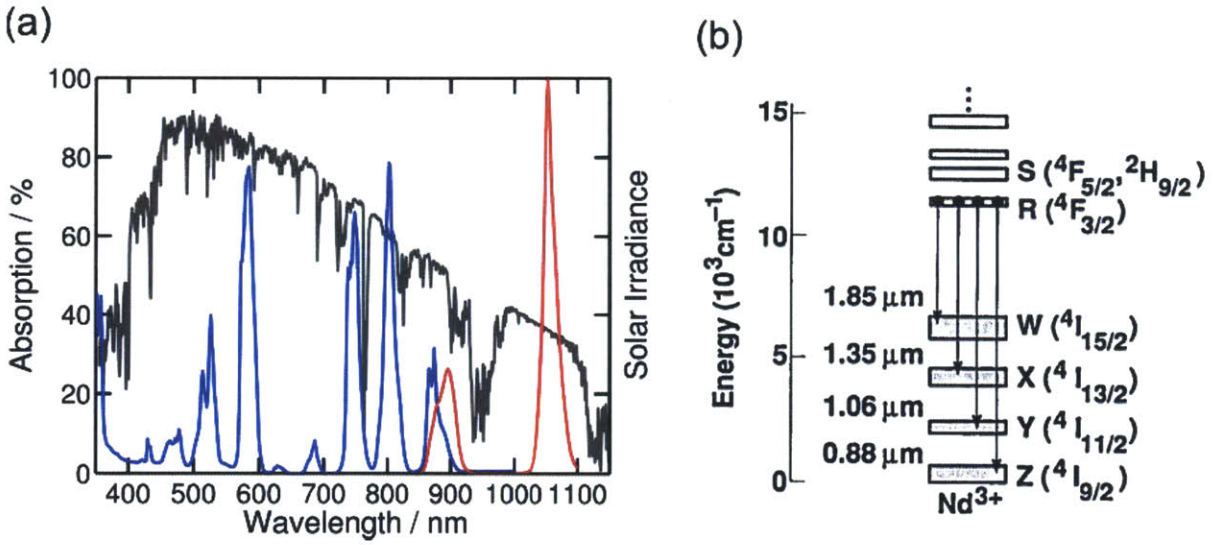

Fig. 4.2 (a) Absorption (blue) and photoluminescence (red) of APG-1 1% wt. Nd_2O_3 glass. The poor overlap between sunlight (gray) and Nd^{3+}:glass can be seen. (b) The radiative transitions of neodymium doped glasses. Approximately 90% of the photoexcited electrons recombine through the 880 and 1060 nm transitions.

While the neodymium ion's large stokes shift, high PLQY, and good spectral alignment make it an attractive candidate for silicon-matched LSCs, its discrete absorption lines (Fig 4.2.a) and low absorption coefficient (the peak absorption coefficients of neodymium are less than < 5 cm^{-1} for moderately doped glass (< 1%)) pose a problem for broad wavelength excitation. Consequently, in industrial processes, very thick slabs are required to achieve sufficient absorption from for broad excitation optical applications. For example, in the continuous glass melt process for neodymium doped phosphate glass developed by the National Ignition Facility along with glass manufacturers Schott and Hoya shown in Fig. 4.3.a, slabs of >3 cm are produced for application with flashlamps. Although ideal for monochromatic excitation from LEDs or lasers, the lack of broad and high absorption coefficients limits neodymium usefulness as a luminescent chromophore for a silicon-matched LSC.

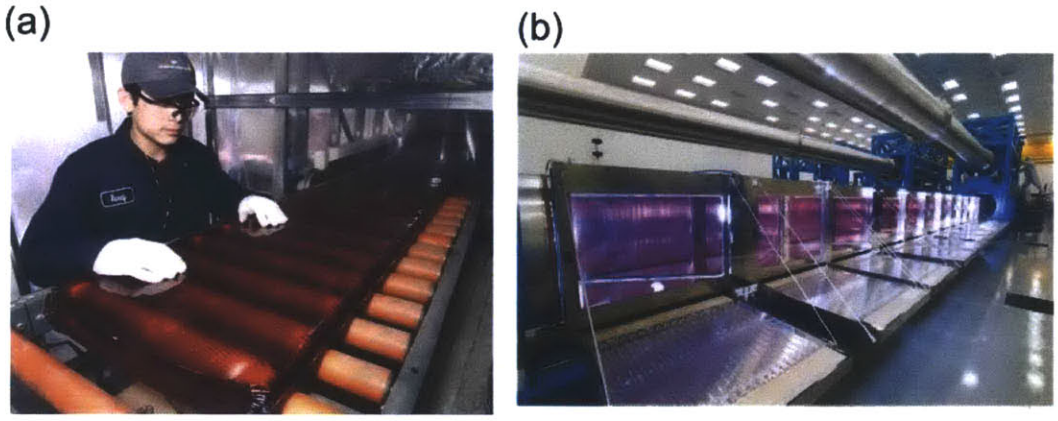

Fig. 4.3 Photo of thick slab neodymium doped phosphate glass (a) from continuous glass melt manufacturing [40] (b) and used as optical amplifiers at the National Ignition Facility [40].

4.1.2 Optical Properties of Colloidal Nanocrystal

Colloidal semiconductor nanocrystals, also known as quantum dots, are an important emerging material system used in technologies such as phosphors [45], LEDs [46], and thin film solar cells [47]. A quantum dot is an inorganic crystalline semiconductor that has spatial size on the order of 1-10 nm. An exciting aspect of this material system is their size tunable optical properties, which result from confinement effects. Analogous to the quantum mechanical particle-in-a-box problem, the electron-hole spatial confinement allows for tuning of nanocrystal energy levels. The size dependent absorption and photoluminescence for CdSeTe [48] and CdSe [49] can be seen in Fig. 4.4.a and b respectively. The confinement also enhances radiative recombination, leading to bright photoluminescence emission approaching unity, which makes them promising candidates for emitters in LSCs. Due to their large and broad absorption coefficients, quantum dots are efficient absorbers in thin films or as dopants in bulk waveguides. However, quantum dots suffer from a small Stokes shift (Fig. 4.4.a) which results in significant self-absorption and transport losses detrimental to LSC performance.

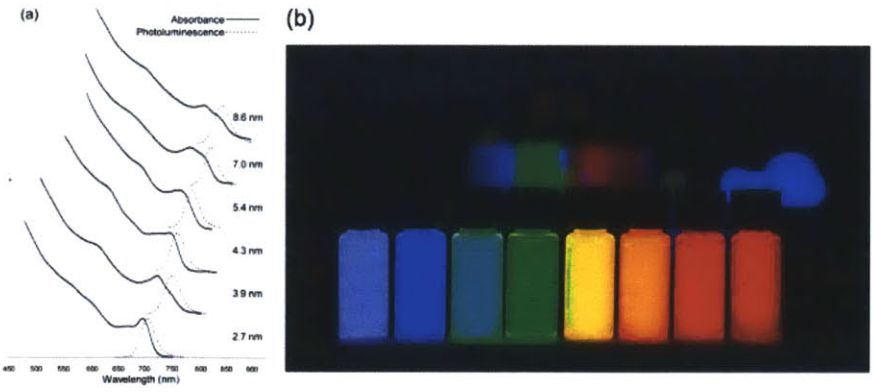

Fig. 4.4 (a) Absorption (solid) and photoluminescence (dotted) of CdSeTe quantum dots from 2.7-8.6 nm [48]. (b) Photo of visible emitting quantum dots under UV light. The tunability of photoluminescence is a result of nanocrystal size and composition [49].

4.2 Cascade Energy Transfer for LSCs

We have discussed Nd^{3+}, a material with a large stokes shift but discrete absorption, and QDs, which have broad absorption but a small stoke shift. Individually, these materials would make poor emitters for LSCs, however by combining these materials into a cascade energy transfer system, we can selectively utilize their attributes and overcome their weaknesses to achieve a broadly absorbing LSC with a large stokes shift.

4.2.1 Cascade Energy Transfer

An attractive infrared LSC for silicon would be to use a nanocrystal's efficient solar absorption as the energy donor to the emitting acceptor of neodymium for its efficient emission and low self-absorption. Unfortunately non-radiative energy transfer schemes such as FRET currently are not available due to the difficulty of integrating the neodymium ion into the nanocrystal. Alternatively, nanocrystal donors and neodymium acceptors can be coupled through cascade energy transfer (radiative energy transfer) due to their complementary optical properties (Fig. 4.5.a). The scheme of cascade energy transfer is depicted in Fig. 4.5.b. The nanocrystal donor, 3% wt CdSe/CdZnS doped in poly(vinyl butyral-co-vinyl alcohol-co-vinyl acetate) (PVB-CVA-CVAc), is an efficient absorber of sunlight as a result of its broad and high ($> 10^5$ cm^{-1}) absorption coefficients, as shown in Fig. 4.5.a. Due to the nanocrystal's narrow and efficient photoluminescence emission, it can be tuned to have near complete overlap with an absorption peak of the neodymium acceptor doped in a phosphate glass (APG-1), for efficient cascade energy transfer.

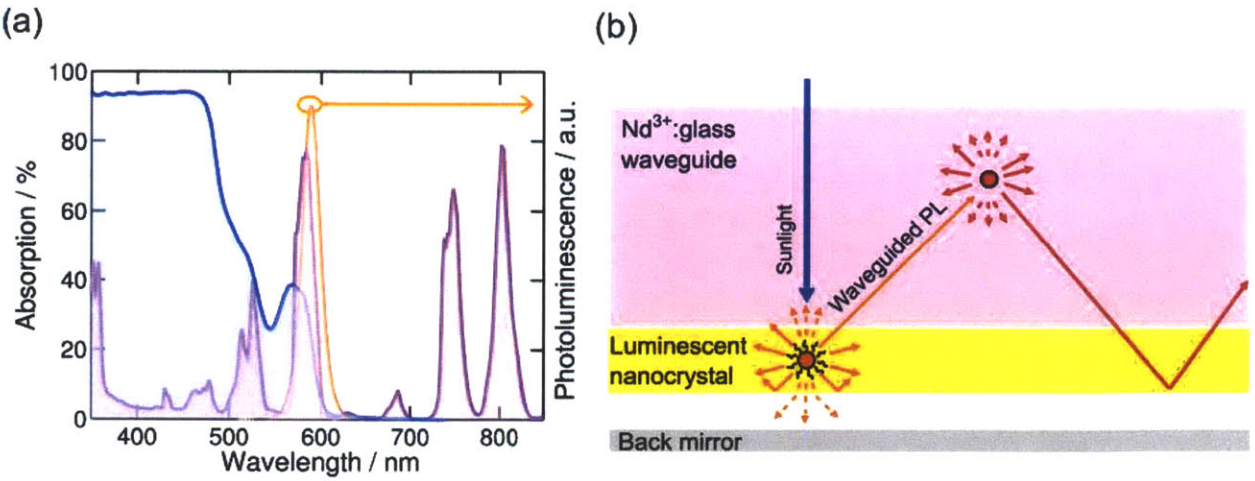

Fig. 4.5 (a) Absorption of APG-1 (phosphate glass) doped with 1% wt. Nd_2O_3 (magenta) and 10% wt. CdSe/ZnS quantum dots in PVB-CVA-CVAc (blue). The nanocrystal photoluminescence (orange) is tuned to the 580 nm Nd^{3+} peak for efficient cascade energy transfer. (b) Schematic of cascade energy transfer. Luminescent nanocrystal efficiently absorbs sunlight and is re-emitted as photoluminescence. By tuning the nanocrystal's narrow photoluminescence to a Nd^{3+} absorption peak, the waveguided photoluminescence will transfer to Nd^{3+}.

The efficiency of cascade energy transfer is very similar in form to the efficiency of a luminescent solar concentrator. Cascade energy transfer consists of photon absorption (η_A), photoluminescence emission (η_{PL}), and waveguided photoluminescence absorption (η_{WA}):

$$\eta_{CE}{}^{T} = \eta_A \eta_{PL} \eta_{WA} \tag{4.1}$$

The efficiency of waveguided photoluminescence absorption is composed of a number of processes within the LSC. It embodies the trapping efficiency of photoluminescence of the nanocrystal, the overlap spectrum of the absorption of the waveguide with the photoluminescence, and self-absorption of the waveguided photoluminescence. With a back

mirror, as shown in Fig. 4.5.b, the efficiency of cascade energy transfer can be 100% if the single pass absorption of the waveguide at the nanocrystal's emission wavelength is close to 100%. For good cascade energy transfer, we want to maximize the following ratio:

$$\left.\frac{(\alpha Ct)_{Nd^{3+}}}{(\alpha Ct)_{QD}}\right|_{QDPL} \tag{4.2}$$

Where α is the absorption coefficient, C is the concentration, and t is the layer thickness. Efficient cascade energy transfer can be obtained by maximizing the waveguides absorption at the nanocrystal's emission wavelength and minimizing the nanocrystal's self-absorption.

4.2.2 Optical Quantum Efficiency

To characterize the spectral efficiency of an LSC, also known as the optical quantum efficiency, we make use of an integrating sphere setup (Fig. 4.6) to count photons. A tungsten light source is passed through a monochromater to produce monochromatic light. The monochromatic light is passed through an optical chopper wheel to convert the DC light source into an AC light source. The integrating sphere has four ports for input, reflected, transmitted, and output light signal. The input light is incident on the sample producing photoluminescence collected with a spectrally calibrated photodetector. The output light passes through a high pass wavelength filter to ensure only the neodymium acceptor's emission is collected. The photocurrent is finally measured with a sensitive lock-in amplifier.

The optical quantum efficiency of an LSC is defined as the photoluminescence emitted from the edges of the waveguide [38]. For this reason we must be able to discriminate between facial and edge photoluminescence from the LSC. This is done by painting the edges of the LSC

with light absorbing paint (carbon black). The output photoluminescence from this painted sample is a result of only facial emission. By measuring a second identical sample with clear edges, the measured output photoluminescence is a result of both facial and edge emission. The difference between these measurements is the optical quantum efficiency.

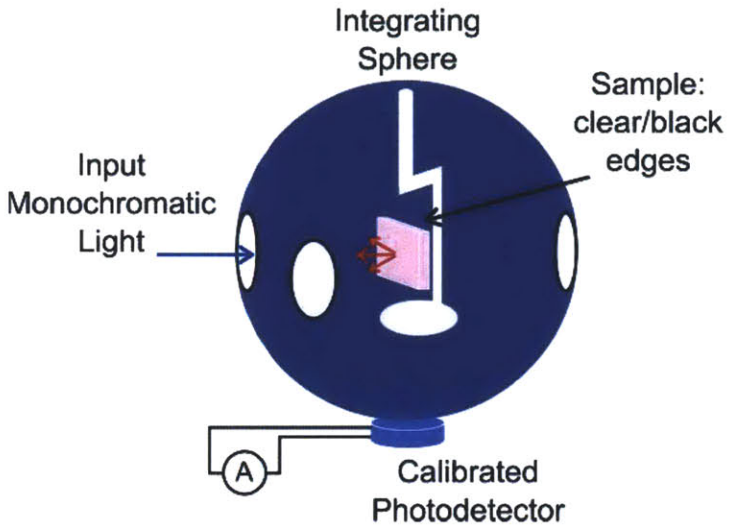

Fig. 4.6 Optical quantum efficiency measurement experimental setup for LSCs. Monochromatic light enters an integrating sphere. The light incident on the sample produces photoluminescence collected with a spectrally calibrated photodetector while the reflected and transmitted light exit the sphere.

The neodymium LSCs were purchased from Schott glass. Neodymium oxide was doped into a phosphate glass matrix [44] at 1, 2, and 3% wt loading. The Nd^{3+}:glass was stored in air and no degradation was observed. The nanocrystal coating was produced through the dropcasting process. CdSe/CdZnS nanocrystals were provided by QD Vision, Inc. Prior to use, the nanocrystals were precipitated once with isopropyl alcohol and then dissolved in chloroform. The PVB-CVA-CVAc polymer was purchased from Sigma Aldrich and dissolved in chloroform at a concentration of 100 mg/mL.

As shown in Eq. 4.2, in order to have good cascade energy transfer we must maximize the numerator in the nanocrystal's photoluminescence spectrum of ~ 580 nm. We have no control over neodymium's inherent absorption coefficient (α) at 580 nm, but we do have control over the thickness of the doped waveguide (Fig. 4.7.a) and the neodymium doping concentration within the waveguide (Fig. 4.7.c). The optical quantum efficiency as a function of wavelength of a 25 x 25 x (1 and 5) mm APG-1 with 1% wt. Nd_2O_3 doping is shown in Fig. 4.7.b. By increasing the thickness of the Nd^{3+}:glass waveguide from 1 to 5 mm, the OQE increased from 10% to 37%. As can be seen, although an efficient emitter, the OQE of Nd^{3+} based LSCs suffer from low and spectrally narrow absorption coefficients. This can partially be overcome by increasing the concentration of neodymium dopant within the glass matrix. The optical quantum efficiency as a function of wavelength of a 25 x 25 x 5 mm APG-1 with 1, 2, and 3% wt. Nd_2O_3 doping is shown in Fig. 4.7.d. In the spectral regions where absorption is not saturated such as at 850 nm, the OQE of the 1% and the 2% wt. Nd_2O_3 doping increases from 12% to 21% respectively. The OQE increase from 2% to 3% wt. Nd_2O_3 doping is marginal due to self-quenching effects. The increase in absorption is offset by a decrease in photoluminescence quantum yield. The self-quenching effects must be balanced with increased cascade energy transfer efficiency.

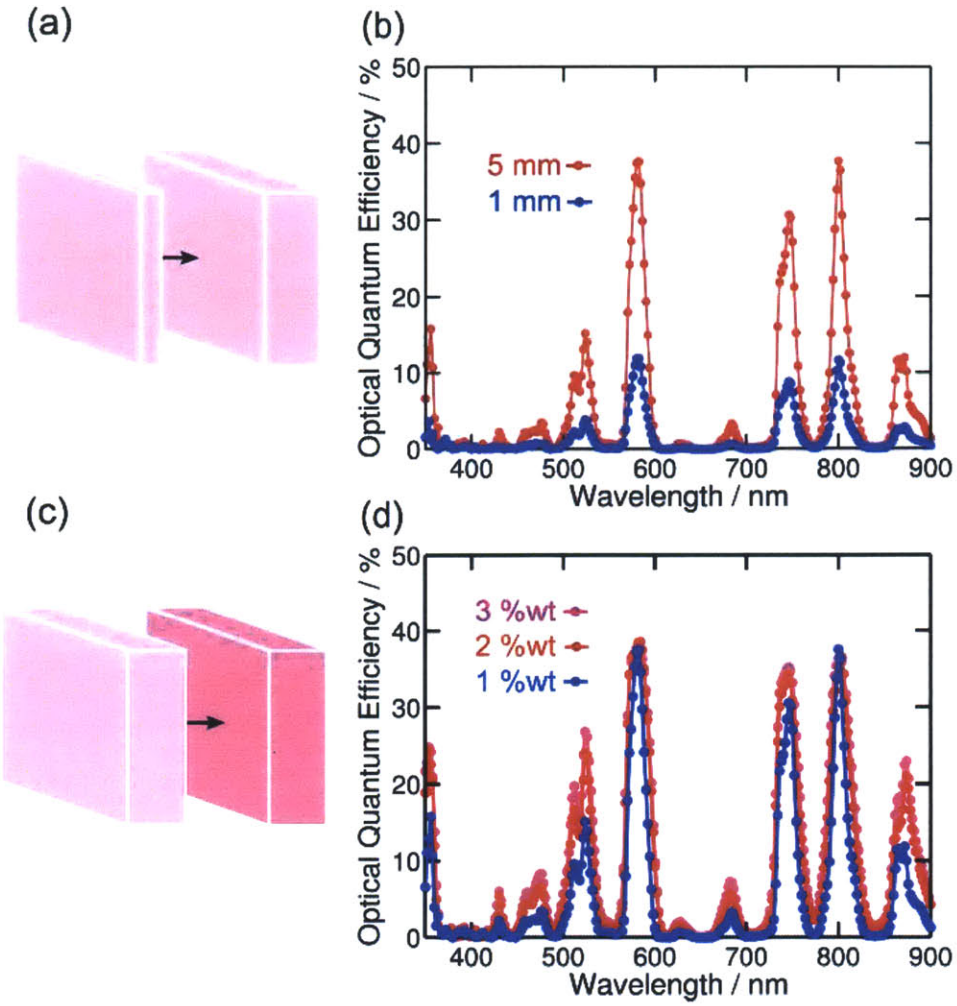

Fig. 4.7 (a) Increasing waveguide thickness to increase waveguide absorption. (b) Optical quantum efficiency as a function of wavelength for 25 X 25 X 1 mm (blue) and 25 X 25 X 5 mm (red) APG-1 1% wt. Nd_2O_3 doping. (c) Increasing neodymium doping concentration within waveguide to increase waveguide absorption. (d) Optical quantum efficiency as a function of wavelength for 25 X 25 X 5 mm APG-1 1% (blue), 2% (red), and 3% (magenta) wt. Nd_2O_3 doping.

The main limiting factor on the peak OQE of Nd^{3+}:glass is the low absorption. The 1% Nd^{3+}:glass, for an infrared emitter, has high photoluminescence efficiency of 70% and low transport losses. A simple and low cost technology to increase the absorption efficiency of Nd^{3+}:glass is a back mirror as shown in Fig. 4.8.a. The back mirror can be a specular reflector

such as an aluminum or silver mirror or a diffusive reflector such as TiO_2 or $BaSO_4$ powders. The optical quantum efficiency as a function of wavelength of a 25 x 25 x 5 mm APG-1 with 1% wt. Nd_2O_3 doping without (blue) and with (red) a back mirror is shown in Fig. 4.8.b. With a simple back mirror, the peak OQE of an Nd^{3+}:glass LSC increases from 37% to 43%. This result demonstrates the potential of neodymium emitters for infrared LSCs to be paired with high efficiency silicon solar cells.

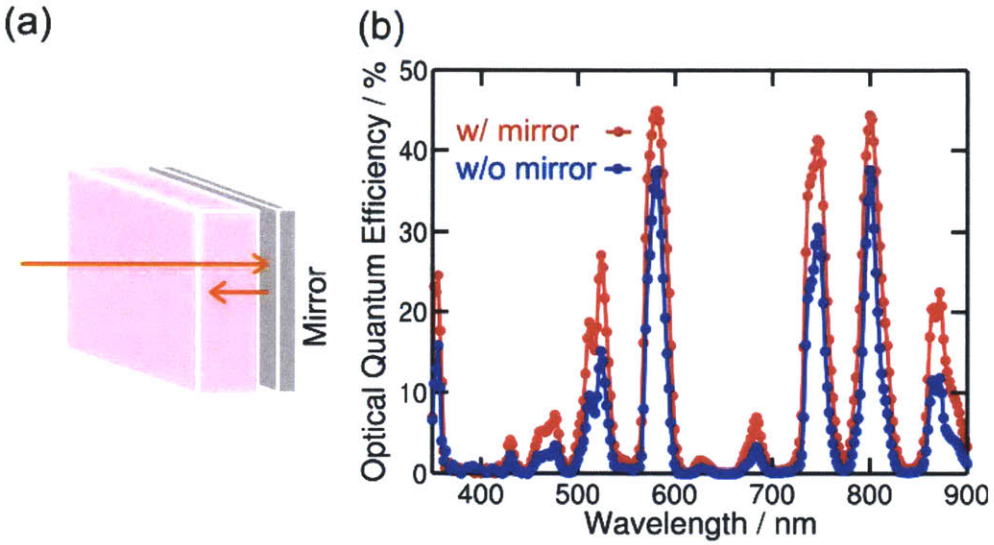

Fig. 4.8 (a) Back reflector to increase solar absorption. (b) Optical quantum efficiency as a function of wavelength for 25 X 25 X 5 mm APG-1 1% wt. Nd_2O_3 doping without (blue) and with (red) back mirror.

Cascade energy transfer from a 3% wt. CdSe/CdZnS in PVB-CVA-CVAc polymer thin film to Nd^{3+} was investigated for both a 1 mm (Fig. 4.9.a) and 5 mm (Fig. 4.9.b) thick Nd^{3+}:glass waveguide. For the thin Nd^{3+}:glass waveguide, a doping of 2% wt. Nd_2O_3 was chosen for to balance the low thickness. The optical quantum efficiency as a function of wavelength of a 25 x 25 x 1 mm APG-1 with 2% wt. Nd_2O_3 doping without (blue) and with (red) a 3% wt.

CdSe/CdZnS in PVB-CVA-CVAc polymer thin film with back mirror is shown in Fig. 4.9.b. With the cascade energy transfer, a broad peak from 350-500 nm that follows the nanocrystal absorption curve appears with peak OQE of 22%. This result demonstrates efficient radiative energy transfer of small volume Nd^{3+}:glass waveguides. To increase the energy transfer, by maximizing the ratio in Eq. 4.2, we move to a 5 mm thick Nd^{3+}:glass waveguide while reducing the Nd_2O_3 doping to 1% for increased photoluminescence quantum yield. The optical quantum efficiency as a function of wavelength of a 25 x 25 x 5 mm APG-1 with 1% wt. Nd_2O_3 doping without (blue) and with (red) a 3% wt. CdSe/CdZnS in PVB-CVA-CVAc polymer thin film with back mirror is shown in Fig. 4.9.d. By moving to a thicker waveguide, the peak optical quantum efficiency in the spectral region of the nanocrystal is increased from 22% to 28%. We can determine the power efficiency by multiplying the OQEs in Fig. 4.9.d with AM1.5 solar irradiance and taking the EQE, FF, and Voc of a SunPower solar cell. For Nd^{3+}:glass waveguides without (blue) and with (red) cascade energy transfer, the power efficiency is 2.4% and 3.4% respectively, an enhancement of 40%. The power efficiency can clearly be enhanced further by moving to efficient near infrared nanocrystals to increase the overlap between system absorption and sunlight.

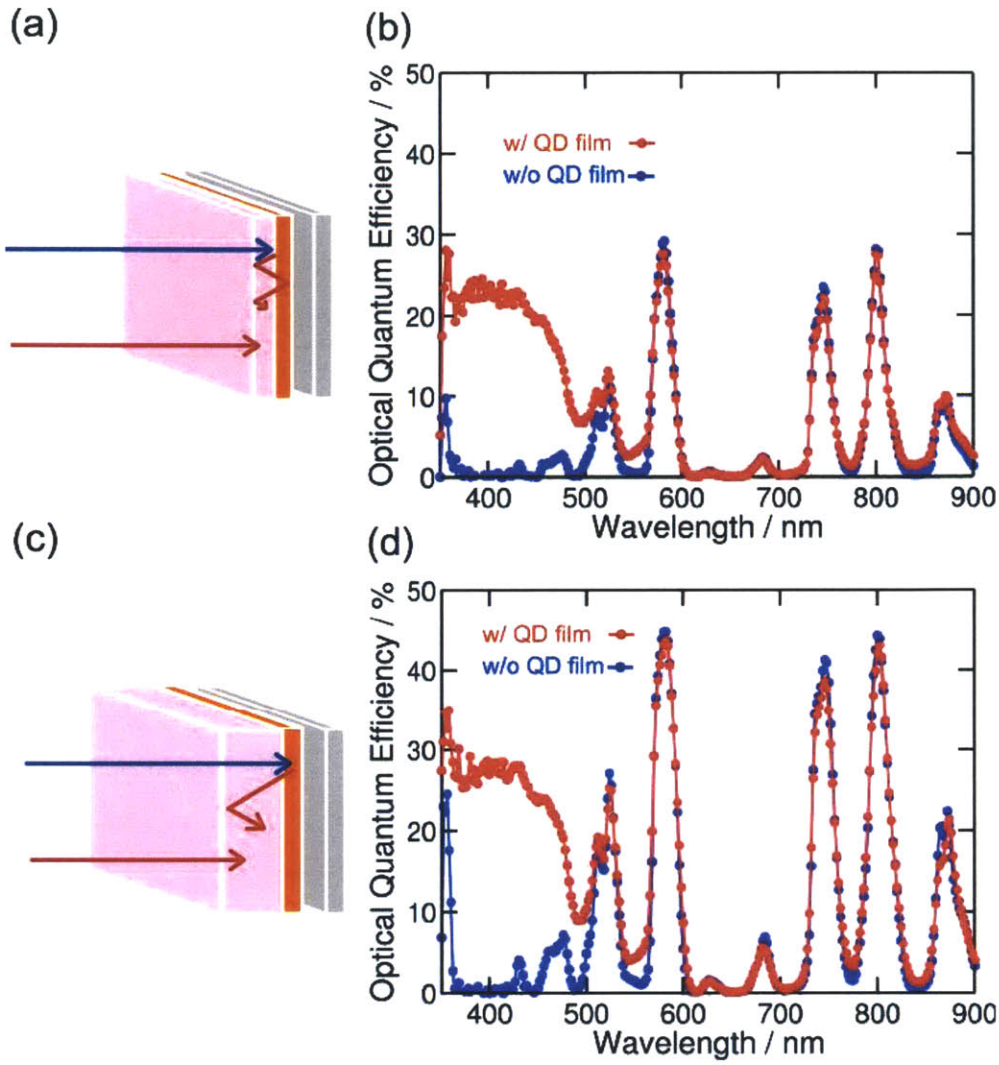

Fig. 4.9 (a) Cascade energy transfer for thin Nd^{3+}:glass waveguide with back mirror. (b) Optical quantum efficiency as a function of wavelength for 25 X 25 X 1 mm APG-1 2% wt. Nd_2O_3 doping without (blue) and with (red) 3% wt. CdSe/CdZnS in PVB-CVA-CVAc thin film with back mirror. (c) Cascade energy transfer for thick Nd:glass waveguide with back mirror. (d) Optical quantum efficiency as a function of wavelength for 25 X 25 X 5 mm APG-1 1% wt. Nd_2O_3 doping without (blue) and with (red) 3% wt. CdSe/CdZnS in PVB-CVA-CVAc thin film with back mirror.

4.2.3 Geometric Gain

The efficient performance of LSCs at large geometric gain is critical to reduce overall system costs. The Monte Carlo ray tracing model (chapter 3) is used to gain insight in how the efficiency of Nd^{3+}:glass, CdSe/CdZnS nanocrystal, and cascade energy transfer based LSCs scale. The measured experimental parameters that are used as inputs to the simulation can be seen in Fig. 4.10. The photoluminescence quantum yield of APG-1 1% wt. Nd_2O_3 and 3% wt. CdSe/CdZnS in PVB-CVA-CVAc were 70% and 85% respectively. For each geometric gain, 100,000 photons were simulated.

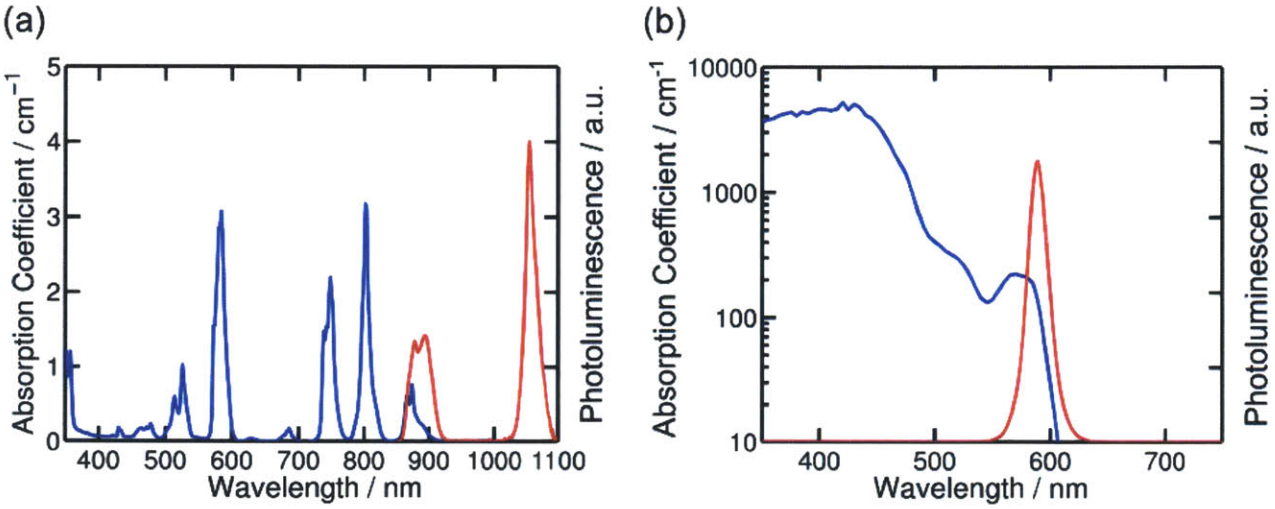

Fig. 4.10 Experimental absorption coefficient (blue) and photoluminescence (red) versus wavelength of (a) APG-1 1% wt. Nd_2O_3 (linear scale) (b) and 3% wt. CdSe/CdZnS in PVB-CVA-CVAc (log scale) used in Monte Carlo ray tracing model.

The simulated optical quantum efficiency as a function of geometric gain of Nd^{3+}:glass, CdSe/CdZnS nanocrystal, and the hybrid system can be seen in Fig. 4.11. To differentiate between the performance of the two emitters, input light of 405 nm (blue) was used to only photoexcite the nanocrystal film and 802 nm (red) to only photoexcite neodymium. As can be

seen in Fig. 4.11, the modelled Nd^{3+}:glass scales with little transport losses due to the low self-absorption making it an attractive LSC emitter. While the simulated high self-absorption material of the nanocrystal doped polymer suffer significant transport losses and lose efficiency rapidly with increasing geometric gain. By making use of cascade energy transfer, the simulated optical quantum efficiency spectral region associated with the nanocrystal now scales to high geometric gains as neodymium.

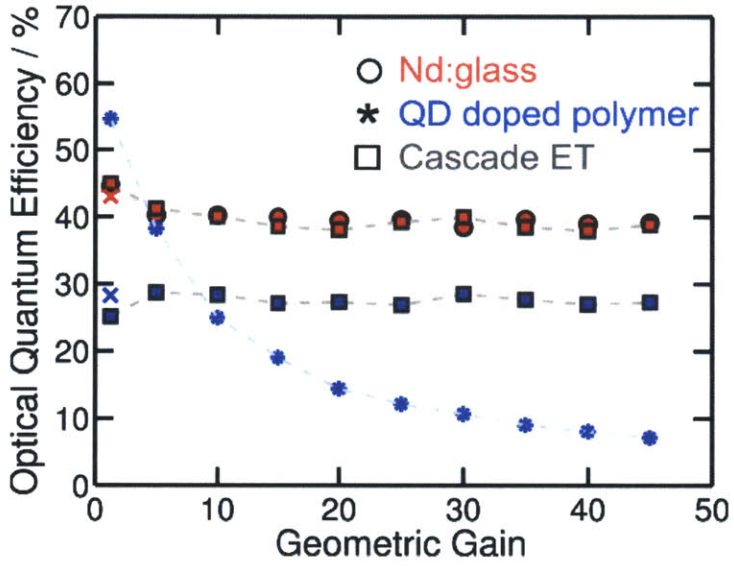

Fig. 4.11 Simulated optical quantum efficiency as a function of geometric gain for APG-1 1% wt. Nd_2O_3 (circle), 3% wt. CdSe/CdZnS in PVB-CVA-CVAc on glass (asterisk), and APG-1 1% wt. Nd_2O_3 with 3% wt. CdSe/CdZnS in PVB-CVA-CVAc (square) all with back reflectors. Excitation wavelength of 405 nm (blue) and 802 nm (red).

4.3 Conclusion

In summary, we have discussed that both Nd^{3+}:glass and colloidal nanocrystals have strengths making them attractive emitters for infrared LSCs, but their weaknesses ultimately would limit their overall utility. By combining these two materials through cascade energy transfer, we have shown that colloidal nanocrystals can be efficient solar absorbers and energy donors to neodymium emitting acceptors. Peak optical quantum efficiencies of 43% in a Nd^{3+}:glass based LSC are demonstrated with simulated high geometric gain performance. With cascade energy transfer, the optical quantum efficiency in the visible of a Nd^{3+}:glass is significantly improved with peak efficiency of 28%. The overall power efficiency of the system is enhanced from 2.4% to 3.4%, an enhancement of 40%. To improve cascade energy transfer, an infrared emitting nanocrystal [48] to improve solar absorption would offer further enhancements in power efficiency for a silicon solar cell compatible LSC.

Chapter 5

Cascade Energy Transfer for Solar Powered Lasers

Nonlinear optics for solar energy conversion and storage

5.1 Motivation for Solar Powered Lasers

The idea of directly converting broad-band solar radiation into coherent and narrow-band laser radiation could enable many attractive technologies for solar energy. Two interesting applications of solar powered lasers are: (1) upconversion of sub-bandgap sunlight via second-harmonic generation for high efficiency solar cells and (2) renewable chemical storage of solar energy as an alternative to fossil fuels. To achieve these goals, the lasers must be of high efficiency and economical.

5.1.1 Upconversion

In a conventional single-junction solar cell, a photon with energy below the bandgap cannot photoexcite electrons from the valence band to the conduction band, ultimately all being lost to the environment as heat. Upconversion for solar energy generation is a process that combines two (or more) sub-bandgap photons into one photon with energy greater than the bandgap. This process can lead to an electron per multiple absorbed sub-bandgap photons, promising for photovoltaics with efficiencies beyond the Shockley-Queisser (SQ) limit.

Upconversion of sub-bandgap sunlight is an active field of research to increase the efficiency of single junction solar cells. The majority of work on solar upconversion makes use of a common scheme, albeit with different material systems. A schematic of the common method employed in solar upconversion is pictured in Fig. 5.1. The method involves a system that has discrete energy levels which are energetically spaced apart in near integer steps, similar to the rungs in a ladder. A sub-bandgap photon excites an electron to the lowest unoccupied energy level. Within the excited electrons lifetime, a second sub-bandgap photon is absorbed and transferred to the excited electron, promoting it further up the energy ladder. The excited electron then radiatively recombines emitting a photon with twice the energy of the input light.

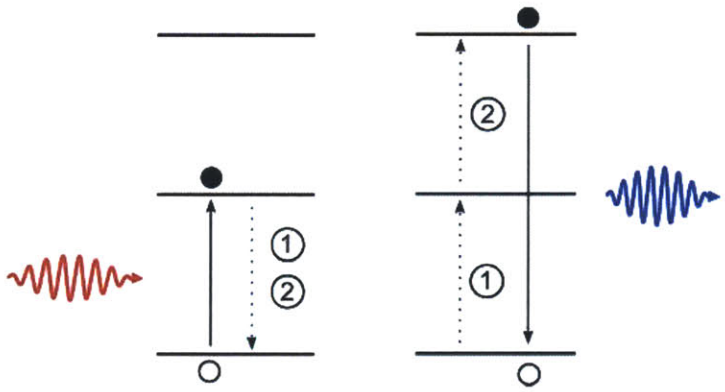

Fig. 5.1 Schematic of the process of incoherent photon upconversion. A material with discreet energy levels with integer spacing is shown. A sub-bandgap photon (red) excites an electron to the lowest unoccupied energy level. A second low energy photon that is absorbed within the electron's radiative lifetime can promote it to a higher energy state. The electron radiatively recombines to the ground state emitting a photon (blue) with twice the energy of the input light.

Although significant research has been invested on the method shown in Fig. 5.1, this scheme has yet to show reduced costs for commercial solar cells. There are two main factors that limit the efficiency of this type of upconversion. First, due to this process being a multiple

photon event, the efficiency is dependent on the intensity of input light. While sunlight is an incredible large source of energy, it is distributed over an incredible large area making it a relatively low intensity source of energy. Secondly, the poor solar overlap between sunlight and absorption of the best studied materials limit the efficiency of the process. For this type of upconversion, common upconversion materials are atomic absorbers and emitters such as erbium (Er^{3+}). Erbium has limited sub-bandgap solar absorption due to its narrow (FWHM < 80 nm) and low (α < 10 cm^{-1}) absorption coefficients. It has been recently shown for Er^{3+}:$NaYF_4$ crystals [50], that for moderate upconversion efficiencies of 1.2% +/- 0.1 require a solar intensity of 6.01 X 10^3 suns.

This begs the question: is solar photon upconversion inherently inefficient and costly? One path to address the first question is to make use of a well-known efficient upconversion technology called second-harmonic generation. Second-harmonic generation is a nonlinear optical process where photons of the same energy and phase interact with a nonlinear material effectively combine to generate new photons with twice the energy of the initial photons (Fig. 5.2). The efficiency of this process is given by:

$$\eta = \left(\frac{\sin(\frac{\Delta kL}{2})}{\Delta kL/2} \right)^2 \tag{5.1}$$

where $\Delta k = 2k_\omega - k_{2\omega}$ is the wavevector mismatch of the process, L is the nonlinear material length. This equation has a maximum when $\Delta k = 0$ where $\eta = 1$. This is difficult to achieve in ordinary materials due to frequency dispersion. Birefringent crystals offer a way to achieve Δk = 0 through modifying the refractive indices and tuning the phase matching. Second-harmonic generation has shown conversion efficiencies of greater than 80% [51]. The phase matching condition for high efficiency limits this process to coherent monochromatic light. For this reason, this process is used extensively in efficient frequency conversion of laser light for a range of

applications such as fusion research, commercial green laser pointers, and as a tool to study material properties in research. This process demonstrates upconversion is not inherently inefficient or costly, but it does not answer the question of whether solar photon upconversion can be efficient and cheap. To use sunlight with nonlinear optical processes such as second-harmonic generation, sunlight must first be converted to a coherent monochromatic laser beam via an efficiency and cheap solar powered laser.

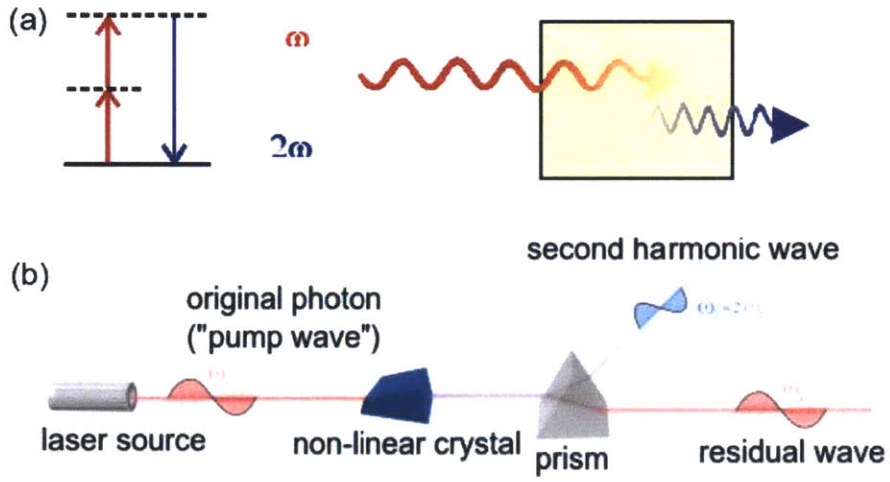

Fig. 5.2 (a) Schematic of the process of coherent photon upconversion. (b) Diagram of the second-harmonic generation process.

5.1.2 Historical Solar Powered Lasers

Many state-of-the-art laser systems share many of the characteristics of the first demonstration of a laser operating in the optical region of the spectrum, performed at the Hughes Research Laboratory in 1960 [ ]. Deveolped and performed by Theodore H. Maiman, a fluorescent ruby crystal with silver coatings on parallel polished faces was optically irradiated by a high power flashlamp achieving the first successful operation of the laser. Fifty years later from

this initial demonstration, many of the most efficient and powerful lasers today have retained the basic elements of this original design, the solid-state active medium and optical energy pump. For similar reasons, state-of-the-art solar powered lasers make use of the same solid-state active medium, but replace the flashlamp with a concentrated sunlight optical pump.

The first solar pumped laser was reported by RCA Labratories in 1963, only three years after the first demonstration of the laser, based on a Dy^{2+}:CaF_2 crystalline system [52] (Fig. 5.3.a). Since then many advances in the optical gain media and solar collector design have occurred [53-58]. The most common optical gain media used in solar pumped lasers today is the rare earth ion neodymium (Nd^{3+}) due to its natural four-level system, high emission cross-section, and long excited state lifetime. Nd^{3+}:YAG laser rods, for example, operate at power thresholds of 275 W-cm^{-2} utilizing large Fresnel lenses to concentrate sunlight [54] (Fig. 5.3.b). Nd^{3+}:YAG ceramics sensitized by Cr^{3+} ions have broad absorption bands in the visible spectrum, and solar lasing thresholds of 160 W-cm^{-2} [53, 55]. Finally, S. Mizuno *et al.* demonstrated passive cooling of a solar pumped laser through the use of a small volume Nd^{3+}-doped glass fiber operating at a solar lasing threshold of 370 W-cm^{-2} [58]. Despite the favorable optical gain properties of Nd^{3+}, these state-of-the-art solar pumped lasers operate at pump concentrations above 1000 suns, making them economically expensive and incompatible for sub-bandgap sunlight upconversion.

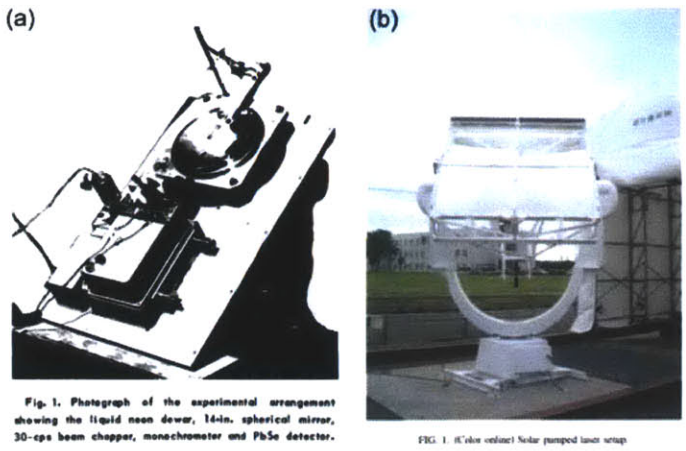

Fig. 5.3 (a) Photograph of first demonstration of solar pumped laser from [52]. (b) Photograph of state-of-the-art solar pumped lasers [54] utilizing Fresnel concentrators.

To understand the large solar concentration threshold in state-of-the-art solar pumped lasers, it is informative to explore the requirements for oscillation to occur. The laser is composed of a resonant optical amplifier whose output is fed back in to the input with matching phase (Fig. 5.4). The two conditions that must be statisfied for oscillation to occur: (1) the amplifier gain must be greater than the loss in the feedback system, and (2) the total phase shift in a single round trip must be a multiple of 2π. The laser is an optical amplifier in which the amplifier is the pumped solid-state active medium (Nd^{3+}). Feedback is achieved by placing the active medium in an optical resonator, which bounces the light back and forth between mirrors.

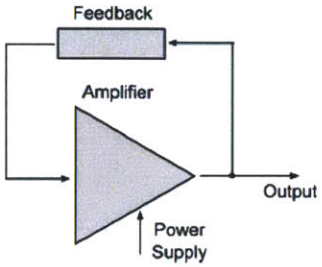

Fig. 5.4 An oscillator is comprised of an amplifier, a feedback system, and an output coupling scheme.

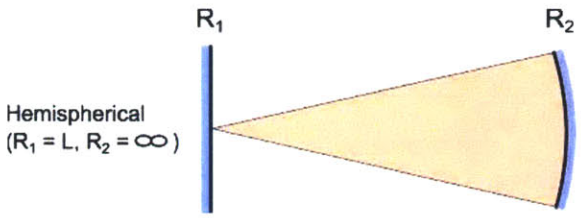

Fig. 5.5 Schematic of optical feedback in a hemispherical resonator.

Optical feedback is achieved by placing the active medium in an optical resonator. The hemispherical resonator is a common example of a stable optical resonator as schematically shown in Fig. 5.5. Output coupling is realized by making one of the resonator mirrors partially transmitting. The output coupling largely defines the photon loss in the system and hence the threshold pumping rate as seen later. The photon-flux density is reduced by the factor $R_1R_2\exp(-2\alpha_s d)$, where R_1 and R_2 are the reflectances of the resonator mirrors and α_s is the material loss due to scattering and absorption. The overall distributed loss coefficient α_r is

$$\alpha_r = \frac{1}{2d}\ln\left(\frac{1}{R_1}\right) + \frac{1}{2d}\ln\left(\frac{1}{R_2}\right) + \alpha_s \tag{5.2}$$

For the initiation of laser oscillate, the small-signal gain coefficient, $\gamma_0(\nu)$, must be greater than the overall system loss, α_r.

$$\gamma_0(\nu) = N_0\sigma(\nu) > \alpha_r \tag{5.3}$$

The small-signal gain coefficienct is proportional to the equilibrium population density difference, N_0, which in turn increases with the pumping rate, R, and the stimulated emission cross-section, $\sigma(\nu)$. The relationship between population and pumping rate can be seen from the schematic of the relevant energy levels and decay rates for a four-level pumping system is shown in Fig. 5.5 and the rate equations, Eq. 5.4.

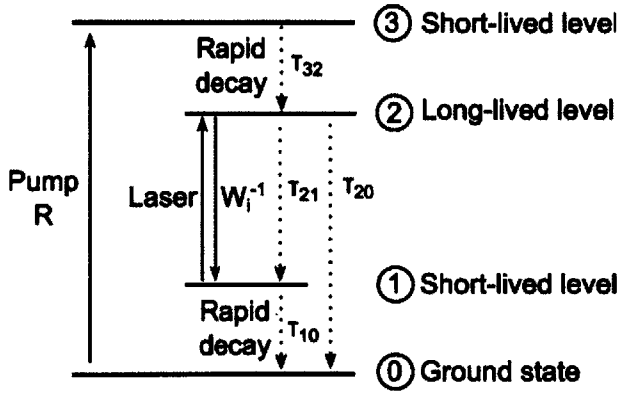

Fig. 5.5 Four-level system energy levels and decay rates.

In the absence of radiation near the resonance, the rates of increase of the population density from pumping are,

$$\frac{dN_2}{dt} = R_2 - \frac{N_2}{\tau_2} \tag{5.4.a}$$

$$\frac{dN_1}{dt} = -R_1 - \frac{N_1}{\tau_1} + \frac{N_2}{\tau_{21}} \tag{5.4.b}$$

Under steady-state conditions ($dN_1/dt = dN_2/dt = 0$), the population difference, $N_0 = N_2 - N_1$, is

$$N_0 = R_2\tau_2\left(1 - \frac{\tau_1}{\tau_{21}}\right) + R_1\tau_1 \tag{5.5}$$

For a four-level system such as Nd^{3+}, the upper level should be pumped strongly and decay slowly so that it retains its population and the lower level should depump strongly so that it disposes of its population. Under these conditions the steady-state population difference simplifies to

$$N_0 \approx R_2 t_{sp} \tag{5.6}$$

The gain of the optical amplifier is proportional to the difference in population which is proportional to the pumping transition. The gain condition is satisfied when the gain coefficient is greater than the loss coefficient as shown in Eq. 5.3. The minimum pumping rate for the initiation of laser oscillation is termed the threshold population difference, N_t, is

$$N_0 > N_t = \frac{\alpha_r}{\sigma(v)} \tag{5.7}$$

Hence the required threshold population difference of a solar pumped laser is proportional to the pumping rate.

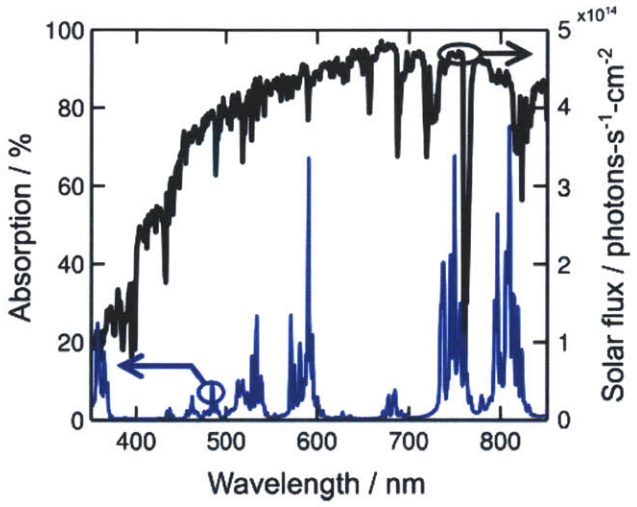

Fig. 5.6 Absorption (blue) of 1% at. Nd^{3+}:YAG. The poor spectral overlap between sunlight (black) and Nd^{3+}:YAG can be seen, leading to large gain volumes and solar concentration thresholds in Nd^{3+}:YAG based solar pumped lasers.

While the neodymium ion's large stokes shift and small scattering coefficient, large stimulated emission cross-section, and good thermal properties have made it the dominant gain material for solar pumped lasers, its discrete absorption lines (Fig 5.6) and low absorption coefficient (the peak absorption coefficients of neodymium are less than $< 5\ cm^{-1}$ for moderately

doped hosts (< 1%)) pose a problem for broad wavelength excitation. Consequently, in state-of-the-art solar pumped lasers use relatively large laser rods (6 mm diameter, 100 mm length) to achieve efficient solar absorption. While larger gain volumes result in increased solar pump absorption, the equivalent increase in mode volume cancels out the increase in excitation density of the mode that is essential for reaching population inversion. Consequently, state-of-the-art solar pumped lasers operate above 1000 suns.

5.2 Cascade Energy Transfer for Solar Powered Lasers

An attractive gain material for solar pumped lasers would be to use a nanocrystal's efficient solar absorption as the energy donor to the emitting acceptor of neodymium for its large stimulated emission cross-section and low self-absorption. As shown previously, nanocrystal donors and neodymium acceptors can be coupled through cascade energy transfer (radiative energy transfer) [59] due to their complementary optical properties In this work we make use of cascade energy transfer to decouple solar pump absorption and optical gain, thereby enabling solar pumped lasers with efficient solar absorption in small mode volumes.

5.2.1 Cascade Energy Transfer

A schematic of the proposed optical energy transfer process is shown in Fig. 5.7. The scheme begins with incident sunlight absorbed by the luminescent colloidal nanocrystals. These are ideal solar downshifting materials due to their stability [60], spectrally broad absorption profile, absorption coefficients of $>10^5$ cm^{-1}, narrow photoluminescence spectrum, and high photoluminescence quantum yield [61]. The absorbed incident light within the nanocrystal is then re-emitted as photoluminescence. As in the operation of a luminescent solar concentrator

(LSC) [29-31], a fraction of the emitted photoluminescence is trapped within the optical gain media waveguide due to total internal reflection. The trapping efficiency is a function of refractive index [30], but for typical dopant hosts such as polymers and glass with n = 1.5, the fraction of trapped photoluminescence is approximately 75%. The waveguided photoluminescence can be tuned to the peak absorption of the optical gain medium through the size dependent quantum confinement effect in nanocrystals. The waveguided photoluminescence ultimately resulting in optically excited states within the waveguide. As with an LSC, the photoluminescence pump concentration can be increased by reducing the thickness of the waveguide, enabling low threshold, small volume solar pumped lasers. Cascade energy transfer [59] enables large Stokes shifts between solar absorption and optical gain emission, a necessary condition for very-low-threshold daylight-pumped lasers as outlined by Roxio and Yablonovitch [62].

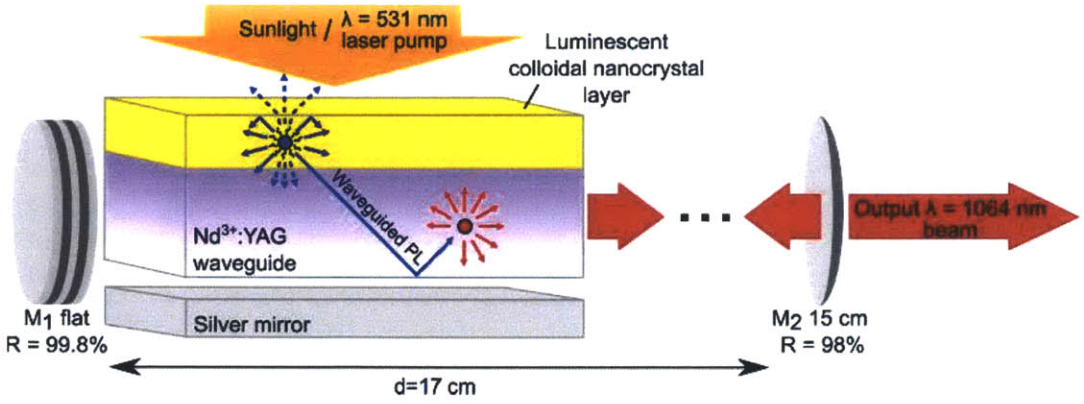

Figure 5.7 Illustration of cascade energy transfer for solar pumped lasers. A luminescent colloidal nanocrystal film (yellow) is optically coupled to the planar optical gain waveguide (purple). Incident sunlight is absorbed by the luminescent layer and largely re-emitted into waveguide modes. As the luminescence propagates in the waveguide, energy is transferred to the optical gain media through optical absorption. The optical gain media is then placed into a hemispherical resonator for a solar pumped laser via cascade energy transfer.

5.2.2 Excited State (Nd^{3+}) Efficiency and Distribution

As a proof of principle, a 1% at. Nd^{3+} doped yittrium aluminum garnet (YAG) planar waveguide of dimensions 43 mm × 2 mm × 750 μm corresponding to length, width, and thickness respectively. The Nd^{3+}:YAG slab waveguide was formed through conventional polishing techniques from commercial laser rods of diameter 3 mm and length of 43 mm with λ = 1064 nm antireflection coatings on both faces. Organic soluble CdSe/CdZnS colloidal semiconductor nanocrystals that emit at 585 nm were provided by QD Vision, Inc. The received nanocrystals were precipitated once with isopropyl alcohol prior to use. The poly(vinyl butyral-co-vinyl alcohol-co-vinyl acetate) (PVB-CVA-CVAc) host was purchased from Sigma Aldrich. A solution of 100 mg/mL 10% wt. CdSe/CdZnS:PVB-CVA-CVAc in chloroform was drop cast onto the Nd^{3+}:YAG waveguide producing a film of 15 μm thickness. The quantum yield of the colloidal nanocrystals is 75% when doped into PVB-CVA-CVAc, with the film being photostable in air. The overlap between the solar spectrum and the absorption of the CdSe/CdZnS:PVB-CVA-CVAc thin film can be seen in Fig. 5.8.a, showing the broad solar absorption of the nanocrystals. The narrow emission and tunability of the waveguided nanocrystal photoluminescence allows efficient pumping of the narrow absorption peaks of Nd^{3+}:YAG. Indeed, as shown in Fig. 5.8.b, the CdSe/CdZnS photoluminescence is tuned to neodymium's main absorption peak in the visible at 585 nm. A disadvantage of the chosen nanocrystal emitter, however, is the small Stokes shift between absorption and emission, which leads to reabsorption and eventually loss of the waveguided photoluminescence [30]. Self-absorption losses can be reduced in future interations through energy transfer methods [5], Stokes shift engineered nanocrystals [34, 35], and optical techniques [63] to reduce the overlap between absorption and emission of the luminescent emitter.

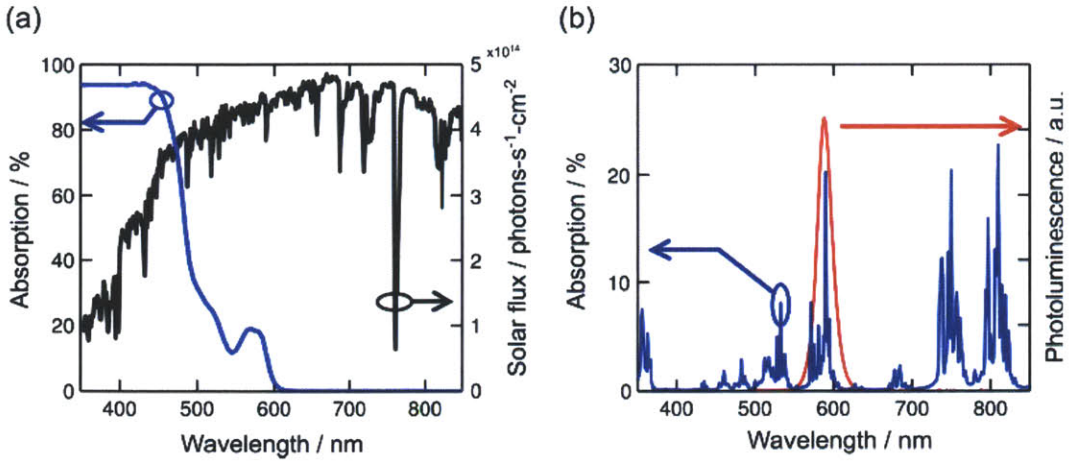

Figure 5.8 a. Absorption of the luminescent colloidal film, 10% wt. CdSe/CdZnS:PVB-CVA-CVAc (blue), overlaid on the AM1.5 solar flux (black). Sunlight can be efficiently absorbed by the colloidal nanocrystals due to their broad and large absorption coefficients. **b.** The luminescence of the nanocrystal (red) is tuned to an absorption peak of the Nd^{3+}:YAG (blue), for efficient waveguided luminescent pumping of optical gain media.

To measure the efficiency of cascade energy transfer from input light to excited Nd^{3+} ions, the Nd^{3+}:YAG waveguide is illuminated by monochromatic light with and without a 15-μm-thick 10% wt CdSe/CdZnS:PVB-CVA-CVAc thin film. To increase the absorption of the incident light within the sample, a simple backing silver mirror is employed. The monochromatic light was generated using a tungsten bulb, monochromator with a spectral resolution of 3.5 nm full width at half maximum, and a mechanical chopper. The sample photoluminescence was collected with an integrating sphere and measured with a lock-in amplifier, spectrally calibrated photodetector, and long wavelength filters were used to discriminate between Nd^{3+}:YAG and CdSe/CdZnS emission in the integrating sphere. Although the fine structure of the Nd^{3+} absorption is partly obscured by the resolution of the monochromator, its spectral resolution does not affect calculations of the equivalent solar threshold obtained by integrating the product of solar and device excitation spectra. The key parameter is the cascade energy transfer, which we

define as the fraction of pump photons ultimately transferred to Nd^{3+}. The cascade energy transfer depends on the nanocrystal absorption, photoluminescent quantum yield, the fraction of nanocrystal photoluminescence trapped in the waveguide, and the competition between photoluminescence reabsorption losses in the nanocrystal film and waveguided pumping of the optical gain media. As can be seen in Fig. 5.9.a, the Nd^{3+}:YAG sample alone has very little absorption in the visible spectrum. With the addtion of the thin film of CdSe/CdZnS:PVB-CVA-CVAc on the Nd^{3+}:YAG waveguide, cascade energy transfer generates a broad visible excitation spectrum with peak value of 14% that follows the absorption profile of the nanocrystal. Averaged over the solar spectrum out to the nanocrystal absorption cutoff at $\lambda = 600$ nm, the waveguide pump efficiency due to the nanocrystal is 8.6%; see grey dashed line in Fig. 5.9.a. This result demonstrates the transfer of optical power to small volume optical gain media via a broadly absorbing luminescent colloidal nanocrystal intermediate.

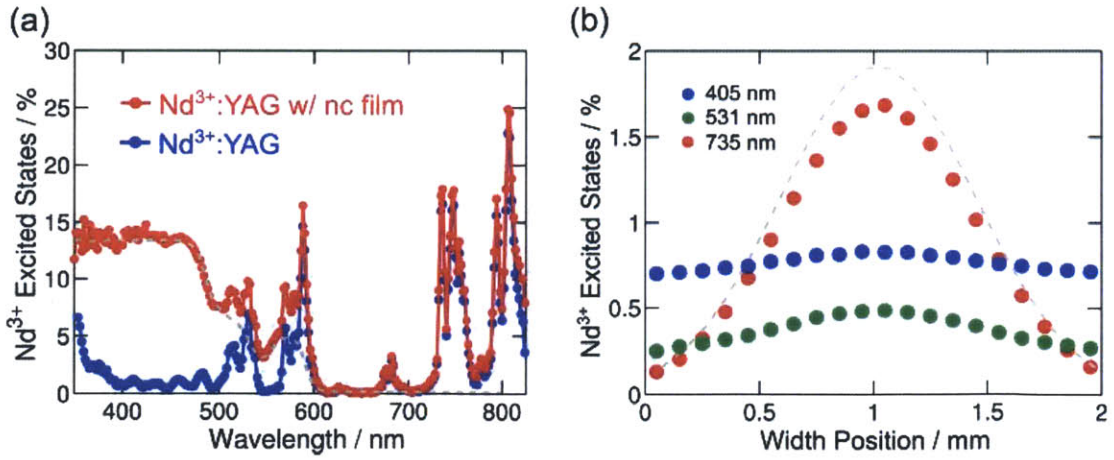

Figure 5.9 a. Excitation spectra of a 750-μm-thick Nd^{3+}:YAG crystal (blue), and the same crystal with a 10% wt. CdSe/CdZnS:PVB-CVA-CVAc coating (red). Scaled double pass absorption of the colloidal nanocrystal film is shown as a dashed gray line. **b.** Modelled Nd^{3+} excited state distribution in the Nd^{3+}:YAG coated waveguide for incident photons of wavelength $\lambda = 405$ (blue dots), 531 (green dots), and 735 (red dots) nm from the Monte Carlo ray tracing simulation. The input photon spatial distribution is shown as a dashed gray line.

A Monte Carlo ray tracing simulation was developed to model the effect of cascade energy transfer on the distribution of excited Nd^{3+} within the waveguide. The inputs to the simulation are the sample geometry, the material's spectral absorption coefficients and refractive indices, photoluminescence spectrum, and photoluminescence quantum yield. An input elliptical gaussian beamshape is used to simulate concentrated input light, with standard deviation $\sigma_W = 1$ mm and $\sigma_L = 26$ mm along the width and length of the sample respectively. The fraction of incident photons resulting in excited Nd^{3+} summed along the length and the thickness of the Nd^{3+}:YAG waveguide is shown in Fig. 5.9.b for three different input wavelengths. At input wavelength of $\lambda = 735$ nm, only excitation of neodymium occurs, the resultant modelled Nd^{3+} excited states mirroring the non-uniformity of the input intensity as expected from direct absorption of input light. When only the luminescent nanocrystal is excited with input wavelength of $\lambda = 405$ nm, the cascade energy transfer produces a near uniform Nd^{3+} population despite the incident intensity non-uniformity. The improved uniformity is a result of the relatively long absorption depth of waveguided photoluminescence compared to the sample thickness. The modelled total integrated Nd^{3+} excited states for input wavelength of $\lambda = 405$ nm is 15.3% compared to the measured 14%. The slight discrepency between simulation and experiment may be due to scattering at surfaces which is not included in the model. For input wavelengths that excite both neodymium and the nanocrystal, such as $\lambda = 531$ nm, the resultant excited state profile is a weighted average of direct absorption and cascade energy transfer. The modelled total integrated Nd^{3+} excited states for input wavelength of $\lambda = 531$ nm is 7.4% compared to the measured 6.3%. These simulations indicate that cascade energy transfer will result in improved uniformity of excited state population and also thermal distribution within the optical gain media.

5.2.3 Solar Lasing Threshold

To determine the expected system solar laser threshold, the population inversion threshold of the Nd^{3+}:YAG coated planar waveguide must be known. To determine the threshold, the sample is placed in a cavity and is excited with an 18 W $\lambda = 531$ nm laser with spot size as defined in the Monte Carlo ray tracing simulation as illustrated in Fig. 5.7. The laser resonator is a hemispherical cavity with a planar mirror of reflectivity 99.8% and an output mirror with a radius of curvature of 15 cm and reflectivity of 98%. We observe that the doped PVB-CVA-CVAc polymer films used in this study are thermally stable for CW pumping below 10 W/cm^2 without active cooling, as seen in the inset of Fig. 5.10.b. To eliminate the possibility of thermal degradation of the polymer films we employ a quasi-CW scheme with pump pulse widths of approximately 10 ms. We observe both spectral narrowing of the main Nd^{3+} transition at $\lambda = 1064$ nm and threshold behavior at an incident power of 7.9 W, shown in Fig. 5.10.a and 5.10.b respectively. An Acton spectrometer with a grating of 1000 grooves per mm and a calibrated Newport photodetector and neutral density filter were used to measure the lasing spectrum and power threshold of the laser respectively. As modelled in Fig. 5.9.b, the gain is maximum in the centeral portion of the sample with 0.49% of the incident photons generating excited Nd^{3+} in this volume. This results in an experimental population inversion of 7.35×10^{21} Nd^{3+}-m^{-3}.

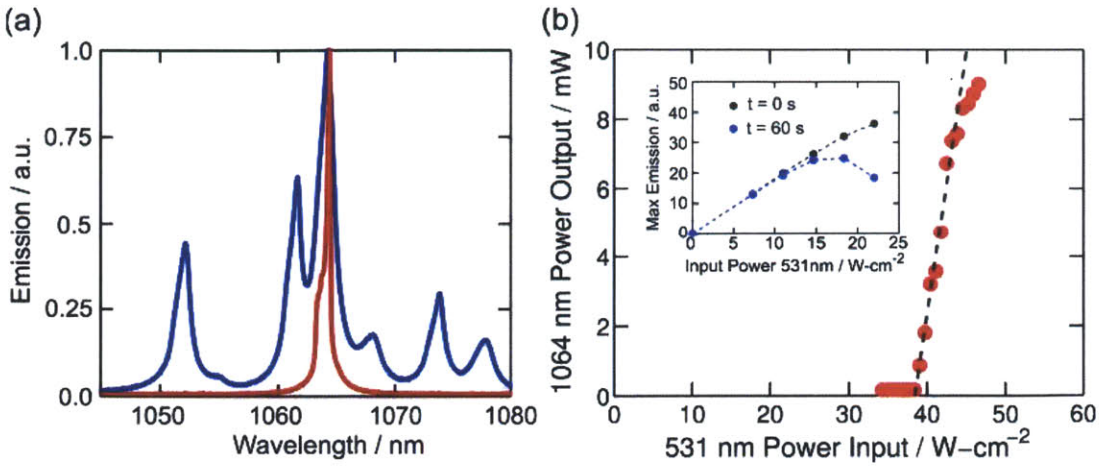

Figure 5.10 a. Emission spectrum below and above threshold. **b.** Lasing power at λ = 1064 nm versus pump intensity showing a lasing threshold of 7.9 W. Inset showing nanocrystal photoluminescence versus pump intensity at t = 0 min and t = 1 min. Above 10 W-cm^{-2}, the steady-state stability of the polymer doped film is reduced. A quasi-CW pump was used for lasing experiments.

Obtaining the same density of excited Nd^{3+} states in the sample from broadband solar excitation (Fig. 5.8.a) of the nanocrystals and subsequent cascade energy transfer (dashed grey line Fig. 5.9.a) requires a concetrated solar intensity of 36 W/cm^2 or 360 solar constants. Including the contribution of direct absorption by Nd^{3+} (red line Fig. 3a), the equivalent solar concentration is reduced to 20 W/cm^2 or 200 solar constants.

5.3 Outlook

The efficiency of cascade energy transfer can be improved through three methods: (i) enhanced solar absorption with near-infrared (NIR) rather than visible spectrum colloidal nanocrystals [65], (ii) higher efficiency waveguide pumping via low self-absorbing colloidal nanocrystals through increased Stokes shift [34, 35], and (iii) smaller mode volume optical gain media [65]. The dependence of the laser threshold on the properties of the luminescent concentrator can be seen in Fig. 5.11. By moving to a NIR absorbing and emitting colloidal nanocrystal, the amount of photons available to the gain material would double, reducing the gain threshold by a factor of two. This should also result in less heat in the gain material due to NIR rather than visible spectrum pumping of Nd^{3+}:YAG. But the largest improvement is expected by improving the photoluminescence quantum yield of the colloidal nanocrystals and increasing the Stokes shift to reduce self-absorption of waveguided photoluminescence. These are key components in the waveguide pump efficiency plotted on the x-axis of Fig. 5.11. The improvement of waveguide pumping efficiency and solar absorption in the NIR could result in significant reduction in solar conentration threshold from this proof of principal system.

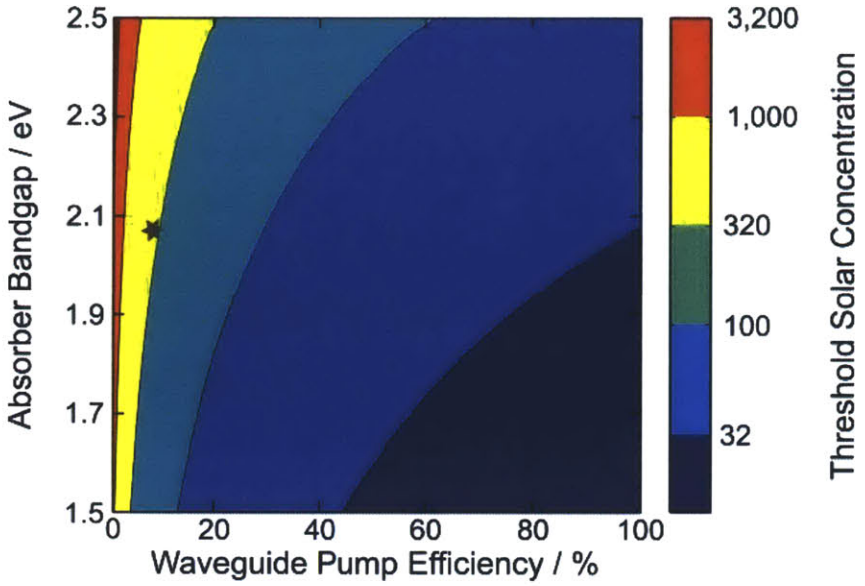

Figure 5.11 The calculated lasing threshold of the presented system as a function of the absorption edge of the luminescent colloidal nanocrystals and the efficiency of energy transfer to the gain medium, disregarding direct solar absorption by Nd^{3+}. The measured equivalent threshold solar concentration due to cascade energy transfer reported in this work is marked as a star.

In conclusion, cascade energy transfer presents a path to efficient solar powered lasers operating under passive cooling, and potentially even in the non-tracking regime [66]. The pairing of luminescent colloidal nanocrystals with traditional optical gain media such as Nd^{3+} and Tm^{3+} allows the decoupling of solar absorption from mode volume and enables solar laser operation from the visible to the near infrared. Solar powered Tm^{3+} lasers are especially notable because they potentially enable the efficient upconversion of sub-bandgap infrared sunlight for silicon solar cells.

Chapter 6

Conclusions and Outlook

In this thesis we focused on two paths to overcoming one of the barriers to widespread adoption of solar energy, the relative high cost. One path involved surmounting the Shockley-Queisser limit with singlet exciton fission to produce more electricity per input photon of sunlight. The other path makes use of Luminescent Solar Concentrators to reduce the overall installed system costs. To advance these two technologies, the processes of sunlight absorption and excitonic processes, such as singlet exciton fission and photoluminescence were separated by cascade energy transfer. Cascade energy transfer enabled us to combine imperfect materials into efficient systems for solar energy generation.

Chapter 2 focused on a method to effectively make any chromophore a potential singlet exciton fission material through appropriate pairing. This is an attractive, due to the limited number of materials that exhibit singlet exciton fission. The process of singlet fission is shown to be de-coupled from photon absorption, exciton diffusion, and charge transport by inserting a singlet fission material at the donor-acceptor (D-A) interface of an organic photovoltaic cell. Singlet excitons generated in the singlet exciton donor were transferred to the singlet fission material where they undergo singlet fission. This interlayer acts as a singlet fission sensitizer to the singlet donor. The enhancement in peak EQE in the spectral region associated with the singlet exciton donor, TPTPA, increased from 12.8% to 27.6% upon introduction of the rubrene singlet exciton fission sensitization layer. Although the efficiency of this cell is lower than the

best organic solar cells, this scheme is general and can be applied to any excitonic absorbing material to act as an antenna for singlet exciton fission materials. The singlet donor can be chosen for high photon absorption, exciton diffusion, and charge transport, and the singlet fission sensitizer can be selected for high singlet fission efficiency to achieve very high EQE organic photovoltaic cells.

To further reduce the cost of state-of-the-art LSC systems, Chapter 4 addressed replacing the high energy, high efficiency, and high cost solar cells such as GaAs or GaInP with low cost, high efficiency, and earth abundant silicon solar cells is required. We used a lanthanide ion--colloidal nanocrystal energy cascade system as a promising LSC emitter scheme for the silicon spectral region. By combining these two materials through cascade energy transfer, we have shown that colloidal nanocrystals can be efficient solar absorbers and energy donors to neodymium emitting acceptors. Peak optical quantum efficiencies of 43% in a Nd^{3+}:glass based LSC are demonstrated with simulated high geometric gain performance. With cascade energy transfer, the optical quantum efficiency in the visible of a Nd^{3+}:glass is significantly improved with peak efficiency of 28%. The overall power efficiency of the system is enhanced from 2.4% to 3.4%, an enhancement of 40%. To improve cascade energy transfer, an infrared emitting nanocrystal should be employed to improve solar absorption offering enhancements in power efficiency for a silicon solar cell compatible LSC.

In chapter 5, we explored the feasibility of high efficiency, low cost solar pumped lasers for solar energy generation. The problem with achieving simultaneously high efficiency and low cost is that the properties of solar pump absorption and lasing power threshold are connected by mode volume. Larger gain volumes resulting in increased solar pump absorption, the equivalent increase in mode volume cancels out the increase in excitation density of the mode that is

essential for reaching population inversion requiring a larger input power. To separate these important properties we made use of a luminescent solar concentrator, CdSe/CdZnS to optically excite a small volume gain media, Nd^{3+}:YAG. With the addtion of the luminescent thin film of CdSe/CdZnS:PVB-CVA-CVAc on the Nd^{3+}:YAG waveguide, cascade energy transfer generates a broad visible excitation spectrum with peak value of 14% that follows the absorption profile of the nanocrystal. Based on laser threshold measurements, cascade energy transfer should result in an expected power threshold of concetrated solar intensity of 36 W/cm^2 or 360 solar constants. Including the contribution of direct absorption by Nd^{3+}, the equivalent solar concentration is reduced to 20 W/cm^2 or 200 solar constants.

To conclude, this thesis addressed the high cost of solar energy by advancing the technologies of organic solar cells, luminescent solar concentrators, and solar pumped lasers. The future of these three technologies is unclear in light of recent work on perovskite solar cells and lasers. Perovskites have eclipsed organic solar cells in terms of efficiency yet share similar processing advantages and stability concerns. If multi-junction perovskites solar cells with high efficiency at low cost can be produced, the processes of unconversion and downconversion would become irrelevant for solar energy generation. Solar lasers may have an advantage over photovoltaics due to solar energy storage and the direct conversion of sunlight to coherent energy source. The advantage of the schemes proposed in this thesis is they are general and can incorporate and exploit the new material advances towards the goal of high efficiency and low cost solar energy.

Appendix A – Monte Carlo Ray Tracing Model Code

```
// LSC MCRT.cpp : Defines the entry point for the console application.
//

/*****************************************************************************
 * lsc_mcrt version 0.05                                                     *
 * Date: 11/2008                                                             *
 * Author:  Phil Reusswig.                                                   *
 *                                                                           *
 * Purpose:  The purpose of this program is to simulate a luminescent solar  *
 *       concentrator (LSC) via ray tracing and statistics (monte carlo).    *
 *                                                                           *
 * Usage:   The program takes one main input file:                           *
 *        -LSC_definition.txt                                                *
 *       The LSC_definition.txt file lists the name of the layers, the       *
 *       thickness (cm) of the layers, and the order in space.  For example: *
 *         air     0                                                         *
 *         organic  0.0006                                                   *
 *         glass    0.2                                                      *
 *         air     0                                                         *
 *       This is interpreted as the initial layer is air with zero           *
 *       thickness.  The next layer increasing in the +z-direction is layer  *
 *       organic with 0.0006 cm thickness.  And so on.                       *
 *                                                                           *
 *       The LSC_definition.txt file defines the remaining properties of     *
 *       the LSC.  These are as follows:                                     *
 *         -Geometric gain (G)                                               *
 *         -Photon's initial wavelength (nm)                                 *
 *         -Photon's incident angle (degrees)                                *
 *         -Number of photons                                                *
 *         -Mirror flag to enable mirrors                                    *
 *           +1: Use 2 side mirrors                                          *
 *           +0: Use all PV                                                  *
 *         -Mirror reflection coefficient                                    *
 *         -Simulation name                                                  *
 *                                                                           *
 *       These are the main inputs that characterize the LSC.  The           *
 *       program will also need input files that define the optical          *
 *       properties of each individual layer:                                *
 *         -Refractive index                                                 *
 *         -Absorption coefficient (cm^-1)                                   *
 *         -Photoluminescence                                                *
 *         -Internal Optical Quantum Efficiency                              *
 *       These will be named according to the layers.txt file as follows:    *
 *        -(layer name).txt                                                  *
 *       (ex. SF10.txt)                                                      *
 *       The first column of (layer name).txt will be the wavelength,        *
 *       second column will be refractive index, third column will be        *
 *       absorption coefficient, fourth column will be photoluminescence,    *
 *       and the fifth column will be photoluminescence efficiency.          *
 *       Each of these files should have the same spectral indexes, ex.      *
 *       300-800nm in 1nm steps.                                             *
 *                                                                           *
 *       Once the input files are created by the user, the program is        *
 *       executed.                                                           *
 *                                                                           *
 *       The output will be named "simulation name".txt.  The first column   *
 *       will be geometric gain.  Second column initial wavelength.  Third   *
 *       column initial theta.  Fourth column number of photons.  Fifth      *
 *       column %reflected.  Sixth column %transmitted.  Seventh column      *
 *       facial emission.  Eighth edge emission.  Ninth selfabsorption.      *
 *       Tenth mirror absorption...                                          *
 *                                                                           *
 *       The random number generator is from:                                *
 *       "Random Number Generators: Good Ones Are Hard To Find"              *
 *            Steve Park and Keith Miller                                    *
```

```
*          Communications of the ACM, October 1988                    *
*                                                                       *
************************************************************************/

#include <stdio.h>                          /*Library for file I/O*/
#include <stdlib.h>                 /*Library for conditional statements*/
#include <math.h>                   /*Library for trig functions and exp*/
#include "rngs.h"                           /*Improved random number generator*/

#define PI 3.14159265               /*Following used to make code more readable*/
#define DEGTORAD(x) ((x) * 0.017453293)
#define RADTODEG(x) ((x) * 57.29577951)
#define DEBUG 0

extern double Random(void);
extern void PlantSeeds(long x);
/*Not good programming practice, making important variables all global, but I am not a good programmer*/
struct PHOTON {
        double x;                   /*x-position*/
        double y;                   /*y-position*/
        double z;                   /*z-position*/
        double dr;                  /*Increment length*/
        double thetak;                /*k vector's theta*/
        double phik;                  /*k vector's phi*/
        double thetaE;                /*E vector's theta*/
        double phiE;                  /*E vector's phi*/
        int current;                /*Photon's current medium/layer*/
        int next;                   /*Photon's next medium/layer (xy boundary/z-direction)*/
        double xzbc;                  /*xz boundary (y-direction)*/
        double yzbc;                  /*yz boundary (x-direction)*/
        int lambda;                 /*Photon's wavelength*/
}photon;                    /*photon is a varialbe of type PHOTON*/
const char INPUT_FILENAME[] = "definition.txt";
                    /*Define input file for LSC*/
char OUTPUT_FILENAME[100];          /*Output filename array*/
char simulation_name[100];          /*Define simulation name for output file*/
FILE *input_file_definition;        /*Pointer for input file for LSC*/
FILE *output_filename;              /*Pointer for output file for LSC*/
FILE *dummy_filename;                 /*Pointer for dummy files*/
FILE *input_file_layer;             /*Pointer for input file for layer data*/
int loss_flag;                  /*Flag that indicates loss event
                                1: Edge emission
                                2: Facial emission (air)
                                3: Non-radiative loss (phonon)*/
int photon_flag;                  /*Flag to indicate photon emission
                                1: Photon emitted
                                0: Phonon emitted*/
int absorption_flag;                /*Flag that indicates an absorption event
                                1: Photon absorbed
                                0: Photon not absorbed*/
int reflection_flag;              /*Flag that indicates a reflection event
                                1: Reflection occured
                                0: Refraction occured*/
int boundary_flag;                  /*Flag that indicates a boundary
                                000: Not at a boundary
                                001: XZ boundary
                                010: YZ boundary
                                100: XY boundary*/
int number_photon;                  /*Number of photons to simulate*/
int lambda_initial;                         /*Pump wavelength*/
int phi_initial;                            /*Pump E-vector*/
int black_flag;                 /*Flag that indicates edges that are blackened similar to G dependence experiment
                                0: No blackened edges
                                1: Blackened edges*/
int spatial_flag;               /*Flag that indicates nonrandom initial position of excitation source, aka use laser at (x,y)
                                0: Uniform distribution
                                1: Center*/
int back_mirror_flag;                       /*Flag that indicates where to us back mirror or not
                                                        0: No mirror
                                                        1: Mirror */
```

```
int NUMBER_LAYER = 0;                /*Number of layers to define array and matrix dimensions*/
int SPECTRUM_WIDTH = 0;              /*Spectrum width to define matrix dimensions*/
int absorption_event_count;          /*Counter that tracks the # of absorption events*/
int reflection_event_count;          /*Counter that tracks the # of reflection events*/
int spectrum[5000];                  /*Spectrum of side emission of LSC*/
double edge_n;                                          /*Edge refractive index*/
double layer_geometry_info[10][3];       /*Thickness, width, length of each layer, maximum of 10
                                 layer_geometry_info[N-1][0] == length of layer N
                                 layer_geometry_info[N-1][1] == width of layer N
                                 layer_geometry_info[N-1][2] == thickness of layer N*/
double layer_optic_info[5000][4*10+1];   /*Contains the wavelength dependent optical information of
                                 each layer including refractive index, absorption
                                 coefficient, photoluminescence, and optical internal
                                 quantum efficiency
                                 layer_optic_info[:][0] == Relavent spectrum
                                 layer_optic_info[:][4N-3] == Refractive index of layer N
                                 layer_optic_info[:][4N-2] == Absorption coefficient of layer N
                                 layer_optic_info[:][4N-1] == Photoluminescence of layer N
                                 layer_optic_info[:][4N] == Optical IQE of layer N*/
double pdf_pl[5000][10];             /*Probability density function for photoluminescence*/
double isotropic_emission[2000];     /*Emission probability profile for atom/molecule*/
double theta[2000];                  /*Angle of emission for atom/molecule*/
double pv;                           /*Number of photons absorbed at edge for each G*/
double air;                          /*Number of photons emitted at face of LSC for each G*/
double mirror;                       /*Number of photons absorbed by miror for each G*/
double trap;
double absSelf;                      /*Number of photons self-absorbed in LSC for each G*/
double avgAbs;                       /*Average number of absorptions of photons absorbed at PV for each G*/
double trans;                        /*Transmission through LSC*/
double refl;                         /*Reflection off LSC*/

void get_input_data () {
        char INPUT_FILE_LAYER[100];
        int i;
        double dummy, thickness = 0;

        input_file_definition = fopen(INPUT_FILENAME, "r");

        if (input_file_definition == NULL) {
                printf("Cannot open %s\n", INPUT_FILENAME);
                exit(8);
        }else {
                printf("Succesfully opened %s\n", INPUT_FILENAME);
                fscanf(input_file_definition, "%s", INPUT_FILE_LAYER);
                while (strcmp("initialWavelength", INPUT_FILE_LAYER) != 0) {
                        fscanf(input_file_definition, "%lf", &dummy);
                        layer_geometry_info[NUMBER_LAYER][2] = dummy + thickness;
                        thickness = layer_geometry_info[NUMBER_LAYER][2];
                        fscanf(input_file_definition, "%lf", &layer_geometry_info[NUMBER_LAYER][1]);
                        fscanf(input_file_definition, "%lf", &layer_geometry_info[NUMBER_LAYER][0]);
                        input_file_layer = fopen(INPUT_FILE_LAYER, "r");
                        if (input_file_layer == NULL) {
                                printf("Cannot open %s\n", INPUT_FILE_LAYER);
                        } else {
                                printf("Succesfully opened %s\n", INPUT_FILE_LAYER);
                                if (NUMBER_LAYER == 0) {
                                        while (!feof(input_file_layer)) {
                                                fscanf(input_file_layer, "%lf %lf %lf %lf %lf",
&layer_optic_info[SPECTRUM_WIDTH][0], &layer_optic_info[SPECTRUM_WIDTH][1], &layer_optic_info[SPECTRUM_WIDTH][2],
&layer_optic_info[SPECTRUM_WIDTH][3], &layer_optic_info[SPECTRUM_WIDTH][4]);
                                                SPECTRUM_WIDTH = SPECTRUM_WIDTH + 1;
                                        }
                                } else {
                                        for (i = 0; i < SPECTRUM_WIDTH; i++) {
                                                fscanf(input_file_layer, "%lf %lf %lf %lf %lf", &dummy,
&layer_optic_info[i][4*NUMBER_LAYER + 1], &layer_optic_info[i][4*NUMBER_LAYER + 2], &layer_optic_info[i][4*NUMBER_LAYER
+ 3], &layer_optic_info[i][4*NUMBER_LAYER + 4]);
                                        }
                                }
                                fclose(input_file_layer);
```

```
                        }
                        NUMBER_LAYER = NUMBER_LAYER + 1;
                        fscanf(input_file_definition, "%s", INPUT_FILE_LAYER);
                }
                fscanf(input_file_definition, "%d", &lambda_initial);
                fscanf(input_file_definition, "%s %d", INPUT_FILE_LAYER, &phi_initial);
                fscanf(input_file_definition, "%s %d", INPUT_FILE_LAYER, &number_photon);
                fscanf(input_file_definition, "%s %lf", INPUT_FILE_LAYER, &edge_n);
                fscanf(input_file_definition, "%s %d", INPUT_FILE_LAYER, &black_flag);
                fscanf(input_file_definition, "%s %d", INPUT_FILE_LAYER, &spatial_flag);
                fscanf(input_file_definition, "%s %d", INPUT_FILE_LAYER, &back_mirror_flag);
                fscanf(input_file_definition, "%s %s", INPUT_FILE_LAYER, &simulation_name);
        }
        fclose(input_file_definition);
/*****************************************************************************************************/
        if (DEBUG) {
                printf("Spectrum width: %d\n", SPECTRUM_WIDTH);
                printf("Number of layers: %d\n", NUMBER_LAYER);
                printf("Pump lambda: %d\n", lambda_initial);
                printf("Polarization flag: %d\n", phi_initial);
                printf("Spatial flag: %d\n", spatial_flag);
                printf("Number Photons: %d\n", number_photon);
                printf("Edge n: %lf\n", edge_n);
                printf("Black flag: %d\n", black_flag);
                printf("Back Mirror flag: %d\n", back_mirror_flag);
                printf("Simulation Name: %s\n", simulation_name);
                for (i = 0; i < NUMBER_LAYER; i++) {
                        printf("Layer %d: %lf %lf %lf\n", i,
layer_geometry_info[i][2],layer_geometry_info[i][1],layer_geometry_info[i][0]);
                }
                for (i = 0; i < NUMBER_LAYER; i++) {
                        printf("Layer %d Props: %lf %lf %lf %lf\n", i, layer_optic_info[0][4*i + 1], layer_optic_info[0][4*i + 2],
layer_optic_info[0][4*i + 3], layer_optic_info[0][4*i + 4]);
                }
                getchar();
        }
}
/*****************************************************************************************************
*initialize_script is to convert Photoluminescence count of each layer into a probability       *
*density function.  Also, to create the probability density function for the emission angle,     *
*theta for isotropic films.                                                                      *
*****************************************************************************************************/
void initialize_script () {
        double sum_pl;
        int i, j;

        for (i = 0; i < NUMBER_LAYER; i++) {
                sum_pl = 0;
                for (j = 0; j < SPECTRUM_WIDTH; j++) {
                        sum_pl = sum_pl + layer_optic_info[j][4*i+3];
                }
                for (j = 0; j < SPECTRUM_WIDTH; j++) {
                        if (sum_pl == 0) {
                                pdf_pl[j][i] = 0;
                        } else {
                        pdf_pl[j][i] = pdf_pl[j-1][i] + layer_optic_info[j][4*i+3]/sum_pl;
                        }
                }
        }
        theta[0] = 0;
        for (i = 1; i < 2000; i++) {
                theta[i] = theta[i-1] + 0.001571582;
        }

        for (i = 0; i < 2000; i++) {
                isotropic_emission[i] = 0.5*(1 - cos(theta[i]));
        }
}
/*****************************************************************************************************
*lambda_index is to find the array index of the photon wavelength                                 *
```

```
**********************************************************************************************/
void lambda_index() {
        int first = 0;
        int last = SPECTRUM_WIDTH - 1;
        int middle;
        int found = 0;

        while (!found && first <= last) {
                middle = floor((first + last) / 2);
                if (layer_optic_info[middle][0] == lambda_initial) {
                        found = 1;
                        photon.lambda = middle;
                } else {
                        if (layer_optic_info[middle][0] > lambda_initial) {
                                last = middle - 1;
                        } else {
                        first = middle + 1;
                        }
                }
        }
/**********************************************************************************************/
        if (DEBUG) {
                printf("Photon index: %d\n", photon.lambda);
                getchar();
        }
}
/**********************************************************************************************
*initialize_photon initializes the photon, which is mainly comprised of the variable photon.???. *
*The photon's initial postion is in the air layer. Depending on the spatial flag, the (x,y)     *
*position is either random, fixed at the center of the LSC, or stepped across the face of the    *
*LSC. The spherical coordinates are set (theta, phi, r).                                        *
**********************************************************************************************/
void initialize_photon () {
        int i;
        double mux, muy, fwhmx, fwhmy, x, random_number;
        double cdfx[39], cdfy[859];

        switch (spatial_flag) {
                case 0:
                        photon.x = Random()*layer_geometry_info[0][0];
                        photon.y = Random()*layer_geometry_info[0][1];
                        break;
                case 1:
                        photon.x = layer_geometry_info[0][0]*0.5;
                        photon.y = layer_geometry_info[0][1]*0.5;
                        break;
                case 2:
                        mux = .1;
                        muy = 2.15;
                        fwhmx = .1;
                        fwhmy = 2.6;


                        for (i = 0; i < 40; i++){
                                x = 0.005*(0.5 + i);
                                cdfx[i] = 0.5*(1 + erf((x - mux)/(fwhmx*.6006)));
                        }
                        for (i = 0; i < 860; i++){
                                x = 0.005*(0.5 + i);
                                cdfy[i] = 0.5*(1 + erf((x - muy)/(fwhmy*.6006)));
                        }

                        random_number = Random();
                        for (i = 0; i < 40; i++) {
                                if (random_number <= cdfx[i]) {
                                        photon.x = 0.005*(0.5 + i);
                                        break;
                                }
                        }
                        random_number = Random();
```

```
                        for (i = 0; i < 860; i++) {
                                if (random_number <= cdfy[i]) {
                                        photon.y = 0.005*(0.5 + i);
                                        break;
                                }
                        }
                        break;
        }

        photon.thetak = DEGTORAD(0);
        photon.phik = DEGTORAD(phi_initial);
        photon.z = -0.000002;
        photon.dr = 0.000002/cos(photon.thetak);
        photon.thetaE = photon.thetak + PI/2;
        photon.phiE = photon.phik;
        photon.current = 0;
        photon.next = 1;

        if (photon.phik <= PI) {
                photon.xzbc = layer_geometry_info[photon.current][1];
        } else {
                photon.xzbc = 0;
        }
        if (photon.phik <= 0.5*PI || 1.5*PI < photon.phik) {
                photon.yzbc = layer_geometry_info[photon.current][0];
        } else {
                photon.yzbc = 0;
        }

        loss_flag = 0;
        absorption_event_count = 0;
        reflection_event_count = 0;
/*****************************************************************************************/
        if (DEBUG) {
                printf ("*************************************************************\n");
                printf ("Initial Position: (%lf %lf %lf)\n", photon.x, photon.y, photon.z);
                printf ("Initial Vector: (%lf %lf %lf)\n", photon.dr, RADTODEG(photon.thetak), RADTODEG(photon.phik));
                printf ("Initial Polarization: (%lf %lf)\n", RADTODEG(photon.thetaE), RADTODEG(photon.phiE));
                printf ("Initial Layer: %d\n", photon.current);
                printf ("Next layer: %d\n", photon.next);
                printf ("XZ bound: %lf\n", photon.xzbc);
                printf ("YZ bound: %lf\n", photon.yzbc);
                printf ("loss_flag: %d\n", loss_flag);
                getchar();
        }
}
/*****************************************************************************************
*update_layer updates various variables after certain events. After an emission, this function  *
*determines the boundaries the photon is propagating towards (+/-x, +/-y, +/-z). After a       *
*refraction or reflection event, it updates the (+/-z) boundary. Also, after a refraction event,*
*this functions checks if the photon escaped the LSC into the air. If so, it breaks out of the  *
*main loop.                                                                                    *
*****************************************************************************************/
void update_layer (int value) {

        if (value & 1) {
                if (photon.phik <= PI) {
                        photon.xzbc = layer_geometry_info[photon.current][1];
                } else {
                        photon.xzbc = 0;
        }
        }
        if (value & 2) {
                if ((photon.phik <= 0.5*PI) || (1.5*PI < photon.phik)) {
                        photon.yzbc = layer_geometry_info[photon.current][0];
                } else {
                        photon.yzbc = 0;
        }
        }
        if (value & 4) {
```

```
                if (photon.thetak <= 0.5*PI) {
                        photon.next = photon.current + 1;
                } else {
                        photon.next = photon.current - 1;
                }
        }
        if (value & 8) {
                if (photon.thetak >= 0.5*PI) {
                        photon.current = photon.current - 1;
                        photon.next = photon.current - 1;
                } else {
                        photon.current = photon.current + 1;
                        photon.next = photon.current + 1;
                }
        }
        if (value & 16) {
                if (layer_optic_info[photon.lambda][(4*photon.current + 2)] == 0) {
                   photon.dr = 0.5*layer_geometry_info[photon.current][2];
                } else {
                        if (pow(layer_optic_info[photon.lambda][(4*photon.current + 2)], -1) >
(0.25*layer_geometry_info[photon.current][2])) {
                                photon.dr = 0.05*layer_geometry_info[photon.current][2];
                        } else {
                                photon.dr = 0.05*pow(layer_optic_info[photon.lambda][(4*photon.current + 2)], -1);
                        }
                }
        }
        if (value & 32) {
                if (photon.phik <= PI) {
                        photon.xzbc = layer_geometry_info[photon.current][1];
                } else {
                        photon.xzbc = 0;
        }
                if ((photon.phik <= 0.5*PI) || (1.5*PI < photon.phik)) {
                        photon.yzbc = layer_geometry_info[photon.current][0];
                } else {
                        photon.yzbc = 0;
        }
                if (photon.thetak <= 0.5*PI) {
                        photon.next = photon.current + 1;
                } else {
                        photon.next = photon.current - 1;
                }
        }

        if (photon.current == (NUMBER_LAYER - 1) || photon.current == 0) {
                loss_flag = 2;
        }
/*****************************************************************************************************/
        if (DEBUG) {
                printf ("Update\n");
                printf ("\tValue: %d\n", value);
                if (value == 17) {
                        printf ("\tXZ boundary: %lf\n", photon.xzbc);
                }
                if (value == 18) {
                        printf ("\tYZ boundary: %lf\n", photon.yzbc);
                }
                if (value == 20) {
                        printf ("\tNext: %d\n", photon.next);
                }
                if (value == 24) {
                        printf ("\tCurrent: %d\n", photon.current);
                        printf ("\tNext: %d\n", photon.next);
                }
                if (value == 48) {
                        printf ("\tXZ boundary: %lf\n", photon.xzbc);
                        printf ("\tYZ boundary: %lf\n", photon.yzbc);
                        printf ("\tNext: %d\n", photon.next);
                }
```

```
                printf ("\tIncrement: %lf\n", photon.dr);
                printf ("\tLoss Flag: %d\n", loss_flag);
                getchar();
        }
}
/*****************************************************************************************
*check_for_boundary checks to see if the photon is within a photon.dr increment of a boundary.  *
*If it is at a user defined boundary, it determines which (PV, mirror, optical boundary) it is  *
*closest to and increments the photon to the interface.                                          *
*       1 xz plane                                                                               *
*               2 yz plane                                                                                *
*               4 xy plane                                                                      *
*****************************************************************************************/
void check_for_boundary () {
        double xybc = 0;
        double dxo, dx, dyo, dy, dzo, dz, dummy;
        int i;

        boundary_flag = 0;

        if (photon.current > photon.next) {
                xybc = layer_geometry_info[photon.next][2];
        } else {
                xybc = xybc + layer_geometry_info[photon.current][2];
        }

        dxo = fabs(photon.x - photon.yzbc);
        dx = fabs(photon.dr*sin(photon.thetak)*cos(photon.phik));
        dyo = fabs(photon.y - photon.xzbc);
        dy = fabs(photon.dr*sin(photon.thetak)*sin(photon.phik));
        dzo = fabs(photon.z - xybc);
        dz = fabs(photon.dr*cos(photon.thetak));

        if (dxo/dx <= 1) {
                boundary_flag = (boundary_flag | 2);
        }
        if (dyo/dy <= 1) {
                boundary_flag = (boundary_flag | 1);
        }
        if (dzo/dz <= 1) {
                boundary_flag = (boundary_flag | 4);
        }

        dummy = boundary_flag;

        switch (boundary_flag) {
                case 0:
                        break;
                case 1:
                        photon.dr = dyo/fabs(sin(photon.thetak)*sin(photon.phik));
                        photon.z = photon.z + photon.dr*cos(photon.thetak);
                        photon.y = photon.y + photon.dr*sin(photon.thetak)*sin(photon.phik);
                        photon.x = photon.x + photon.dr*sin(photon.thetak)*cos(photon.phik);
                        break;
                case 2:
                        photon.dr = dxo/fabs(sin(photon.thetak)*cos(photon.phik));
                        photon.z = photon.z + photon.dr*cos(photon.thetak);
                        photon.y = photon.y + photon.dr*sin(photon.thetak)*sin(photon.phik);
                        photon.x = photon.x + photon.dr*sin(photon.thetak)*cos(photon.phik);
                        break;
                case 3:
                        if (dxo/dx <= dyo/dy) {
                                boundary_flag = 2;
                                photon.dr = dxo/fabs(sin(photon.thetak)*cos(photon.phik));
                                photon.z = photon.z + photon.dr*cos(photon.thetak);
                                photon.y = photon.y + photon.dr*sin(photon.thetak)*sin(photon.phik);
                                photon.x = photon.x + photon.dr*sin(photon.thetak)*cos(photon.phik);
                        } else {
                                boundary_flag = 1;
                                photon.dr = dyo/fabs(sin(photon.thetak)*sin(photon.phik));
```

```
                                        photon.z = photon.z + photon.dr*cos(photon.thetak);
                                        photon.y = photon.y + photon.dr*sin(photon.thetak)*sin(photon.phik);
                                        photon.x = photon.x + photon.dr*sin(photon.thetak)*cos(photon.phik);
                                }
                                break;
                        case 4:
                                photon.dr = dzo/fabs(cos(photon.thetak));
                                photon.z = photon.z + photon.dr*cos(photon.thetak);
                                photon.y = photon.y + photon.dr*sin(photon.thetak)*sin(photon.phik);
                                photon.x = photon.x + photon.dr*sin(photon.thetak)*cos(photon.phik);
                                break;
                        case 5:
                        if (dyo/dy <= dzo/dz) {
                                        boundary_flag = 1;
                                        photon.dr = dyo/fabs(sin(photon.thetak)*sin(photon.phik));
                                        photon.z = photon.z + photon.dr*cos(photon.thetak);
                                        photon.y = photon.y + photon.dr*sin(photon.thetak)*sin(photon.phik);
                                        photon.x = photon.x + photon.dr*sin(photon.thetak)*cos(photon.phik);
                                } else {
                                        boundary_flag = 4;
                                        photon.dr = dzo/fabs(cos(photon.thetak));
                                        photon.z = photon.z + photon.dr*cos(photon.thetak);
                                        photon.y = photon.y + photon.dr*sin(photon.thetak)*sin(photon.phik);
                                        photon.x = photon.x + photon.dr*sin(photon.thetak)*cos(photon.phik);
        }
        break;
                        case 6:
                                if (dxo/dx <= dzo/dz) {
                                        boundary_flag = 2;
                                        photon.dr = dxo/fabs(sin(photon.thetak)*cos(photon.phik));
                                        photon.z = photon.z + photon.dr*cos(photon.thetak);
                                        photon.y = photon.y + photon.dr*sin(photon.thetak)*sin(photon.phik);
                                        photon.x = photon.x + photon.dr*sin(photon.thetak)*cos(photon.phik);
                                } else {
                                        boundary_flag = 4;
                                        photon.dr = dzo/fabs(cos(photon.thetak));
                                        photon.z = photon.z + photon.dr*cos(photon.thetak);
                                        photon.y = photon.y + photon.dr*sin(photon.thetak)*sin(photon.phik);
                                        photon.x = photon.x + photon.dr*sin(photon.thetak)*cos(photon.phik);
        }
        break;
                        case 7:
                                if (dxo/dx <= dyo/dy && dxo/dx <= dzo/dz) {
                                        boundary_flag = 2;
                                        photon.dr = dxo/fabs(sin(photon.thetak)*cos(photon.phik));
                                        photon.z = photon.z + photon.dr*cos(photon.thetak);
                                        photon.y = photon.y + photon.dr*sin(photon.thetak)*sin(photon.phik);
                                        photon.x = photon.x + photon.dr*sin(photon.thetak)*cos(photon.phik);
                                } else {
                                        if (dyo/dy <= dzo/dz) {
                                                boundary_flag = 1;
                                                photon.dr = dyo/fabs(sin(photon.thetak)*sin(photon.phik));
                                        photon.z = photon.z + photon.dr*cos(photon.thetak);
                                        photon.y = photon.y + photon.dr*sin(photon.thetak)*sin(photon.phik);
                                        photon.x = photon.x + photon.dr*sin(photon.thetak)*cos(photon.phik);
                                        } else {
                                        boundary_flag = 4;
                                                photon.dr = dzo/fabs(cos(photon.thetak));
                                                photon.z = photon.z + photon.dr*cos(photon.thetak);
                                        photon.y = photon.y + photon.dr*sin(photon.thetak)*sin(photon.phik);
                                        photon.x = photon.x + photon.dr*sin(photon.thetak)*cos(photon.phik);
          }
        }
        break;
           }
/*****************************************************************************************************/
          if (DEBUG) {
                        if (dx == 0) {
                                dx = .000001;
                        }
```

```
                if (dy == 0) {
                        dy = .000001;
                }
                if (dz == 0) {
                        dz = .000001;
                }
                printf ("Check For Boundary\n");
                printf ("Boundary: %lf\n", dummy);
                printf ("\txybc: %lf\n",xybc);
                printf ("\tx: %lf\n", dxo/dx);
                printf ("\ty: %lf\n", dyo/dy);
                printf ("\tz: %lf\n", dzo/dz);
                printf ("\tBoundary: %d\n", boundary_flag);
                printf ("\tNew position: (%lf %lf %lf)\n", photon.x, photon.y, photon.z);
                printf ("\tIncrement: %lf\n", photon.dr);
                getchar();
        }
}
/*****************************************************************************************
*increment_position increments the photon's position based on the current cartesion coordinates  *
*and the spherical coordinates.  Also, this tracks the photon's time in the cladding layer and   *
*core layer (organic layer versus glass waveguide).                                              *
*****************************************************************************************/
void increment_position () {
        photon.z = photon.z + photon.dr*cos(photon.thetak);
        photon.y = photon.y + photon.dr*sin(photon.thetak)*sin(photon.phik);
        photon.x = photon.x + photon.dr*sin(photon.thetak)*cos(photon.phik);
/*****************************************************************************************/
        if (DEBUG) {
                printf ("Increment Position\n");
                printf ("\tNew Postion: (%lf %lf %lf)\n", photon.x, photon.y, photon.z);
                getchar();
        }
}
/*****************************************************************************************
*absorption uses the Beer-Lambert law to determine the probability of a photon being absorbed,   *
*based on the medium's wavelength dependent absorption coefficient and the spatial step.  Using  *
*a random number generator to then determine if the photon was absorbed or not.                  *
*****************************************************************************************/
void absorption () {
        double random_number;
        int value;

        if (Random() <= ((1 - exp(-photon.dr*layer_optic_info[photon.lambda][(4*photon.current + 2)])))) {
                absorption_flag = 1;
                absorption_event_count = absorption_event_count + 1;
        } else {
                absorption_flag = 0;
        }
/*****************************************************************************************/
        if (DEBUG) {
                printf ("\tdr: %lf\n", photon.dr);
                printf ("\ta: %lf\n", layer_optic_info[photon.lambda][(4*photon.current + 2)]);
                printf ("\texp(-a*dr): %lf\n", ((1 - exp(-photon.dr*layer_optic_info[photon.lambda][(4*photon.current + 2)]))));
                printf ("\tAbsorption: %d\n", absorption_flag);
                getchar();
        }
}
/*****************************************************************************************
*phonon_or_photon determines if an absorbed photon emits a photon or a phonon based on the       *
*mediums photoluminescence quantum efficiency.  Using a random number generator to determine if  *
*the photon is emitted or not.                                                                   *
*****************************************************************************************/
void phonon_or_photon () {

        if (Random() < layer_optic_info[photon.lambda][(4*photon.current + 4)]) {
        photon_flag = 1;
        } else {
        photon_flag = 0;
        }
```

```
/*****************************************************************************************/
        if (DEBUG) {
                printf ("Photon or Phonon\n");
                printf ("\tPhoton: %d\n", photon_flag);
                getchar();
        }
}
/*****************************************************************************************
*emission randomly selects the emitted photon's new wavelength based on the probability density  *
*function, and the photon's new vector (theta, phi) based on a random number generator.          *
*****************************************************************************************/
void emission () {
        double random_number;
        int i;

        random_number = Random();
        for (i = 0; i < SPECTRUM_WIDTH; i++) {
                if (random_number <= pdf_pl[i][photon.current]) {
                        photon.lambda = i;
                        break;
                }
        }
        photon.phik = 2*PI*Random();
        random_number = Random();

        for (i = 0; i < 2000; i++) {
                if (random_number <= isotropic_emission[i]) {
                        photon.thetak = theta[i];
                        break;
                }
        }

        photon.phiE = 2*PI*Random();
        photon.thetaE = atan(-1/(tan(photon.thetak)*cos(photon.phik - photon.phiE)));
        if (photon.thetaE < 0) {
                photon.thetaE = PI + photon.thetaE;
        }
/*****************************************************************************************/
        if (DEBUG) {
                printf ("Emission\n");
                printf ("\tNew lambda index: %d\n", photon.lambda);
                printf ("\tNew vector`: (%lf %lf %lf)\n", photon.dr, RADTODEG(photon.thetak), RADTODEG(photon.phik));
                printf ("\tNew polarization: (%lf %lf)\n", RADTODEG(photon.thetaE), RADTODEG(photon.phiE));
                getchar();
        }
}
/*****************************************************************************************
*refraction calculates the transmitted photon's new theta based on phase matching or snell's law.*
*****************************************************************************************/
void refraction () {
        double n1, n2;

        if (boundary_flag == 4) {
                n1 = layer_optic_info[photon.lambda][(4*photon.current + 1)];
                n2 = layer_optic_info[photon.lambda][(4*photon.next + 1)];
        } else {
                n1 = layer_optic_info[photon.lambda][(4*photon.current + 1)];
                n2 = edge_n;
        }
        if (photon.thetak >= 0.5*PI) {
                photon.thetak = PI - asin((n1/n2)*sin(PI - photon.thetak));
                photon.thetaE = fabs(atan(-1/(tan(photon.thetak)*cos(photon.phik - photon.phiE))));
        } else {
                photon.thetak = asin((n1/n2)*sin(photon.thetak));
                photon.thetaE = fabs(atan(-1/(tan(photon.thetak)*cos(photon.phik - photon.phiE))));
        }

/*****************************************************************************************/
        if (DEBUG) {
                printf ("Refraction\n");
```

```
                printf ("\tn1: %lf n2: %lf\n", n1, n2);
                printf ("\tTheta k: %lf\n", RADTODEG(photon.thetak));
                printf ("\tTheta E: %lf\n", RADTODEG(photon.thetaE));
                getchar();
        }
}
/*****************************************************************************************
*reflection calculates the photon's new vector assuming a facial reflection due to a mirror, *
*photonic crystal, or fresnel equations.                                                    *
*****************************************************************************************/
void reflection () {

        photon.thetak = PI - photon.thetak;
        if (photon.phiE > PI) {
                photon.phiE = photon.phiE - PI;
        } else {
                photon.phiE = photon.phiE + PI;
        }
        reflection_event_count = reflection_event_count + 1;

        if (DEBUG) {
                printf ("Reflection Face\n");
                printf ("\tNew theta: %lf\n", RADTODEG(photon.thetak));
                printf ("\tNew polarization: (%lf %lf)\n", RADTODEG(photon.thetaE), RADTODEG(photon.phiE));
                getchar();
        }
}
/*****************************************************************************************
*reflection_coefficient calculates the fresnel equation reflection coefficients due to a   *
*refractive index step. This function assumes unpolarized light. Then using a random number *
*generator, determines if the photon was reflected or refracted.                           *
*****************************************************************************************/
void reflection_coefficient () {
        double R = 0;
        double R_s, R_p, n1, n2, temp, s_coe = 0, p_coe = 0;
        double theta_temp;

        if (boundary_flag == 4) {
                n1 = layer_optic_info[photon.lambda][(4*photon.current + 1)];
                n2 = layer_optic_info[photon.lambda][(4*photon.next + 1)];
        } else {
                n1 = layer_optic_info[photon.lambda][(4*photon.current + 1)];
                n2 = edge_n;
        }
        if (photon.thetak >= 0.5*PI) {
                theta_temp = PI - photon.thetak;
        } else {
                theta_temp = photon.thetak;
        }

        if (n2/n1 <= 1) {
                if (theta_temp >= asin(n2/n1)) {
                        R = 1;
                }
        }
        if (photon.next == (NUMBER_LAYER-1) && back_mirror_flag) {
                R = 1;
        }
        if (R == 0) {
                temp = pow((n1/n2)*sin(theta_temp), 2);
                s_coe = pow(sin(photon.phik - photon.phiE), 2);
                p_coe = pow(cos(photon.phik - photon.phiE), 2);

                R_s = s_coe*pow((n1*cos(theta_temp) - n2*pow(1 - temp ,0.5))/(n1*cos(theta_temp) + n2*pow(1 - temp ,0.5)), 2);
                R_p = p_coe*pow((n1*pow(1 - temp, 0.5) - n2*cos(theta_temp))/(n1*pow(1 - temp, 0.5) + n2*cos(theta_temp)), 2);

                R = R_s + R_p;
        }

        if (Random() <= R) {
```

```
                reflection_flag = 1;
        } else {
                reflection_flag = 0;
        }
/*****************************************************************************************************/
        if (DEBUG) {
                printf ("Reflection Coefficient\n");
                printf ("\tn1: %lf n2: %lf\n", n1, n2);
                printf ("\ts_coe: %lf p_coe: %lf\n", s_coe, p_coe);
                printf ("\tReflection Coefficient: %lf\n", R);
                printf ("\tReflection flag: %d\n", reflection_flag);
                getchar();
        }
}
/*****************************************************************************************************
*new_coordinates converts the spherial coordinates where theta is measured from the z-axis to   *
*the vector to where theta is measured from either the x-axis or y-axis depending on which plane*
*the photon is incident (xz boundary/yz boundary)
                        *
*Conversion:             0 xyz -> yzx
                                                                *
*                       1 yzx -> xyz
                                                                        *
*                       2 xyz -> zxy
*                       3 zxy -> xyz
                                                                                        *
*****************************************************************************************************/
void new_coordinates (int conversion) {
        double new_theta, kx, ky, kz, Ex, Ey, Ez;

        if (DEBUG) {
                printf ("Conversion\n");
                printf ("\tOld vector: (%lf, %lf)\n", RADTODEG(photon.thetak), RADTODEG(photon.phik));
                printf ("\tOld polarization: (%lf, %lf)\n", RADTODEG(photon.thetaE), RADTODEG(photon.phiE));
        }

        switch (conversion) {
                case 0:
                        kx = cos(photon.phik)*sin(photon.thetak);
                        ky = sin(photon.phik)*sin(photon.thetak);
                        kz = cos(photon.thetak);
                        Ex = cos(photon.phiE)*sin(photon.thetaE);
                        Ey = sin(photon.phiE)*sin(photon.thetaE);
                        Ez = cos(photon.thetaE);

                        new_theta = acos(kx);
                        if (kz > 0) {
                                photon.phik = acos(ky/sin(new_theta));
                        } else {
                                photon.phik = 2*PI - acos(ky/sin(new_theta));
                        }
                        photon.thetak = new_theta;
                        new_theta = acos(Ex);
                        if (Ez > 0) {
                                photon.phiE = acos(Ey/sin(new_theta));
                        } else {
                                photon.phiE = 2*PI - acos(Ey/sin(new_theta));
                        }
                        photon.thetaE = new_theta;
                        break;
                case 1:
                        kx = cos(photon.thetak);
                        ky = cos(photon.phik)*sin(photon.thetak);
                        kz = sin(photon.phik)*sin(photon.thetak);
                        Ex = cos(photon.thetaE);
                        Ey = cos(photon.phiE)*sin(photon.thetaE);
                        Ez = sin(photon.phiE)*sin(photon.thetaE);

                        new_theta = acos(kz);
                        if (ky > 0) {
```

```
                        photon.phik = acos(kx/sin(new_theta));
                } else {
                        photon.phik = 2*PI - acos(kx/sin(new_theta));
                }
                photon.thetak = new_theta;
                new_theta = acos(Ez);
                if (Ey > 0) {
                        photon.phiE = acos(Ex/sin(new_theta));
                } else {
                        photon.phiE = 2*PI - acos(Ex/sin(new_theta));
                }
                photon.thetaE = new_theta;
                break;
        case 2:
                kx = cos(photon.phik)*sin(photon.thetak);
                ky = sin(photon.phik)*sin(photon.thetak);
                kz = cos(photon.thetak);
                Ex = cos(photon.phiE)*sin(photon.thetaE);
                Ey = sin(photon.phiE)*sin(photon.thetaE);
                Ez = cos(photon.thetaE);

                new_theta = acos(ky);
                if (kx > 0) {
                        photon.phik = acos(kz/sin(new_theta));
                } else {
                        photon.phik = 2*PI - acos(kz/sin(new_theta));
                }
                photon.thetak = new_theta;
                new_theta = acos(Ey);
                if (Ex > 0) {
                        photon.phiE = acos(Ez/sin(new_theta));
                } else {
                        photon.phiE = 2*PI - acos(Ez/sin(new_theta));
                }
                photon.thetaE = new_theta;
                break;
        case 3:
                kx = sin(photon.phik)*sin(photon.thetak);
                ky = cos(photon.thetak);
                kz = cos(photon.phik)*sin(photon.thetak);
                Ex = sin(photon.phiE)*sin(photon.thetaE);
                Ey = cos(photon.thetaE);
                Ez = cos(photon.phiE)*sin(photon.thetaE);

                new_theta = acos(kz);
                if (ky > 0) {
                        photon.phik = acos(kx/sin(new_theta));
                } else {
                        photon.phik = 2*PI - acos(kx/sin(new_theta));
                }
                photon.thetak = new_theta;
                new_theta = acos(Ez);
                if (Ey > 0) {
                        photon.phiE = acos(Ex/sin(new_theta));
                } else {
                        photon.phiE = 2*PI - acos(Ex/sin(new_theta));
                }
                photon.thetaE = new_theta;
                break;
        }
/*****************************************************************************************/
        if (DEBUG) {
                printf ("\tNew vector: (%lf, %lf)\n", RADTODEG(photon.thetak), RADTODEG(photon.phik));
                printf ("\tNew polarization: (%lf, %lf)\n", RADTODEG(photon.thetaE), RADTODEG(photon.phiE));
                getchar();
        }
}
/*****************************************************************************************
*****************************************************************************************/
int main()
```

```
{
        int i;

        PlantSeeds(-1);
        get_input_data ();
        initialize_script ();
        for (i = 0; i < number_photon; i++){
                lambda_index();
                initialize_photon ();
                while (!loss_flag) {
                        increment_position ();
                        absorption ();
                        if (absorption_flag) {
                                phonon_or_photon ();
                                if (photon_flag) {
                                        emission ();
                                        update_layer (48);
                                } else {
                                        loss_flag = 3;
                                }
                        }
                        while (1) {
                                top:
                                if (reflection_event_count > 10000) {
                                        loss_flag = 5;
                                        break;
                                }
                                check_for_boundary ();
                                if (boundary_flag) {
                                        absorption ();
                                        if (absorption_flag) {
                                                phonon_or_photon ();
                                                if (photon_flag) {
                                                        emission ();
                                                        update_layer (48);
                                                        goto top;
                                                } else {
                                                        loss_flag = 3;
                                                        break;
                                                }
                                        }
                                } else {
                                        break;
                                }
                                if (boundary_flag == 1) {
                                        if (black_flag) {
                                                loss_flag = 1;
                                                break;
                                        } else {
                                                new_coordinates (2);
                                                reflection_coefficient ();
                                                if (reflection_flag) {
                                                        reflection ();
                                                        new_coordinates (3);
                                                        update_layer(17);
                                                } else {
                                                        refraction ();
                                                        new_coordinates (3);
                                                        loss_flag = 1;
                                                        break;
                                                }
                                        }
                                } else {
                                        if (boundary_flag == 2) {
                                                if (black_flag) {
                                                        loss_flag = 1;
                                                        break;
                                                } else {
                                                        new_coordinates (0);
                                                        reflection_coefficient ();
```

```
                                                if (reflection_flag) {
                                                        reflection ();
                                                        new_coordinates (1);
                                                        update_layer(18);
                                                } else {
                                                        refraction ();
                                                        new_coordinates (1);
                                                        loss_flag = 1;
                                                        break;
                                                }
                                        }
                                } else {
                                        if (boundary_flag == 4) {
                                                reflection_coefficient ();
                                                if (reflection_flag) {
                                                        reflection ();
                                                        update_layer(20);
                                                } else {
                                                        refraction ();
                                                        update_layer(24);
                                                        if (loss_flag) {
                                                                break;
                                                        }
                                                }
                                        }
                                }
                        }
                }
                dummy_filename = fopen(simulation_name, "a");
                fprintf (dummy_filename, "%d\t%d\t%lf\t%lf\t%lf\t%lf\t%lf\t%lf\t%d\t%d\n", loss_flag, photon.current,
layer_optic_info[photon.lambda][0], photon.x, photon.y, photon.z, photon.thetak, photon.phik, absorption_event_count, reflection_event_count);
                fclose(dummy_filename);
        }
        return 0;
}
```

References

[1] The World Bank. "Energy – The Facts." The World Bank, Web. 02 July, 2014. http://go.worldbank.org/6ITD8WA1A0.

[2] Gates, Bill. "Powering the Fight Against Poverty." Gates Notes: The Blog of Bill Gates, 25 June, 2014. Web. 02 July, 2014. http://www.gatesnotes.com/Energy/Powering-the-Fight-Against-Poverty.

[3] Perez, R. and M. Perez, The IEA SHC Solar Update, 50: 2-3, (2009)

[4] P. Lorenz, D. Pinner, and T. Seitz, "The Economics of Solar Power," McKinsey Quarterly, June 2008.

[5] Currie, M. J., J. K. Mapel, T. D. Heidel, S. Goffri, and M. A. Baldo, "High-efficiency organic solar concentrators for photovoltaics," Science, 321(5886):226-8, 2008.

[6] EV World, "Our $100 Billion Clean Energy Future," EVWorld.com, 25 March, 2005. Web. 02 July, 2014. http://evworld.com/article.cfm?storyid=827.

[7] http://www.ntkj.co.jp/product_fresnel_solar_en.html.

[8] Smestad, G, H. Ries, R. Winston, and E. Yablonovitch, "The thermodynamic limits of light concentrators," Solar Energy Materials, 21: 99-111, 1990.

[9] IRENA, "Concentrating Solar Power," IRENA Working Paper, 1(2), 2012.

[10] Feldman, D., G. Barbose, R. Margolis, R. Wiser, N. Darghouth, and A. Goodrich, "Photovoltaic (PV) Pricing Trends: Historical, Recent, and Near-Term Projections," Sunshot US DOE, 2012.

[11] Shockely, W., and H. J. Queisser, "Detailed balance limit of efficiency of p-n junction solar cells," Journal of Applied Physics, 32(3):510, 1961.

[12] Smith, M., and J. Michl, "Singlet Fission," Chem. Rev. 110, 6891, 2010.

[13] Lee, J., P. Jadhav, and M. Baldo, "High efficiency organic multilayer photodetectors based on singlet exciton fission," Appl. Phys. Lett. 95, 033301, 2009.

[14] Jadhav, P., A. Mohanty, J. Sussman, J. Lee, and M. Baldo, "Singlet exciton fission in nanostructured organic solar cells," Nano Lett. 11, 1495, 2011.

[15] Ehrler, B., M. Wilson, A. Rao, R. Friend, and N. Greenham, "Singlet exciton fission-sensitized infrared quantum dot solar cells," Nano Lett. 12, 1053, 2012.

[16] Reusswig, P. D., D. N. Congreve, N. J. Thompson, and M. A. Baldo, "Enhanced external quantum efficiency in an organic photovoltaic cell via singlet exciton fission sensitizer," Appl. Phys. Lett. 101(11), 2012.

[17] Kageyama, H., H. Ohishi, M. Tanaka, Y. Ohmori, and Y. Shirota, "High performance organic photovoltaic devices using amorphous molecular materials with high charge-carrier drift mobilities," Appl. Phys. Lett. 94 063304, 2009.

[18] Frankevich, E., B. Rumyantsev, and V. Lesin, "Magnetic field effect on the thermostimulated chemiluminescence of photoperoxidized rubrene," J. of Lum. 11, 91, 1975.

[19] Hamada, Y., H. Kanno, T. Tsujioka, H. Takahashi, and T. Usuki, "Red organic light-emitting diodes using an emitting assist dopant," Appl. Phys. Lett. 75, 1682, 1999.

[20] Hirade, M., and C. Adachi, "Small molecular organic photovoltaic cells with exciton blocking layer at anode interface for improved device performance," Appl. Phys. Lett. 99, 153302, 2011.

[21] Geacintov, N., M. Pope, and F. Vogel, "Effect of magnetic field on the fluorescence of tetracene crystals: exciton fission," Phys. Rev. Lett. 22, 593, 1969.

[22] Johnson, R. C., and R. E. Merrifield, "Effects of magnetic fields on the mutual annihilation of triplet excitons in anthracene crystals," Phys. Rev. B 1, 896, 1970.

[23] Jadhav, P., P. Brown, N. Thompson, B. Wunsch, A. Mohanty, S. Yost, E. Hontz, T. Van Voorhis, M. Bawendi, V. Bulovic, and M. Baldo, "Triplet exciton dissociation in singlet exciton fission photovoltaics," Adv. Mat. 24(46), 2012.

[24] Zhan, X., A. Facchetti, S. Barlow, T.J. Marks, M.A. Ratner, M.R. Wasielweski, and S.R. Marder, "Rylene and related diimides for organic electronics," Adv. Mat. 23, 268-284, 2011.

[25] Hammond, S., J. Meyer, N. Widjonarko, P. Ndione, A. Sigdel, A. Garcia, A. Miedaner, M. Lloyd, A. Kahn, D. Ginley, J. Berry, and D. Olson, "Low-temperature, solution-processed molybdenum oxide hole-collection layer for organic photovoltaics," J. Mater. Chem. 22, 3249, 2012.

[26] Kahn, A., N. Koch, and W. Y. Gao, "Electronic structure and electrical properties of interfaces between metals and π-conjugated molecular films," J. Polym. Sci., Part B: Polym. Phys. 41, 2529, 2003.

[27] Heidel, T. D., D. Hochbaum, J. M. Sussman, V. Singh, M. E. Bahlke, I. Hiromi, J. Lee, and M. A. Baldo, "Reducing recombination losses in planar organic photovoltaic cells using multiple step charge separation," J. Appl. Phys. 109, 104502, 2011.

[28] Congreve, D. N., J. Lee, N. J. Thompson, E. Hontz, S. R. Yost, P. D. Reusswig, M. E. Bahlke, S. Reineke, T. V. Voorhis, M. A. Baldo, "External Quantum Efficiency Above 100% in a Singlet-Exciton-Fission–Based Organic Photovoltaic Cell," Science 340(6130), 2013.

[29] Weber, W. H., and J. Lambe, "Luminescent greenhouse collector for solar radiation," Applied Optics 15(10), 1976.

[30] Batchelder, J. S., A. H. Zewail, and T. Cole, "Luminescent solar concentrators. 1: Theory of operation and techniques for performance evaluation," Applied Optics 18(18), 1979.

[31] Batchelder, J. S., A. H. Zewail, and T. Cole, "Luminescent solar concentrators. 2: Experimental and theoretical analysis of their possible efficiencies," Applied Optics 20(21), 1981.

[32] Slooff, L. H., E. E. Bende, A. R. Burgers, T. Budel, M. Pravettoni, R. P. Kenny, E. D. Dunlop, and A. Buchtemann, "A Luminescent Solar Concentrator with 7.1% Power Conversion Efficiency," Physica Status Solidi-Rapid Research Letters 2(6), 2008.

[33] Meinardi, F., A. Colombo, K. A. Velizhanin, R. Simonutti, M. Lorezon, L. Beverina, R. Viswanatha, V. I. Klimov, and S. Brovelli, "Large-area luminescent solar concentrators based on 'Stokes-shift-engineered' nanocrystals in a mass-polymerized PMMA matrix," Nature Photonics 8(5), 2014.

[34] Coropceanu, I., and M. G. Bawendi, "Core/Shell Quantum Dot Based Luminescent Solar Concentrators with Reduced Reabsorption and Enhanced Efficiency," Nano Letters, ASAP.

[35] Erickson, C. S., L. R. Bradshaw, S. McDowall, J. D. Gilbertson, D. R. Gamelin, and D. L. Patrick, "Zero-Reabsorption Doped-Nanocrystal Luminescent Solar Concentrators," ACS Nano 8(4), 2014.

[36] Reisfeld, R., and Y. Kalisky, "Nd3+ and Yb3+ germinate and tellurite glasses for fluorescent solar energy collectors," Chem. Phys. Lett. 80(1), 1981.

[37] Mulder, C. L., L. Theogarajan, M. Currie, J. K. Mapel, M. A. Baldo, M. Vaughn, P. Willard, B. D. Bruce, M. W. Moss, C. E. McLain, and J. P. Morseman, "Luminescent Solar Concentrators Employing Phycobilisomes," Advanced Materials 21(31), 2009.

[38] Mulder, C. L., P. D. Reusswig, A. M. Velázquez, H. Kim, C. Rotschild, M.A. Baldo, "Dye Alignment in Luminescent Solar Concentrators: I. Vertical Alignment for Improved Waveguide Coupling," Optics Express 18(S1), 2010.

[39] Hoffmann, W., "PV solar electricity industry: Market growth and perspective," Solar Energy Materials and Solar Cells 90, 2009.

[40] https://lasers.llnl.gov/.

[41] Haxel, G. B., J. B. Hedrick, and G. J. Orris, "Rare Earth Elements—Critical Resources for High Technology," U.S. Geological Survey, http://pubs.usgs.gov/fs/2002/fs087-02/.

[42] Ronda, C. R., T. Jüstel, H. Nikol, "Rare earth phosphors: fundamentals and applications," Journal of Alloys and Compounds 275-277, 1998.

[43] Croat, J. J., J. F. Herbst, R. W. Lee, and F. E. Pinkerton, "Pr-Fe and Nd-Fe-based materials: A new class of high-performance permanent magnets," Journal of Applied Physics 55(2078), 1984.

[44] Caird, J. A., A. J. Ramponi, and P. R. Staver, "Quantum efficiency and excited-state relaxation dynamics in neodymium-doped phosphate laser glasses," Journal of the Optical Society of America B 8(7), 1991.

[45] Lee, J., V. C. Sundar, J. R. Heine, M. G. Bawendi, and K. F. Jensen, "Full color emission from II-VI semiconductor quantum dot-polymer composites," Advanced Materials 12, 2000.

[46] Mashford, B. S., M. Stevenson, Z. Popovic, C. Hamilton, Z. Zhou, C. Breen, J. Steckel, V. Bulovic, M. Bawendi, S. Coe-Sullivan, and P. T. Kazlas, "High-efficiency quantum-dot light-emitting devices with enhanced charge injection," Nature Photonics 7, 2013.

[47] Chuang, C. M., P. R. Brown, V. Bulović, and M. G. Bawendi, "Improved performance and stability in quantum dot solar cells through band alignment engineering," Nature Materials, Online, 2014.

[48] Liang, G., L. Li, H. Liu, J. Zhang, C. Burda, and J. Zhu, "Fabrication of near-infrared-emitting CdSeTe/ZnS core/shell quantum dots and their electrogenerated chemiluminescence," Chemical Communications 46(17), 2010.

[49] http://www.plasmachem.com/.

[50] MacDougall, S. K.W., A. Ivaturi, J. Marques-Hueso, K.W. Kramer, and B.S. Richards, "Broadband photoluminescent quantum yield optimization of Er3+-doped β-NaYF4 for upconversion in silicon solar cells," Solar Energy Materials & Solar Cells 128, 2014.

[51] Ou, Z.Y., S.F. Pereira, E.S. Polzik, and H.J. Kimble, "85% efficiency for cw frequency doubling from 1.08 to 0.54 μm," Optics Letters17(9), 1992.

[52] Z. J. Kiss, H. R. Lewis, and R. C. Duncan, Jr., "Sun pumped continuous optical maser," Applied Physics Letters, 2(5):93-94, 1963.

[53] T. Yabe, B. Bagheri, T. Ohkubo, S. Uchida, K. Yoshida, T. Funatsu, T. Oishi, K. Daito, M. Ishioka, N. Yasunaga, Y. Sato, C. Baasandash, Y. Okamoto, and K. Yanagitani, "100 W-class solar pumped laser for sustainable magnesium-hydrogen energy cycle," Journal of Applied Physics, 104(8), 2008.

[54] T. H. Dinh, T. Ohkubo, T. Yabe, and H. Kuboyama, "120 watt continuous wave solar-pumped laser with a liquid light-guide lens and an Nd:YAG rod," Optics Letters, 37(13), 2012.

[55] Liang, D., and J. Almeida, "Highly efficient solar-pumped Nd:YAG laser," Optics Express, 19(27), 2011.

[56] Almeida, J., D. Liang, E. Guillot, and Y. Abdel-Hadi, "A 40 W cw Nd:YAG solar laser pumped through a heliostat: a parabolic mirror system," Laser Physics, 23(6), 2013.

[57] Yabe T.,, T. Ohkubo, S. Uchida, K. Yoshida, M. Nakatsuka, T. Funatsu, A. Mabuti, A. Oyama, K. Nakagawa, T. Oishi, K. Daito, B. Behgol, Y. Nakayama, M. Yoshida, S. Motokoshi, Y. Sato, and C. Baasandash, "High-efficiency and economical solar-energy-pumped laser with fresnel lens and chromium codoped laser medium," Applied Physics Letters, 90(26):261120, 2007.

[58] Mizuno, S., H. Ito, K. Hasegawa, T. Suzuki, and Y. Ohishi, "Laser emission from a solar-pumped fiber," Optics Express, 20(6), 2012.

[9] Rotschild, C., M. Tomes, H. Mendoza, T. L. Andrew, T. M. Swager, T. Carmon, and M. A. Baldo, "Cascade energy transfer for efficienct broad-band pumping of high-quality, micro-lasers," Advanced Materials, 23(27):3057-60, 2011.

[60] Chen, O., H. Wei, A. Maurice, and M. G. Bawendi, "Pure colors from core-shell quantum dots," MRS Bulletin, 38(9):696-702, 2013.

[61] Chen, O., J. Zhao, V. P. Chauhan, J. Cui, C. Wong, D.K. Harris, H. Wei, H. Han, D. Fukumura, R. K. Jain, and M.G. Bawendi, "Compact high-quality CdSe-CdS core-shell nanocrystals with narrow emission linewidths and suppressed blinking," Nature Materials, 12(5):445-51, 2013.

[62] Roxlo, C.B., and E. Yablonovitch, "Thermodynamics of daylight-pumped lasers," Optics Letters, 8(5):271-273, 1983.

[63] Giebink, N.C., G.P. Wiederrecht, and M.R. Wasielewski, "Resonance-shifting to circumvent reabsorption loss in luminescent solar concentrators," Nature Photonics, 5(11):694, 2011.

[64] Liang, G., L. Li, H. Liu, J. Zhang, C. Burda, and J. Zhu, "Fabrication of near-infrared-emitting CdSeTe/ZnS core/shell quantum dots and their electrogenerated chemiluminescence," Chemical Communications, 46(17): 2974-2976, 2010.

[65] Burrus, C.A., and J. Stone, "Single–crystal fiber optical devices: A Nd:YAG fiber laser," Applied Physics Letters, 26(318):318-320, 1975.

[66] R.Winston, "Principles of solar concentrators of a novel design," Solar Energy, 16:89-95, 1974.